Fall 2017

Geophysical assessment of soil and rock in the New Madrid seismic zone

Faraj Mohamed Eljabri

GEOPHYSICAL ASSESSMENT OF SOIL AND ROCK IN THE NEW MADRID SEISMIC ZONE

by

FARAJ MOHAMED ELJABRI

A DISSERTATION

Presented to the Faculty of the Graduate School of the

MISSOURI UNIVERSITY OF SCIENCE AND TECHNOLOGY

In Partial Fulfillment of the Requirements for the Degree

DOCTOR OF PHILOSOPHY

in

GEOLOGICAL ENGINEERING

2017

Approved by

Neil L. Anderson, Advisor
David J. Rogers
Lesley H. Sneed
Evgeniy V. Torgashov
Jeffrey D. Cawlfield

ABSTRACT

The research presented here consists of two case studies: the first from a study site in Illinois and the second from a site in Arkansas. In both instances, geophysical investigations were conducted to characterize the subsurface. At the Illinois site, borehole control, downhole seismic (DHS), seismic refraction tomography (SRT) and multichannel analysis of surface waves (MASW) data were acquired for the purpose of seismic site characterization. Shear wave and compressional wave velocities were used to estimate depth to bedrock and to generate 1-D plots depicting variations in Poisson's Ratio, elastic moduli and density. The average shear wave velocity in the upper 100 ft was calculated and the national earthquake hazards reduction program (NEHRP) class D was assigned to the site based on MASW and DHS data results. At the Arkansas site, borehole control, electrical resistivity tomography (ERT), seismic refraction tomography (SRT), and multichannel analysis of surface waves (MASW) data were acquired with the objective of verifying and mapping a postulated fault. A comparative evaluation of the overall usefulness of the ERT, SRT and MASW techniques was also performed. The comparison showed that ERT and SRT tools generated remarkably similar images of the fault. The MASW tool generated a slightly different image of the fault. The research demonstrates that integrated use of seismic (seismic refraction tomography, multichannel analysis of surface waves and downhole seismic) and electrical (electrical resistivity tomography) methods is an effective approach in terms of assessing soil and rock in the New Madrid Seismic Zone.

ACKNOWLEDGMENTS

I am very grateful to my advisors, Dr. Neil L. Anderson and Dr. David J. Rogers for their valuable guidance and patient encouragement during the stages of the dissertation.

My grateful thanks to Dr. Evgeniy V. Torgashov, Dr. Jeffrey D. Cawlfield, and Dr. Lesley H. Sneed for serving on my committee and for their instructive and active help.

I would also like to thank the faculty members, students, workers, and staff for their successful efforts.

My special thanks to Illinois Department of Transportation and Geotechnology INC for providing with DHS and borehole data and my grateful thanks to Dr. Niemi Tina, James Dunahue, and Marion Haynes, Arkansas University.

Finally, I would like to express my thanks to my wife for her support and patience during the period of my dissertation.

TABLE OF CONTENTS

Page

LIST OF ILLUSTRATIONS

LIST OF TABLES

1. INTRODUCTION

Geophysical methods have been playing a vital role in subsurface imaging in the recent past. The main advantages of non-destructive geophysical methods over conventional intrusive site investigation techniques are cost-effectiveness and efficiency. Geophysical methods are used for a variety of engineering investigations, including: seismic site characterization, bedrock depth delineation, rock type definition, layer boundaries mapping, water table detection, groundwater flow detection, locating fractures, weak zones, expansive clays, etc. For the purposes of subsurface characterization, it is common to map variations in the physical properties of subsurface materials (elastic moduli, density, porosity, etc.).

This research is based on two case studies in which non-destructive geophysical methods were used in combination with destructive testing. The main goal of the research is to demonstrate that non-destructive geophysical methods can be a cost-effective alternative to destructive methods for purposes of site assessment.

The two study sites as shown in Figure 1.1 are located within the New Madrid Seismic Zone. The first study site is located in the Granite City 7.5' quadrangle just east of St. Louis, Missouri. The quadrangle lies on the western portion of the Illinois basin in the St. Louis metro east area. The second site is located near Blytheville, Arkansas in proximity to the epicenters of the 1811-1812 New Madrid earthquakes.

At the Illinois site, borehole control, downhole seismic (DHS), seismic refraction tomography (SRT) and multichannel analysis of surface waves (MASW) data were acquired for the purpose of seismic site characterization.

At the Arkansas site, borehole control, electrical resistivity tomography (ERT), seismic refraction tomography (SRT), and multichannel analysis of surface waves (MASW) data were acquired for the purpose of verifying and mapping a postulated fault.

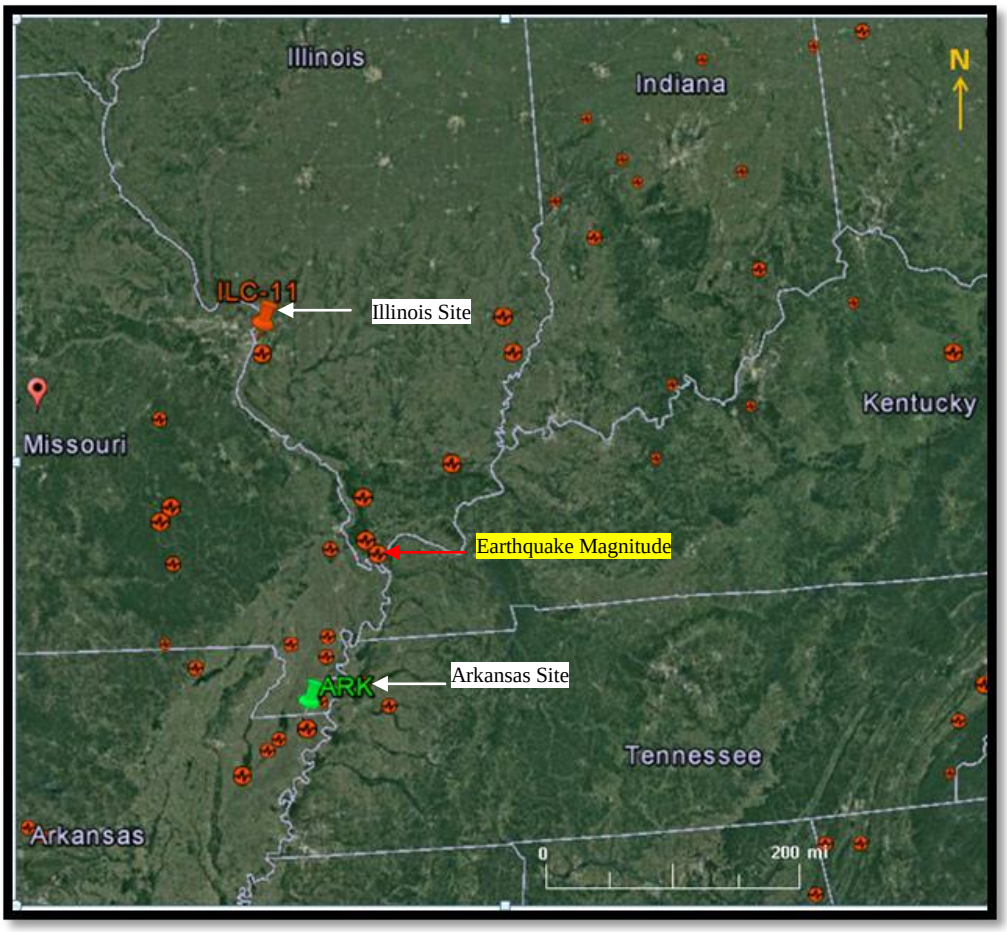

Figure 1.1. Study site locations in the New Madrid Seismic Zone.

2. NEW MADRID SEISMIC ZONE

When the accumulated strain exceeds, the frictional forces, that prevent fault slip due to the rough fault surfaces, fault rupture occurs. It causes the earthquake to happen creating seismic waves moving, and make the ground shake. These waves move away from a hypothetical earthquake hypocenter (Figure 2.1).

Body waves travel through the earth's interior in all directions away from the rupture, while the surface waves move along the earth's surface. The spot underground, where the rock breaks is called the focus of the earthquake. The epicenter of the earthquake is the place right above the focus.

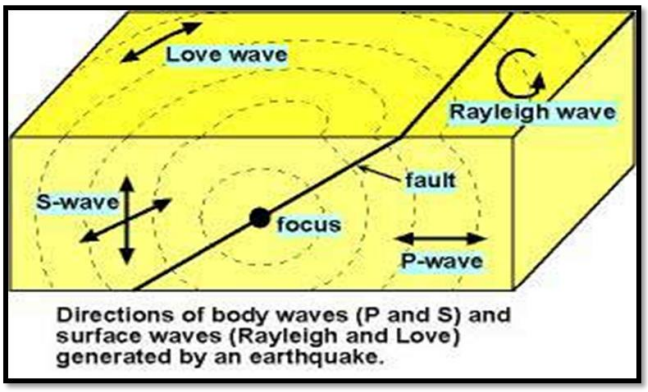

Figure 2.1. Direction of seismic waves generated by earthquake [1].

The new Madrid Seismic zone (NMSZ) is considered to be the most seismically active area east of the Rocky Mountains. Three of the highest magnitude great earthquake reported in recent times in the continental United States occurred on December 16th 1811, January 23rd 1812, and 7 February 7th 1812, near the town of New Madrid in the Mississippi Embayment.

The earthquakes magnitudes are uncertain, but are estimated to have been between MI 7.5-7.8 [2]. The earthquakes caused extensive liquefaction and ground failure in five states: Arkansas, Illinois, Kentucky, Missouri and Tennessee (Figure 2.2).

Earthquakes comparable to the 1811-1812 events could occur at any time in the New Madrid Seismic Zone or perhaps elsewhere in the Mississippi Embayment. Softer unconsolidated soil will amplify seismic ground motion caused by seismic waves resulting in significant damage to infrastructure in an area inhabited by 15 million people.

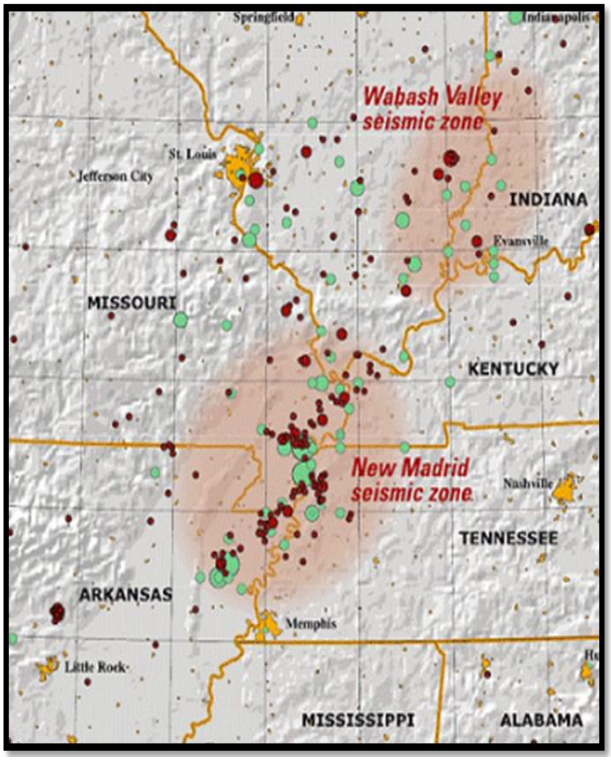

Figure 2.2. The USGS map shows the areas potentially under threat from earthquakes [3].

The St. Louis area earthquake hazards mapping project (SLAEHMP) is producing digital maps (Figure 2.3) that show variability of earthquake hazards, including the local soil conditions affect and the intensity of potential shaking.

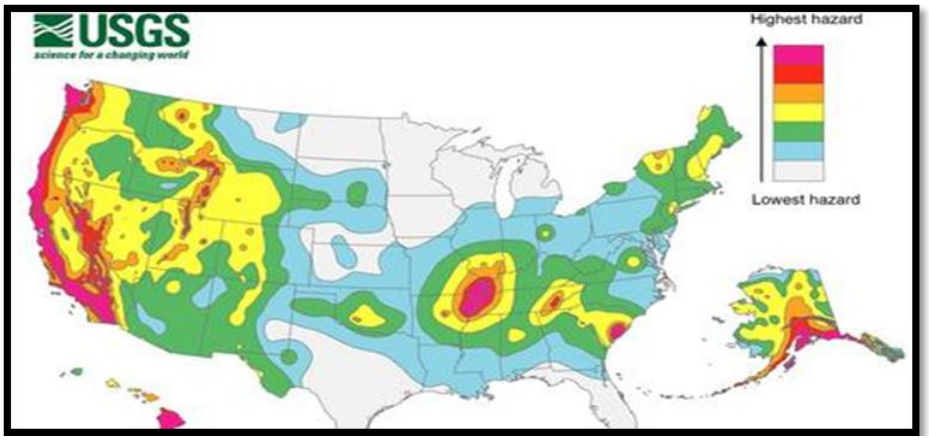

Figure 2.3. National seismic hazard map [4].

Earthquakes can't be accurately predicted, but the intensity and effect of the potential earthquakes can be estimated as shown in Figure 2.4. Seismic shaking (ground motion) tends to increase at the sites are underlain by low density (unconsolidated) sediments, typically characterized by low shear wave velocity (low shear modulus). In order to better predict the ground motion at a site so that structures can be appropriately designed, a reliable model of the dynamic properties (normally shear wave velocity) of the shallow (typically to a depth of 100 ft.) sediment is needed.

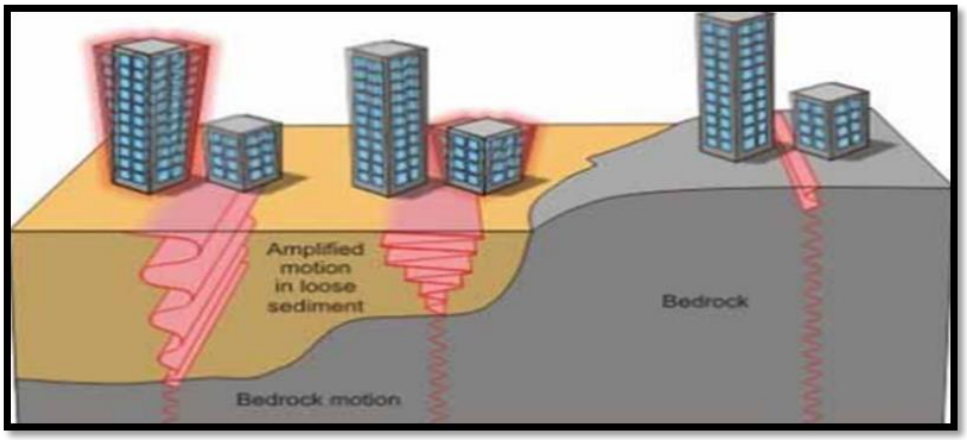

Figure 2.4. Local soil conditions affect the intensity [5].

3. THEORY OF SEISMIC METHOD

3.1. STRESS AND STRAIN

The stress on an object is related to the forces applied on that object as shown in Figure 3.1. These stresses strain the object causing it to deform. Strain is typically measured in terms of relative changes in length, volume or angle. Stress is force per unit area and can be expressed as:

$$\sigma = F/A \tag{3.1}$$

where:

σ is stress (N/m2) or (lb/in2, psi),

F is force (N) or (lb), and

A is area of object (m2) or (in2).

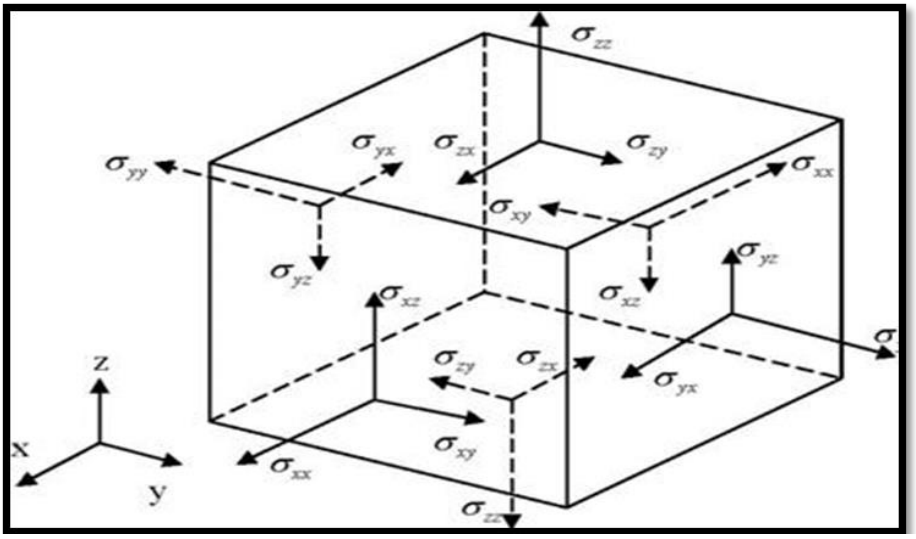

Figure 3.1. Stress acting on the elemental cube [6].

The degree to which the body is deformed (in terms of length) is expressed as:

$$\varepsilon = \Delta L / Lo \tag{3.2}$$

where:

ε = strain,

ΔL is elongation or compression (offset) of the object, and

Lo = initial length of the object.

The body shape will change when external forces are applied to it. Hooke's Law states over the elastic range, stress and strain are linearly related (Figure 3.2). The stress-strain relationship for any material is governed by their elastic moduli variation.

If the applied stress exceeds the yield strength, the stress-strain relationship is no longer linear and the material deforms as a plastic. In this case, the material returns to its original shape when the load is removed. The principle of Hooke's law remains one of the prominent models for elasticity in seismic theory [7].

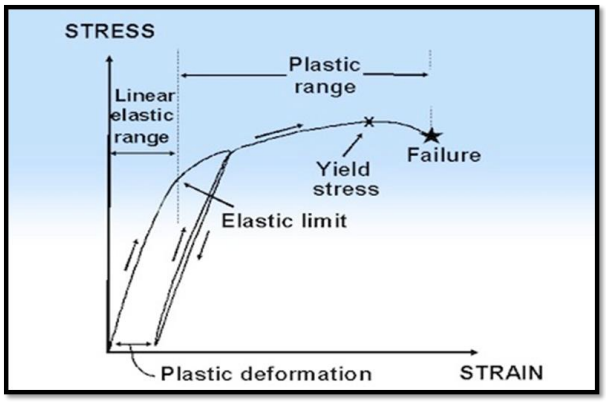

Figure 3.2. Stress and strain relationship [8].

There are four principle elastic moduli: Young's modulus, axial modulus, shear modulus and bulk modulus. The velocity with which acoustic (seismic) energy propagates through a material is a function of these moduli and Poisson's ratio. If one knows the elastic moduli (and density) of a material, one can predict the velocity with which acoustic energy will travel through that material.

3.1.1. Young's Modulus. Young's modulus is the ratio between the tensile stress as (the ratio of the magnitude of the external force F to the cross-sectional area A), to the tensile strain (the ratio of the change in length ΔL to the original length Lo). Young's modulus as shown in Figure 3.3 can be expressed as:

$$E = (F / A) / (\Delta L / Lo) \tag{3.3}$$

where:

E is Young's modulus,

ΔL is change in length, and

Lo is original length.

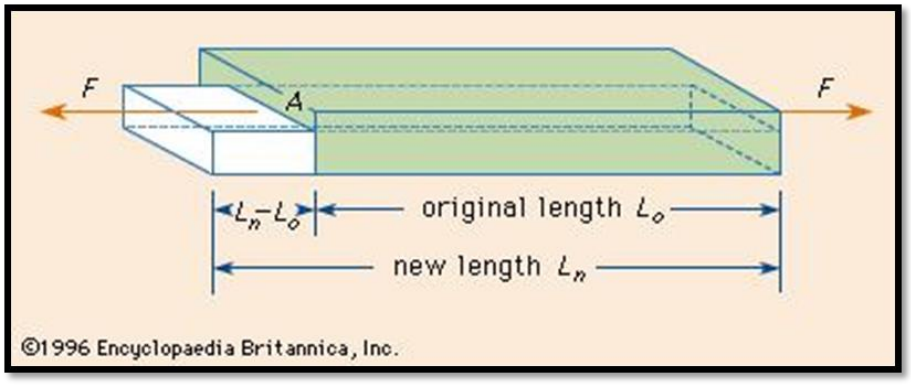

Figure 3.3. Young's modulus diagram [9].

3.1.2. Shear Modulus. Shear modulus as shown in the Figure 3.4 occurs when two opposite forces acting on different plane of the body, the object is subjected to a force tangential to one of its faces while the opposite face is held fixed by another force, the produced strain is the horizontal distance of sheared face by the height of the object. The Shear modulus can be expressed as:

$$G = (F/A) / (\Delta x/L) \tag{3.4}$$

where:

G is shear modulus,

F is tangential force,

A is the area of face being sheared,

Δx is the horizontal distance sheared face moves, and

H is the height of the object.

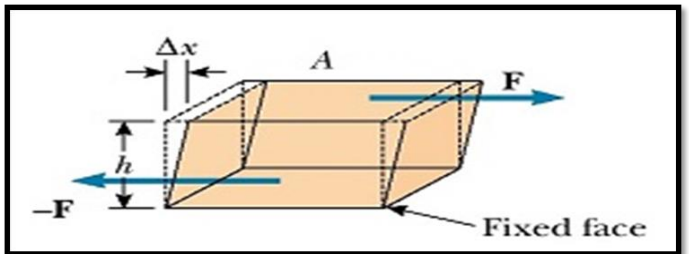

Figure 3.4. Shear modulus diagram [10].

3.1.3. Bulk Modulus. The object in this case as shown in Figure 3.5 is subjected to forces act equally in all of its faces. The volume stress is the ratio of the force on each face to the area.

The body undergoes a change in volume but no change in shape and the volume strain is the ratio of the change in the object's volume to its original volume. The bulk modulus is associated with p-wave propagated.

The bulk modulus can be expressed as:

$$K = (F/A) / (\Delta V/V) \tag{3.5}$$

where:

K is bulk modulus,

F is tangential force,

A is the area,

ΔV is differential change in volume of the object, and

V is initial volume of the object.

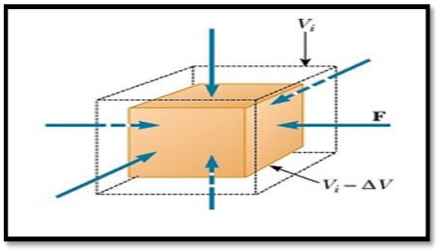

Figure 3.5. Compressed cube in all sides [11].

3.2. TYPE OF ACOUSTIC (SEISMIC) WAVES

The acoustic Seismic waves will be discussed indetail in the following section.

3.2.1. Overview. Seismic waves are a type of oscillation that transports energy from one location to another without the transportation of matter.

They propagate through a medium because of the interaction between the particles of the medium. They are classified into body waves and surface waves.

3.2.2. Body Waves. Body waves are those which travel through the entire volume of the earth. Those waves are non-dispersive and travel at a speed proportional to the material density and modulus.

The propagated wave, the body waves are classified as either compressional waves (p-wave; P stands for primary) or shear waves (S-wave; S stands for secondary).

3.2.2.1 Compressional waves. Compressional waves as shown in Figure 3.6 are characterized by particle motion parallel to the direction of the wave propagation. The velocity of propagation can be expressed in terms of axial modulus and density.

$$V_p = (E/\rho)^{0.5} \tag{3.6}$$

where:

V_p is compressional wave velocity,

E is an axial modulus, and

ρ is a density.

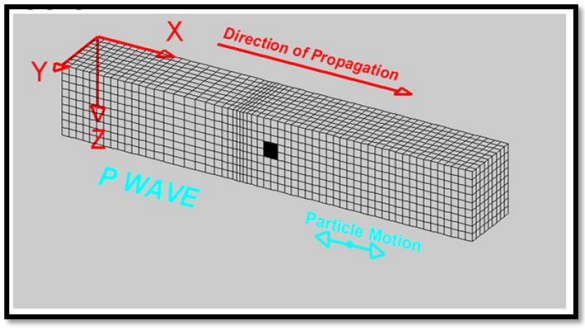

Figure 3.6. Compressional wave propagation [12].

The Compressional wave velocity can also be expressed in terms of the bulk modulus and density [13]:

$$V_p = [(K+4/3G)/ \rho)]^{0.5} \quad (3.7)$$

where:

K is the bulk modulus,

G is the shear modulus, and

ρ is a density.

Table 3.1. Range of velocities for compressional waves in soil and rock [14].

Materials	P-wave velocity	
	ft/s	m/s
Weathered surface	800 to 2000	240 to 610
Gravel or dry sand	1500 to 3000	460 to 915
Sand (saturated)	4000 to 6000	1220 to 1830
Clay (saturated)	3000 to 9000	915 to 2750
Water	4700 to 5500	1430 to 1665
Sea water	4800 to 5000	1460 to 1525
Sandstone	6000 to 13 000	1830 to 3960
Shale	9000 to 14 000	2750 to 4270
Chalk	6000 to 13 000	1830 to 3960
Limestone	7000 to 20 000	2134 to 6100
Granite	15 000 to 19 000	4575 to 5800
Metamorphic rock	10 000 to 23 000	3050 to 7000

3.2.2.2 Shear waves. The second type of body wave is a shear wave or S-wave. Shear waves as shown in Figure 3.7 are characterized by particle motion that is perpendicular to the direction of wave propagation. S-wave is calculated using the equation:

$$V_s = (G/\rho) \tag{3.8}$$

where:

V_s is the shear wave velocity,

G is the shear modulus, and

ρ is a density.

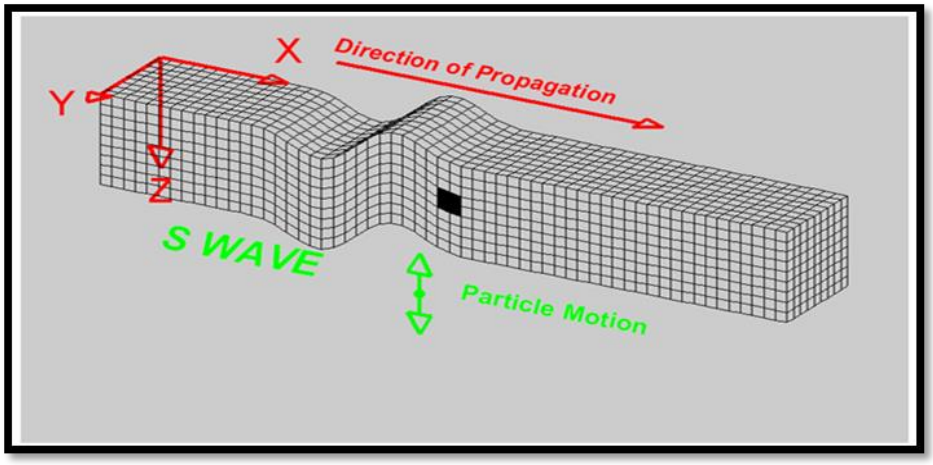

Figure 3.7. Shear wave propagation [12].

3.2.3. Surface Waves. There are two primary types of surface waves: Rayleigh and Love waves. Unlike body waves, surface waves travel only along the earth's surface and are dispersive.

The velocity of propagation is mostly a function of material rigidity, shear modulus and hence shear wave velocity).

3.2.3.1 Rayleigh waves. Rayleigh wave particle motion is usually described as retrograde elliptical. Rayleigh waves (Figure 3.8) motion is both parallel and perpendicular to the direction of wave propagation.

Rayleigh waves are responsible for much of the damage and destruction associated with earthquakes. When a compressional wave source used, more than two-third of total seismic energy generated is imparted into Rayleigh waves [16].

The shear-wave velocity is the dominant parameter influencing changes in Rayleigh-wave phase velocity. It has been shown that Rayleigh-wave phase velocity data can be inverted and used to generate reliable corresponding shear-wave data [17].

Rayleigh-wave velocity is a function of both the shear-wave velocity of the subsurface and the compression-wave velocity of the subsurface.

The interrelationships between Rayleigh-wave velocities within the uniform medium , shear-wave velocities and compression-wave velocities in a uniform half-space are expressed in the following equation.

$$V_R^6 - 8V_S^2V_R^4 + (24 - 16\, V_S^2 / V_p^2)\, V_S^4V_R^2 + 16(V_S^2/ V_p^2 - 1)\, V_S^6 = 0 \qquad (3.9)$$

where:

V_R is the Rayleigh-wave velocity within the uniform medium,

Vs is the shear-wave velocity within the uniform medium, and

V_p is the compression-wave velocity within the uniform medium.

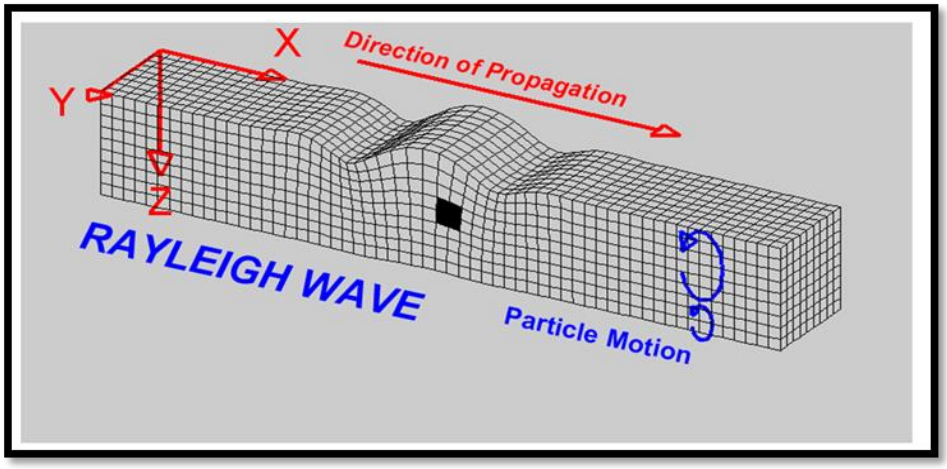

Figure 3.8. Rayleigh waves propagation [12].

Sensitivity studies conducted by several authors, including [17] and [18] have concluded that Rayleigh-wave phase velocities are influenced much less by changes in compression-wave velocity than by changes in shear-wave velocity. (Stokoe, 1994).

3.2.3.2 Love waves. Love waves was named after Edward Hough Love, They are horizontally polarized surface waves which is the second components associated to the shear component, it's tending to be the most destructive wave at the surface of the earth. Love wave and its direction of propagation are shown in Figure 3.9.

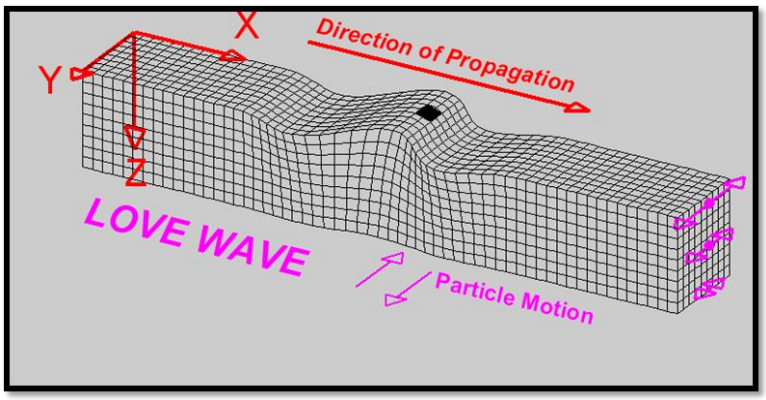

Figure 3.9. Love waves propagation [12].

4. METHODOLOGY

4.1. TOOLS OVERVIEW

Geophysical methods used in this study divided in two categories: destructive and nondestructive methods. The downhole seismic method is the destructive method used in the study area, the downhole seismic measurements of ILC-11 borehole, with depths reached up to 120 feet was performed in 2008 in the Granite City 7.5'quadrangle, where the nondestructive geophysical methods used in this study area include multichannel analysis of surface waves (MASW), seismic refraction tomography (SRT), and electrical resistivity tomography (ERT).

4.2. DESTRUCTIVE METHOD

The downhole seismic surveying (DHS) is the destructive method used in this study . Downhole seismic surveying (Figure 4.1) is an important field method for determining the p-wave and s-wave velocities and other geotechnical site investigations.

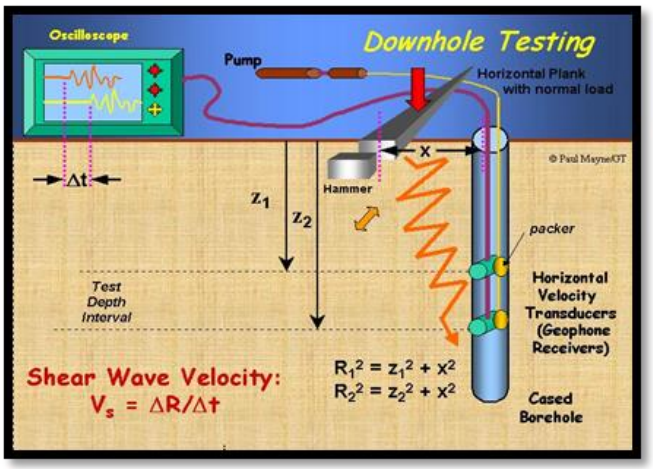

Figure 4.1. Downhole seismic test for shear wave velocity measurements [20].

Downhole allows direct measurements of travel times from a source at the surface to a geophone at depth in a borehole (Figure 4.2). [19] Stated that the interval and average velocities of the borehole surrounding material can be measured. Downhole seismic surveying provide detailed information on the engineering properties of subsurface soils and rock. The velocity profiles obtained from downhole surveys used to construct the site response modeling for earthquake hazard evaluation and structural design.

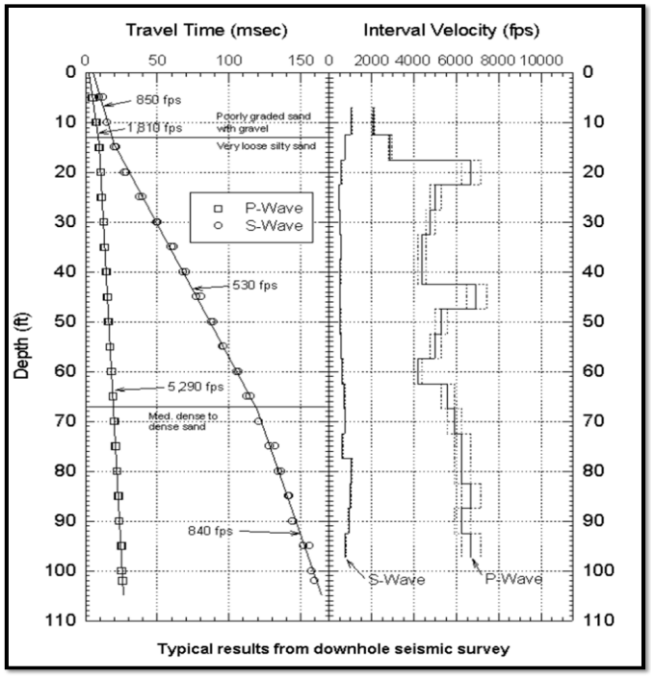

Figure 4.2. Arrival time curve from downhole seismic test for shear wave velocity [21].

4.3. NON DESTRUCTIVE METHODS

Multichannel analysis of surface waves (MASW), seismic refraction tomography (SRT) and the electrical resistivity tomography (ERT) are the nondestructive methods used in this study.

4.3.1. Multichannel Analysis of Surface Waves (MASW). MASW is a noninvasive, continuous profiling method that can study the subsurface to depths more than 100ft depending on the seismic source and site condition.

Rayleigh waves travel along or near the ground surface; these waves are typically characterized by a low velocity, low frequency, and high amplitude that decreases with depth. The Rayleigh waves have a particle motion counterclockwise with respect to the direction of the travel wave; it moves with a rolling motion with the waves across the ocean.

4.3.1.1 MASW theory. Due to the accurate determination of phase velocities for horizontally traveling fundamental modes of the Rayleigh waves, MASW can be used in many different sites successfully [22].

The Rayleigh waves can be assumed as 92% of the shear wave velocity according to [23], so 0.92Vs is the practical value used by the geotechnical engineers for a Rayleigh wave velocity.

The MASW method estimates S-wave velocities by exploiting the Rayleigh wave's dispersive nature through mathematical inversion [17]. Dispersion is the apparent velocity of the surface-wave that depends on the period and reflects the velocity variation with depth. Different frequencies have different velocities.

The *f*k-spectrum method is the most commonly used for the dispersion curve measurements related to the characteristics of surface wave data, or those data analyzed to transform into the *f*k-domain. [24].

The analyzed data can then be used to create the Phase velocity frequency spectrum.

$$Cf = dx/dt = 2\pi f/k \quad (4.1)$$

where:

Cf is the phase velocity,

f is the frequency,

k is the wave number, and

λ is the wave length

4.3.1.2 MASW equipment and tools. The necessary equipment to achieve the MASW survey is including the seismograph, geophones, seismic cables, triggering device, power supply, energy source, field laptop, tape measure, and notebook.

4.3.1.2.1 Seismograph. The seismograph is an instrument used to measure and records the vibrations of earthquakes. Seismographs are capable of recording the intensity, direction, and duration of ground movement in digital form and are thus compatible with digital computers.

The RAS-24 exploration seismograph is powered by 12volt battery, as shown in Figure 4.3.

Figure 4.3. The seismograph with its accessories and 12volt battery.

4.3.1.2.2 <u>Geophones.</u> Geophones, as it shown in Figure 4.4, record motion by measuring the voltage induced in an electrical coil at the movement of a magnet within the coil correction the displacement of the ground.

The induced voltages will subsequently display with respect to time (or distance) as amplitude variations. The generated voltage relates to the ground velocity, not amount of movement. The displacement velocity, or velocity of particles of a medium perturbed by passage of the wave, will be recorded. 4.5 Hz geophones (Figure 4.5) were used for MASW in this study.

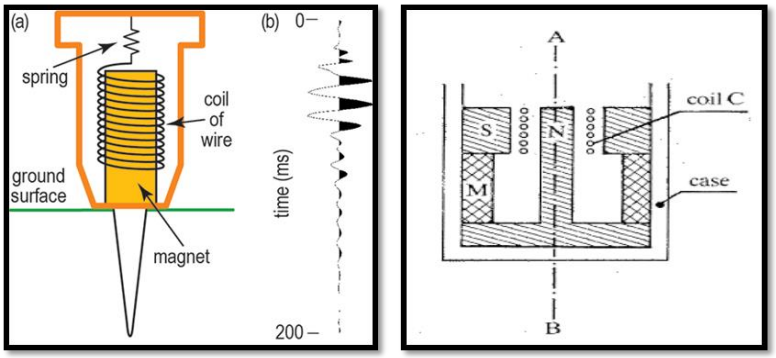

Figure 4.4. Spike coupled Geophone [25].

Figure 4.5. A 4.5 Hz Geophone used for MASW.

4.3.1.2.3 Seismic cable. The seismic cable, also called the spread cable connects the geophones to the seismograph (Figure 4.6). In this study, seismic cable with 5 ft. geophone spacing and 24 connecters was used.

Figure 4.6. Seismic cable with 5ft geophone spacing.

4.3.1.2.4 Triggering device. The trigger device (Figure 4.6) is connected by a cable to the seismograph and attached to the hammer.

When the ground is hit by the sledge hammer, the trigger tells the system to start recording the data, and this will occur when the attached open circuit mechanisms close. The signal is synchronized when the waves have transmitted along the seismograph [26].In some cases where the trigger does not work, a geophone can be used as trigger.

4.3.1.2.5 Energy source. The signal sources for data acquisition with seismic techniques in this study used 20 lb sledgehammer, as shown in Figure 4.7, and steel plate with dimensions of 12 in x 12 in (Figure 4.8) to deliver appropriate impact power into the ground. The sledgehammers used for shallow investigations and signals need to be stacked many times to obtain best results.

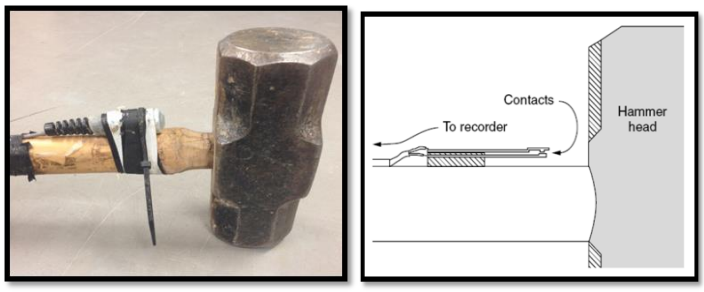

Figure 4.7. A heavy sledge hammer (20 lb.) with a triggering device [27].

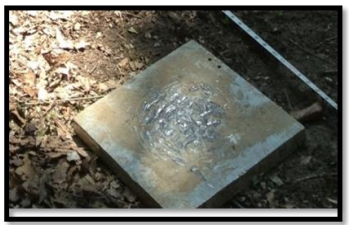

Figure 4.8. The impact steel plate to deliver appropriate impact power into the ground.

4.3.1.3 MASW data acquisition. MASW data acquisition field setup [17] is shown in Figure 4.9. Recent studies have demonstrated that the field parameters for MASW are affected by characteristics of the dispersion curve such as offset distance, receiver, array length, and the seismic energy source that are used for recording surface wave data to obtain a reliable shear wave velocity.

Therefore, the optimum field parameters for the MASW method can be determined by considering the characteristics of dispersion curves, especially the fundamental mode (Figure 4.10).

The suitable characteristics of the fundamental mode of the dispersion curve should be a high amplitude and high signal-to-noise ratio. Field tests using different sets of receiver distances and array lengths have been acquired and processed to ensure that the most consistent and useful dispersion images are obtained.

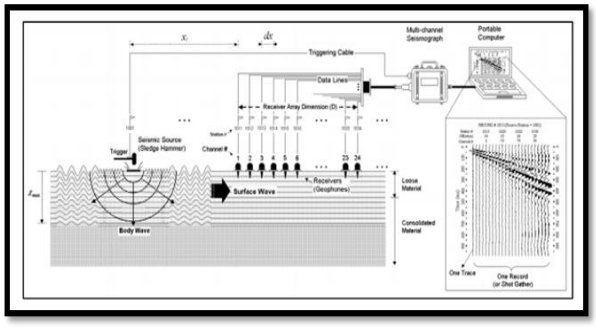

Figure 4.9. MASW data acquisition field setup [17].

4.3.1.4 MASW data processing. The format of the acquired field data must be modified to be consistent with the KGS format using Kansas Geologic Survey (KGS) and transform seismic data from the offset time domain (x-t) to the phase velocity frequency domain (v- w).

Some parameters need to be recognized as well, such as the number of traces, record length and sampling interval. The geometry information such as the offset distance (x1) and the geophone spacing (dx), units employed, trace number of geophone closest to source, and direction of move. The overtone (OT) records (colored dispersion curve data) are generated automatically, and then the dispersion curves will be extracted from overtone image.

A given frequency of Rayleigh waves can be associated with more than one phase velocity, simply because these waves can travel at different velocities for a given frequency. The lowest velocity for any given frequency is called the fundamental-mode velocity (or the first mode), as shown in Figure 4.10.

The next higher velocity above the fundamental-mode phase velocity is called the second-mode velocity (a higher mode), and so on. A series of dispersion curve images will demonstrate the practical selection of optimum offsets.

Finally, the inversion of dispersion curve generates 1-D shear wave velocity profile (Figure 4.10). These initial model approximations are correlated with calculation several times to correct the model until the last proposed iteration, which should represent the truth.

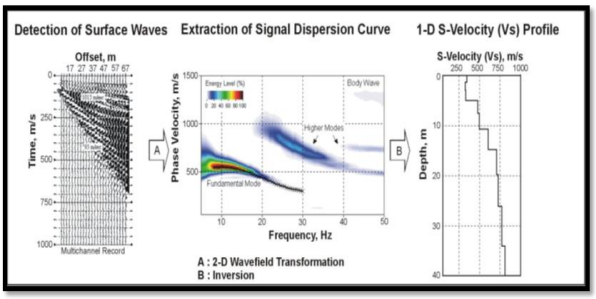

Figure 4.10. A 3-step processing scheme for MASW data [28].

Various sources offsets and spread sizes from an extra-large fixed spread with near and far source offsets were used to generate and examine the corresponding dispersion curve images and estimate which combination of source offsets and spread size provides the optimal image of the fundamental mode of the Rayleigh wave for the survey. A 2-D shear wave velocity map would be constructed, as shown in Figure 4.11.

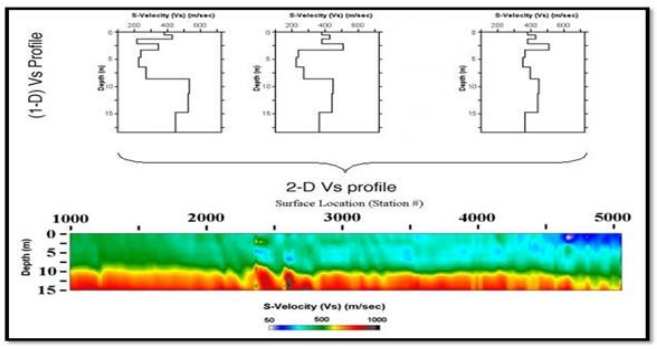

Figure 4.11. Construct a 2-D vs map from a MASW survey [29].

4.3.2. Seismic Refraction Tomography (SRT). Tomographic inversion is generally best used when velocity contrasts are known to be more gradational than discrete, when strong horizontal velocity variations are known to exist, or in extreme topography.

Tomography is currently used in many fields such as geophysics, atmospheric science, and materials science. It uses the mathematical procedure called tomographic reconstruction. Seismic refraction tomography (SRT) is a newly- devolved cost effective technique for site characterization compared to conventional seismic refraction due to the capability of seismic refraction tomography to detect "hidden layers" [30], which cause erroneous interpretation of data. An initial module of the ray paths is constructed to associate with their respective measured travel times close to the true P-wave velocity distribution as well as smoothing constraints [31] in order to achieve reliable results during inversion.

Tomographic inversion displays the data in a mode that is more true to real life by showing gradual transitions of velocities instead of very sharp transitions from one velocity to another. In any surface refraction inversion technique, including tomography, it must be assumed that velocity increases with depth.

If all geometrical data and first break picks have been input, the computer would be able to build a theoretical model close to field data using a different algorithm.

4.3.2.1 SRT theory. Seismic waves travel at different speeds in different materials. When an explosion or an impact occurs in the surface, waves travel away in all direction (Figure 4.12). A ray is an arrow perpendicular to the wave front, indicating the direction of travel at that point on the wave front.

Passage of waves (light or seismic) from one media to another across an interface was first explained in 1678 by Dutch mathematician Christian Huygens. According to the Huygens' Principle, "All points on a wave front can be regarded as point sources for the production of new spherical waves; the new wave front is the tangential surface (or envelope of the secondary wavelets)".

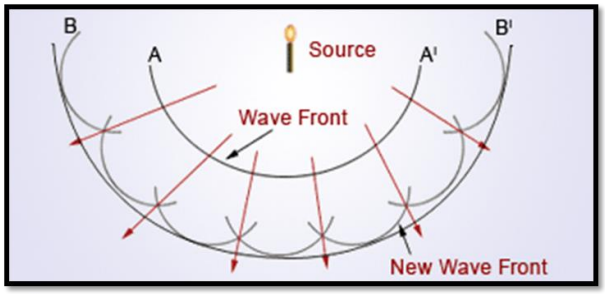

Figure 4.12. Construct a new wave front from the original one [32].

In a uniform medium, the wave front travel in straight paths away from the source but they hit a boundary between fast and slower layers with a reactive called Snell's law (Figure 4.13). Willeberd van Roijen Snell (1580-1626) describes the relationship of energy passing across a boundary between faster and slower media as the basics of the seismic refraction theory.

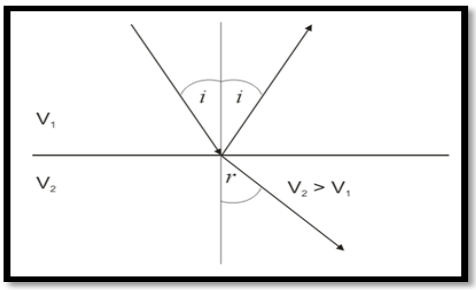

Figure 4.13. The relationship of energy passing across a boundary (Snell's law) [33].

$$Sini/Sinr = V1/V2 \quad (4.2)$$

where:

i is angle of incidence,

r is angle of refraction,

V1 is velocity of the first layer, and

V2 is velocity of the second layer.

If V2>V1, then as i increases, r increases faster, the critical angle where it is refracted at 90° and travels along the boundary on the fast layer.

$$Ic = Sin^{-1} V1/V2 \quad (4.3)$$

When energy arrives to the boundary, some of energy is refracted in a lower layer to speed up and slow down depending on a media at the critical angle (Figure 4.14), where refractions at 90° travel along the boundary on the fast layer.

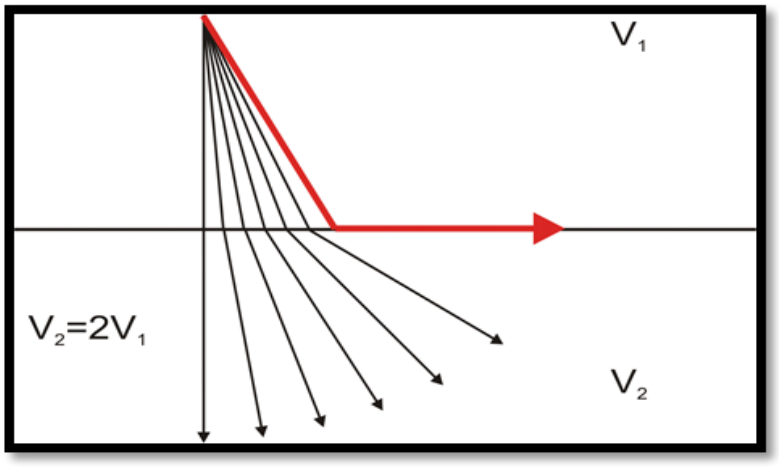

Figure 4.14. The energy where is refracted at 90° travel along the boundary on the fast layer [33].

If the ray passes more than the critical angle, all the energy will reflect back to the surface; this is known as a super critical angle. An angle less than a critical angle, which is called subcritical angle, have most of the energy refracted to speed up travel in the lower layer with less energy reflected upwards.

The critical angle marks the angle with away is refracted parallel to the boundary and travels along the upper surface sending a series of rays known collectively as head waves back to the surface with the angle of the initial direct wave.

Seismic refraction uses the first-arrival energy only (Figure 4.15). The rest of the wave form is ignored. If low-velocity layers are anticipated and/or if the subsurface is relatively complex, refraction tomography should be the tool of choice.

In general, the tomographic technique is reliable for realistic synthetic models. These include subsurface models with gradual change in velocity and variation in lateral velocity.

Snell's law states that the break in slope of the below travel time curve as shown in Figure 4.15 and Figure 4.16, which occurs at the crossover distance marks the point at which travel times refracted from V2 overtake direct arrivals traveling through V1. The equation for the first segment T1 is:

$$V1=X/T1 \tag{4.4}$$

where:

v1 is the velocity of the direct compressional wave, and

x is the distance from the source to the receiver.

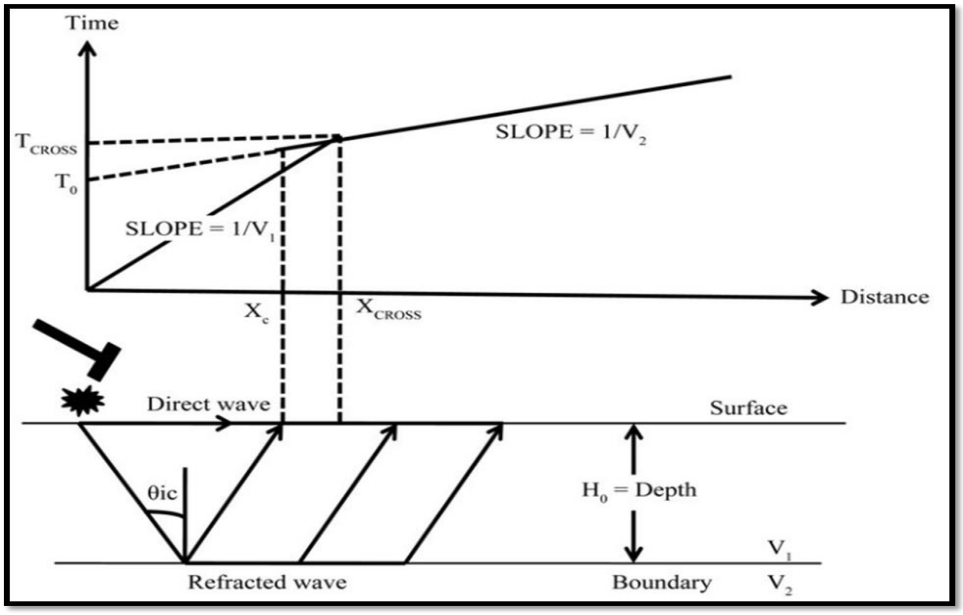

Figure 4.15. Diagram of compressional wave and travel time curves [34].

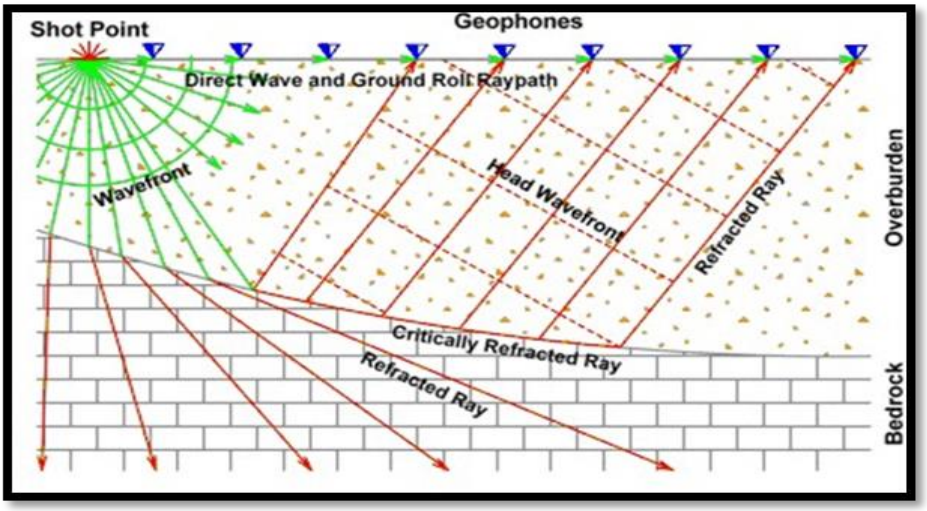

Figure 4.16. Seismic refraction geometry [35].

The SRT is also known as velocity gradient or diving-wave tomography [36]. It uses the first arrival travel time of seismic waves. When a seismic wave encounters a velocity discontinuity, some of the energy is reflected and some is refracted, but this study only focuses on refracted energy.

4.3.2.2 SRT equipment and tools. The same MASW equipment was used to achieve the seismic refraction tomography (SRT) survey including the seismograph, geophones, seismic cables, triggering device, power supply, energy source, field laptop, tape measure, and notebook, only 14HZ geophones as shown in Figure 4.17 were used in SRT.

4.3.2.3 SRT data acquisition. SRT involves more complex mathematic algorithms to construct more reasonable model. In the field procedure, SRT in generally needs more shot points than standard seismic refraction survey to obtain high resolution. The SRT data acquisition was performed using 24-channels seismic equipment Seistronix RAS - 24, with the system dynamics of 144 dB, of 24 bites resolution and 14Hz vertical geophones.

Figure 4.17. A 14 Hz Geophones used for SRT.

The optimum number of stacking impacts can be determined when there is little change in signal-to-noise ratio (S/N) in the displayed seismic record during the stacking.

Seven vertical stacks were sufficient, but this number should increase as the ambient noise level increases and/or total receiver array length (D) increases.

4.3.2.4 SRT data processing. SeisImagerTM is the master program used for a nonlinear travel time tomography. It described by Hayashi and Takahashi [37]. It consists of four modules for refraction wave data analysis. The individual modules are PickwinTM, PlotrefaTM, WaveEqTM, and GeoPlotTM.

Many of methods were used to calculate the true velocities and thicknesses of the subsurface layers, [38], [39] used the wave front method where the delay - time method was tested by [40], [41], and others. The third method is the Plus minus method was used by Hagedoorn, [42], and the generalized reciprocal method was discussed by Palmer, [43].

In this study, the time-term method used where assumed constant velocities in each layer, and the travel time changed by changes in depth of the interface. The tomographic method requires an initial velocity model such as what it has been formed from the time term method.

The model made up of many cells, where rays are traced through this model and the velocities in each cell are changed to improve the fit until acceptably small errors in travel time are achieved.

SeisImagerTM is the master program used for a nonlinear travel time tomography. It described by Hayashi and Takahashi, [37]. It is the first break picking module. The general flow of Pickwin is depicted in the flow chart as shown in Figure 4.18. When the first arrivals have picked for all shots with in the spread line, the green lines show the lines of the first break picks from the previous files.

The pinky red file shows the first arrivals have picked from the current shot record. When all files have been picked, the first break picks file will be saved.

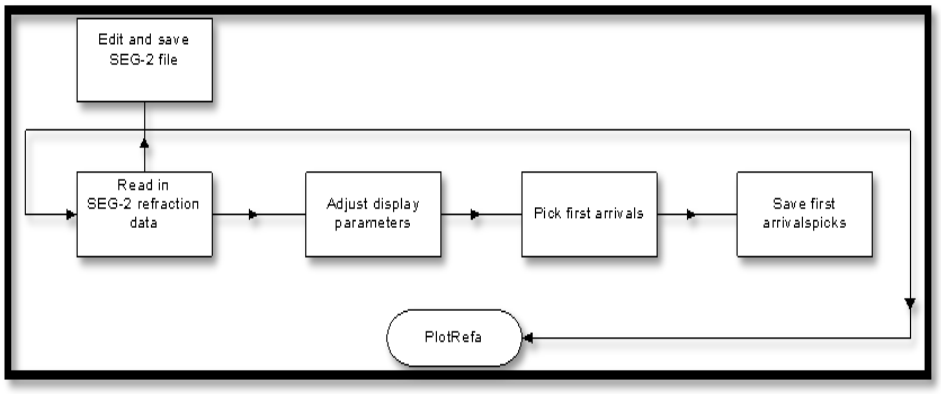

Figure 4.18. The general flow of Pickwin software.

Plotrefa is the interpretation module of SeisImagerTM in which takes the output of Pickwin as input, and through the application of one of the three used techniques. Those programs provide a velocity cross section and include many useful tools for facilitating data interpretation.

When the first arrivals have picked for all shots with in the spread line as sown in Figure 4.19, the green lines show the lines of the first break picks from the previous files. The pinky red file shows the first arrivals have picked from the current shot record. Plotrefa includes the capability of creating a custom velocity model for forward modeling purposes. Initial model can be created as a simple layer-cake, and then customize it further using the editing technique once the model completed.

It may use the ray tracing routine to compute theoretical travel times for the model. Calculating the synthetic travel times by execute. The travel times will be calculated and displayed along with the observed data, along with the RMS error.

Graphically representation of the data will be done by transform the travel time information in to time distance (XT) graph.

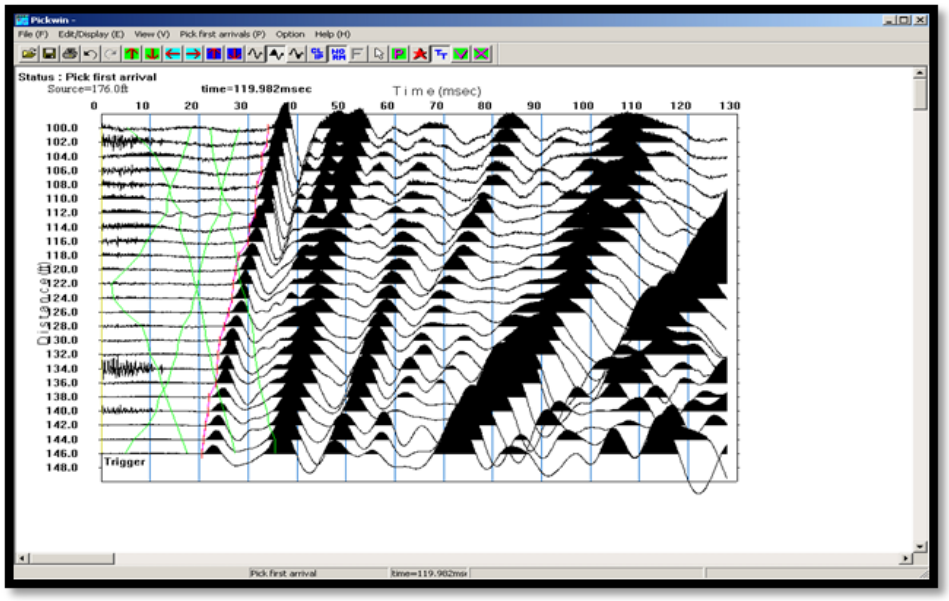

Figure 4.19. A current shot record shows travel time curves.

Tomographic inversion is the third interpretation technique provided by Plotrefa. This method starts with an initial velocity model (generally generated by a time-term inversion), and iteratively traces rays through the model with the goal of minimizing the RMS error between the observed and calculated travel times. Figure 4.20 shows flow chart of typical flow of a tomographic inversion:

The best way to generate the initial model is to do a quick time-term inversion of the data to overrides all of the other manual settings including the minimum and maximum velocities.

If you have done a reasonable time-term inversion, the minimum and maximum velocities from this should provide a good tomographic inversion.

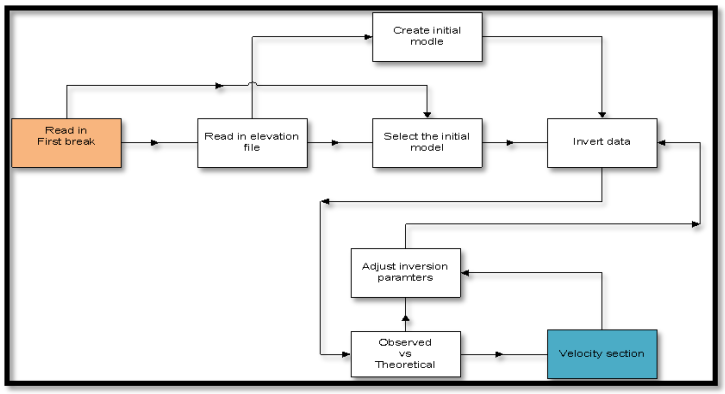

Figure 4.20. The typical flow of a tomographic inversion.

After doing the inversion, it is possible to change the minimum and maximum velocities and re-invert if necessary, the inversion will begin using the selection parameters either with default inversion parameters or setting the parameters manually, when the inversion is complete, the velocity model will be displayed and the agreement between the calculated and observed data of the travel time curves could be displayed.

In extreme topography, converted the tomogram to a layered model to better represent the layered nature of the geology.

Particularly at assignments difficult layers and the tomographic inversion achieved with the default parameters, the inversion can be set the parameters manually to modify the tomographic inversion parameters.

Tomography divides the velocity model into cells of constant velocity as shown in Figure 4.21, and then traces rays through the model.

The number of nodes defines the density of rays, The program automatically assigns a thickness to the bottom layer of an interpreted velocity model. But in a refraction survey, there is insufficient information to actually determine the thickness; it is therefore assigned arbitrarily.

By drawing the bottom layer with a certain thickness, it can give the impression that this thickness is known. It is therefore sometimes desirable to manually define the base of the bottom layer. One way to deal with this is to determine the maximum thickness of the bottom layer by estimating and assuming a maximum velocity of the layer below it, and using a crossover distance equivalent to the greatest shot-geophone distance used, and then computes the maximum depth from the following equation:

$$\text{Depth}=Xc/2*[(Vn+1-Vn/Vn+1+Vn)]^{0.5} \quad (4.5)$$

where:

Xc is the assumed crossover distance,

Vn is the velocity of the bottom layer, and

Vn+1 are the assumed maximum velocity.

It is often useful to convert synthetic travel time data calculated from a synthetic model into observed data assuming the synthetic data is actually real data, allowing to treat it as such, this is a necessary step if wishing to invert this synthetic data and compare the resulting model to the original input model.

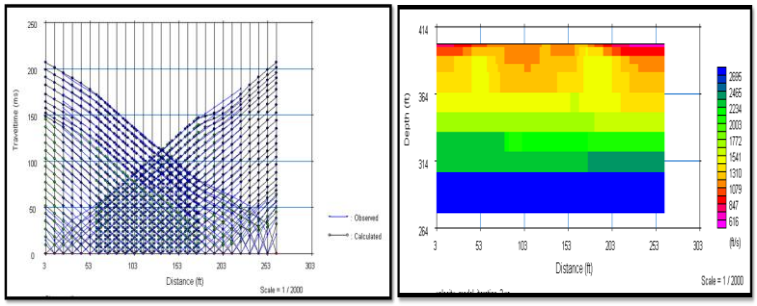

Figure 4.21. A step processing scheme for SRT data inversion.

GeoPlot software. GeoPlot is a window program for the processing and presentation of geophysical data collected from a variety of instruments including: resistance meters, gradiometers, magnetometers, EM instruments, and seismic data.

4.3.3. Electrical Resistivity Tomography (ERT). The electrical resistivity surveying is more than 100 years old and is one of the most commonly used geophysical exploration methods [34].

It has been used to image targets from the millimeter scale to structures with dimensions of kilometers [44], [45]. It is widely used in environmental, engineering and mineral exploration [46] surveys. The basic concept of the Surface electrical resistivity surveying is based on the generation of electrical potential difference by injecting a current in to the earth through a pair of current electrodes.

The common linear arrays of the electrodes as shown in Figure 4.22 are the pole-pole array, dipole- dipole array, schlumberger array and the wenner array.

The variation of resistivity with depth is modeled using forward and inverse modeling computer program. ERT profiles consist of a modeled cross-sectional (2-D) plot of resistivity (Ω·m) versus depth. Figure 4.23 shows the resistivity of different rock types.

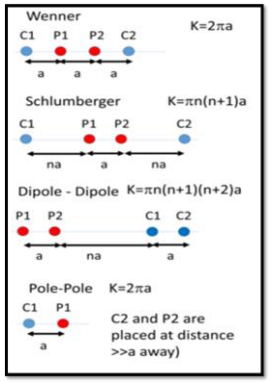

Figure 4.22. Electrode array configurations for resistivity measurements [47].

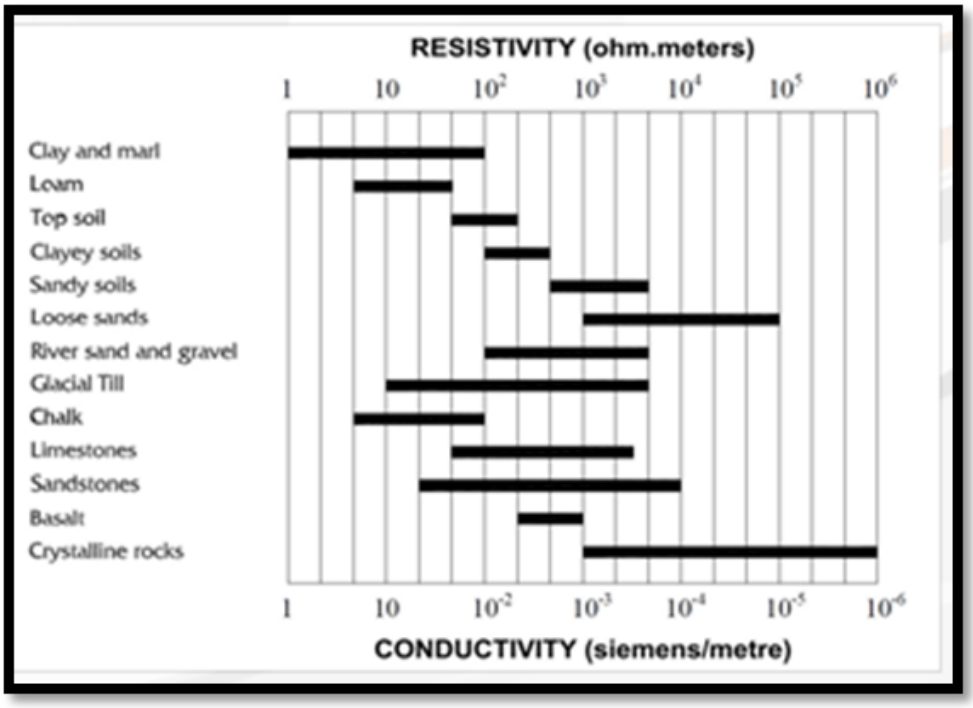

Figure 4.23. Resistivity of different rock types [48].

5. ILLINOIS CASE STUDY

5.1. LOCATION AREA

The study area is located in the Granite City 7.5' quadrangle which is just east of St. Louis, Missouri, the quadrangle lies on the western portion of the Illinois basin in the Metro east St. Louis area.

As shown in Figure 5.1, the Granite City is one of the 29 quadrangles in the St. Louis urban area and one of the four priority quadrangles designated for initial earthquake hazard mapping [49].

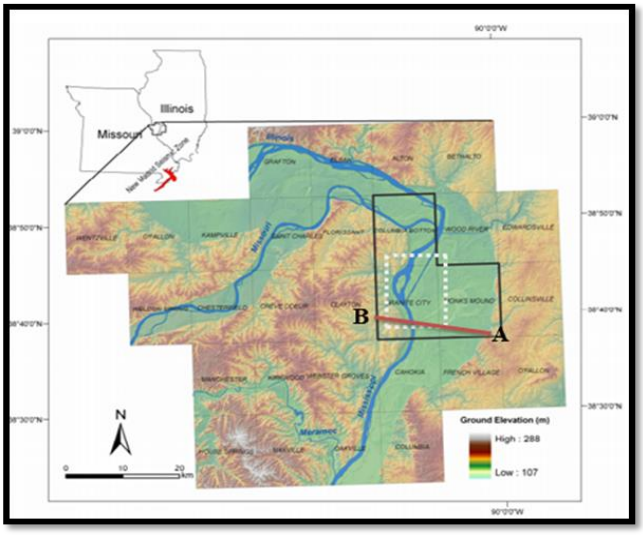

Figure 5.1. Location map of the study area, dashed line [51].

This area is located within earthquake seismic sources, the new Madrid seismic zone (NMSZ) in the upper Mississippi embayment and the Wabash Valley seismic zone (WVSZ) in southeastern Illinois, which have produced prehistoric and historic earthquakes.

This case study used the geophysical nondestructive techniques, the data were acquired to evaluate of using a combination of two acoustic methods, seismic refraction tomography (SRT) as a new devolved cost effective technique for site characterization compared to conventional seismic refraction due to capability of Seismic refraction tomography to detect “hidden layers”,[30] which cause erroneous interpretation of data.

An initial module was constructed for this site closed to the true P-wave velocities distribution as well as smoothing, constraints [31], in order to achieve reliable results during inversion. The second acoustic method is the multi-channel analyses of surface waves (MASW) using a dispersive characteristics of Rayleigh waves from phase velocity versus frequency plot [50].

The p-wave and s-wave velocities were measured and enabled the determination of elastic moduli (Young's modulus, shear modulus, and bulk modulus) indirectly and non-destructively, those moduli are very important parameters for understanding the dynamic behavior of soil and rock layers that helps to evaluate suitability of ground for many structures. The average shear wave velocity for the top 100 ft of soil (Vs100) has been determined at all the section 2D and not only in the middle as 1D, that could be used to verify the lateral change of the most important parameters for the seismic site characterization to use for earthquake hazards assessment and also to demonstrate the sites classes according to the NEHRP and IBC standards. One borehole site were selected in the Granite City 7.5’quadrangle in southwestern of Illinois for further assessment due to available information about primary wave velocities (v_p), shear-wave velocities (v_s) and Poisson’s ratio. The location of the selected borehole given by the coordinates -90.1653, 38.64 at the Mississippi River Bridge to the east of St. Louis.

5.2. GEOLOGY AND STRATIGRAPHY

The Granite City 7.5' quadrangle is just east of St. Louis, Missouri, the quadrangle lies on the western portion of the Illinois basin in the Metro east St. Louis area, bedrock does not outcrop on the Illinois portion of this quadrangle. Holocene and Quaternary units along the flood plain of the Mississippi river cover the entire Illinois portion.

This surficial material ranges in thickness from less than 50 ft near the chain of rocks canal to approximately 125 ft along the eastern half.

According to borehole data provided by the Missouri and Illinois geological surveys as shown from Figures 5.5, 5.6, 5.7, and 5.8, more than 100ft of sand with some gravel resting over Mississippian limestone, the depths to bedrock are generally about 96ft to 128ft, the loess is thickest (up to 93 ft) at the bluffs immediately east of the Mississippi river valley (Figure 5.2), and thins to the east and northeast.

The Illinois portion of the quadrangle is underlain by the Ste. Genevieve limestone and St. Louis limestone (Figure 5.3) throughout the majority of the quadrangle with major material types includes silty, clayey, sandy and gravelly alluvium [52]

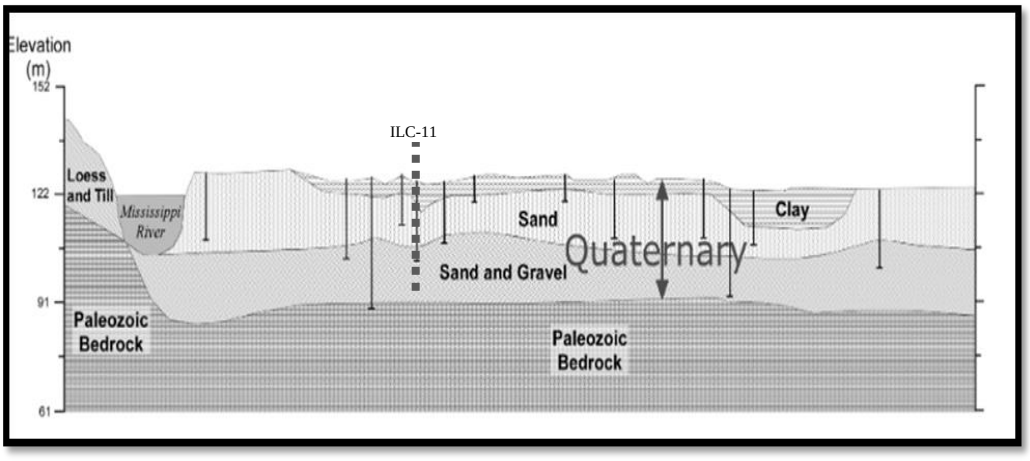

Figure 5.2. B-A cross-section of surficial geology in the study area [52].

Table 5.1. Geologic and stratigraphic units in Missouri [53].

System	Series	Formation	Thickness (ft)	Thickness (m)
Mississippian	Meramecian	Ste. Genevieve Formation	1 – 4	0.3 – 1.2
		St. Louis Formation	0 – 50	0 – 15
		Salem Formation	100	46
		Warsaw Formation	40	12
	Osagean	Burlington-Keokuk Formations	100 – 150	30 – 46
		Fern Glen Formation	30 – 50	9 – 15
	Kinderhookian	Chouteau Group Undif.	15	4.5
Unassigned Devonian-Mississippian		Bushberg Formation	10	3
		Glen Park Formation	15	4.5

5.3. METHODOLOGY AND DATA

The avalaible borehole data and the methodology are shown as follows:

5.3.1. Borehole Data. The borehole data of the ILC-11, with depths reached up to 120 ft that performed in 2008 in the Granite City 7.5'quadrangle in Southwestern of Illinois, are shown in Figures 5.4, 5.5, 5.6, and 5.7.

These data with the cross-section B-A are considered as a ground truth for all the subsurface geophysical techniques used in this study area.

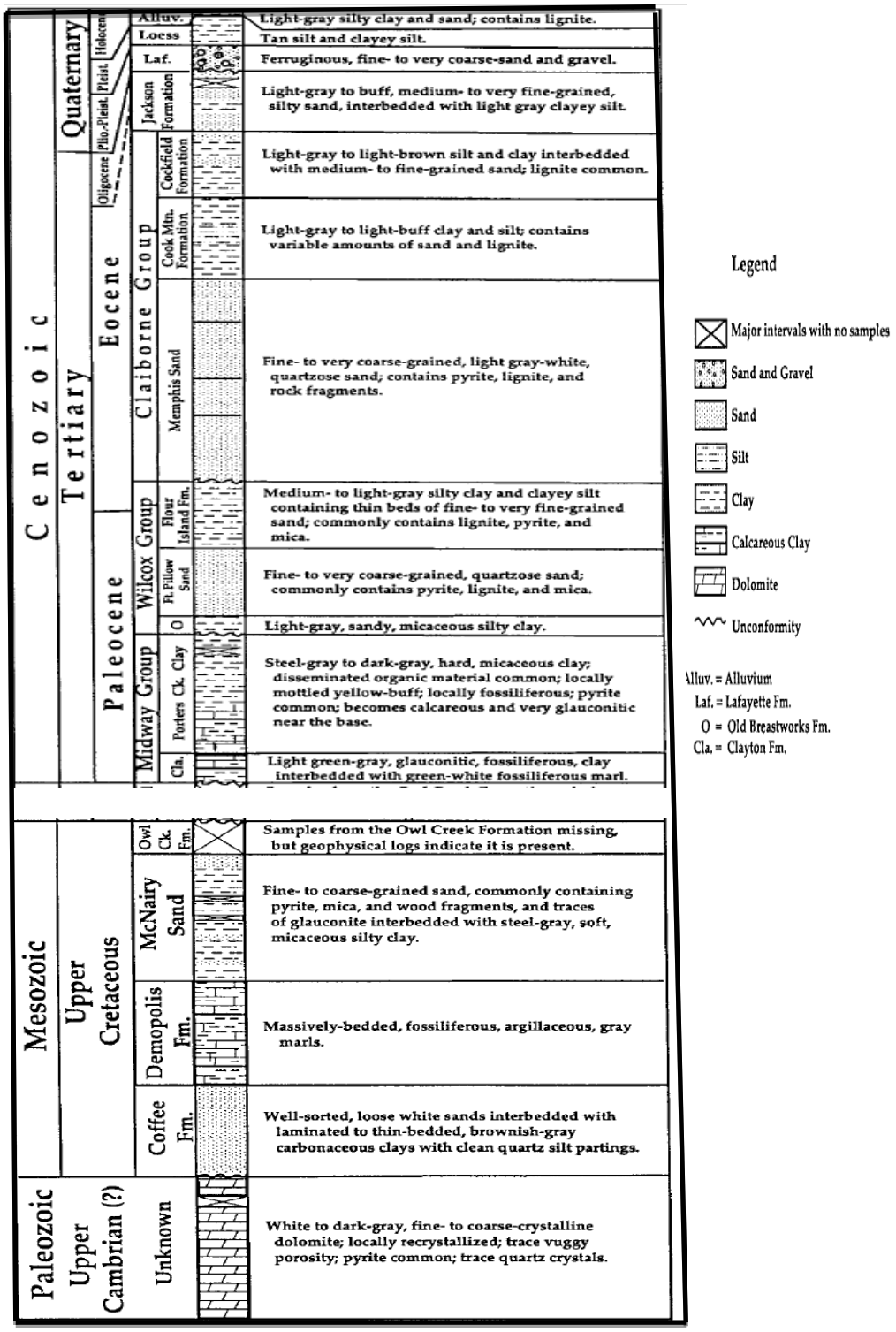

Figure 5.3. Geologic column for the New Madrid seismic zone [54].

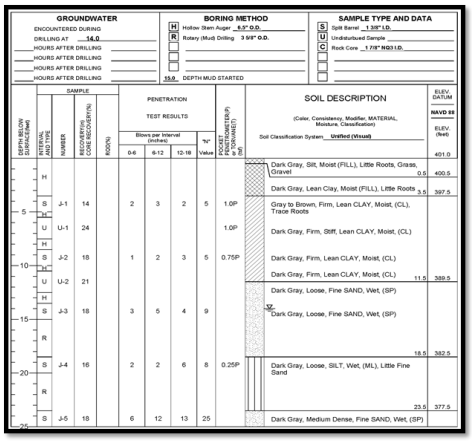

Figure 5.4. Soil description of the borehole number ILC-11, (0 – 25 ft.) [55].

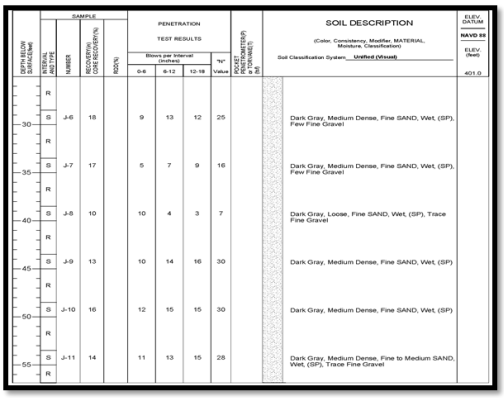

Figure 5.5. Soil description of the borehole number ILC-11, (30 – 55 ft.) [55].

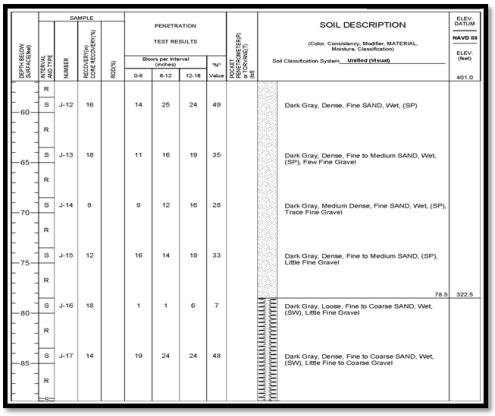

Figure 5.6. Soil description of the borehole number ILC-11, (55 – 85 ft.) [55].

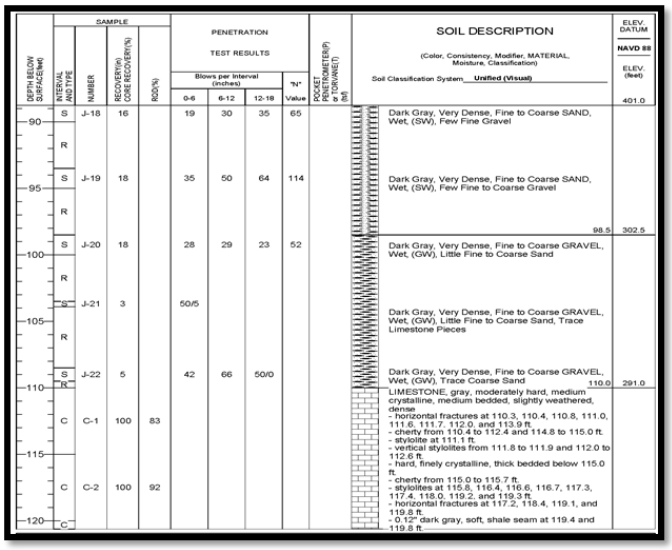

Figure 5.7. Soil description of the borehole number ILC-11, (90 – 120 ft.) [55].

5.3.2. DHS Test. Arrival time curves from downhole seismic test (Figure5.8), by Geotechnology, INC for the borehole ILC-11, Mississippi River Bridge, St. Louis, Missouri, with depths reached up to 120 ft that performed in 2008 in the Granite City 2008.

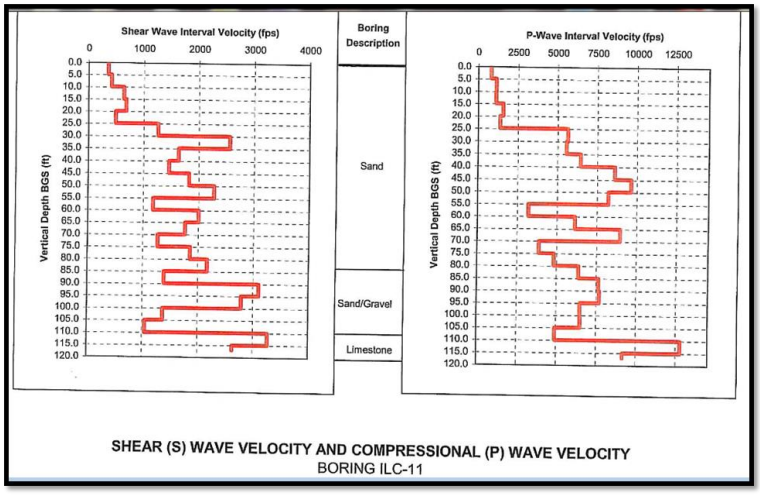

Figure5.8. Pseudo 1-D S-wave velocity and P-wave velocity model profile using DHS [55].

5.3.3. SRT Survey. Seismic refraction tomography (SRT) has been applied in this study where data have been acquired and processed.

5.3.3.1 SRT data acquisition. The SRT data acquisition was performed using 24-channels seismic equipment Seistronix RAS - 24 (Figure 5.9).

Table 5.2. Downhole seismic test results for the tested site ILC-11[55].

Depth (ft/)	S-velocity (ft/sec)	P-velocity (ft/sec)	Poisson's Ratio
5	354.9	812.5	0.382
10	414.1	1134	0.423
15	637.2	1118.9	0.260
20	679.6	1567.4	0.384
25	492	1373.5	0.426
30	1260.2	5645	0.474
35	2560.1	5549.6	0.474
40	1633.1	6443.9	0.466
45	1458.7	8597.1	0.485
50	1825.3	9633.8	0.481
55	2281.6	8196.7	0.458
60	1177.7	3192.4	0.421
65	2004.8	6122.4	0.440
70	1758.7	8964.2	0.480
75	1268.3	3882.2	0.440
80	1857.3	4831.2	0.413
85	2165	6392.6	0.435
90	1386.9	7650.7	0.483
95	3104	7698.2	0.403
100	2792	6490.8	0.386
110	1048.3	4930.1	0.476
120	2629.7	9172.5	0.455

The sampling interval used is 0.25 millisecond and recording time is 0.25 millisecond. The seismic refraction survey line (Figure 5.10) is 235 ft using 14 Hzl geophones with 5 ft geophone spacing as shown in Figure 5.16.The Offset forward and backward distances were equal 60 ft.

The signal sources for data acquisition used a heavy sledge hammer (20 lb.) and the impact steel plate with dimensions of 1ft x 1ft and seven vertical stacks were sufficient to get a good first arrival record. 24 shot points with 10 ft. as a distance between each shot were done for the survey line.

Figure 5.9. Refraction seismic tomography (SRT) acquisition field data.

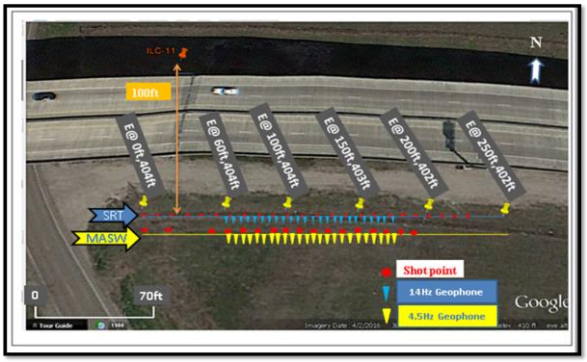

Figure 5.10. Location of the shot points for SRT traverse.

5.3.3.2 SRT data processing. SeisImagerTM is the master program used for a travel time tomography. As mentioned before, PickwinTM and PlotrefaTM will be used for data processing.

The geometry parameters of the 27 files were edited in the survey line as shown in the example Figure 5.11.

When picking first breaks, it is often helpful to display the first break picks of prior records in the survey as a reference. An example of this is shown in Figure 5.12.The red line indicates the first breaks of the current record, while the green lines represent the first breaks of several prior records from the same seismic line.

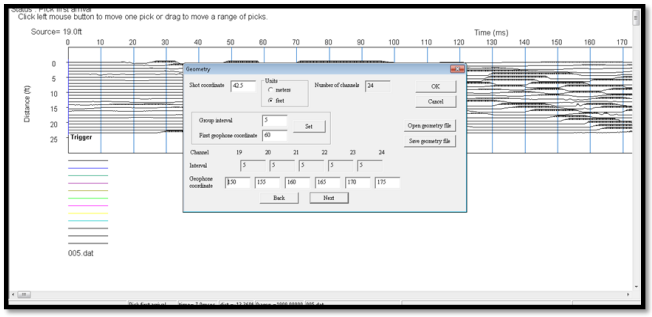

Figure 5.11. Edit source/receiver locations for each record.

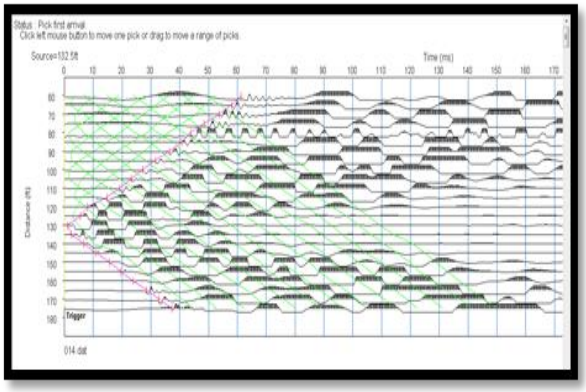

Figure 5.12. Picking first arrival from a seismic wave record showing travel time curves.

The second portion of refraction processing or the inversion portion will be starting using Plotrefa (seismic interpretation program), Figure 5.13 shows a travel time vs distance data plot was displayed, each change in slope represents a layer of increasing velocity.

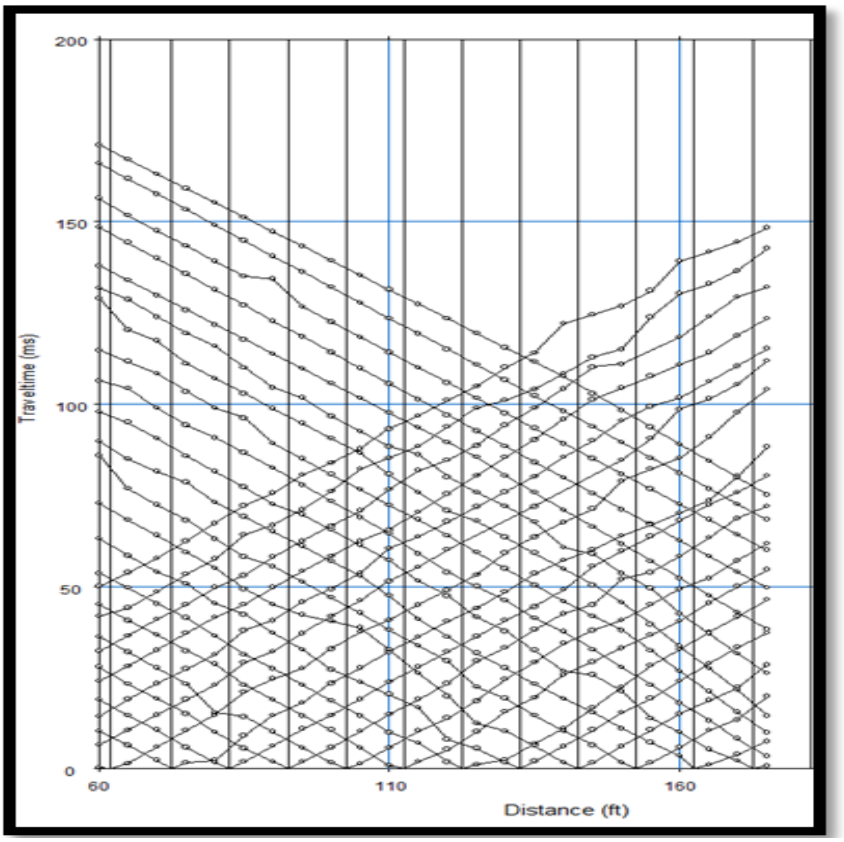

Figure 5.13. The observed first arrival curves.

Under time-term inversion, assign layer 2 arrivals as shown in Figure 5.13. The data points turn red. Click the closest point to the shot on each branch of each travel time curve that was refracted, the points turn green to show they have been selected as layer 2. Points remaining red are layer 1 (direct wave). If there is evidence for a third layer or more in the data, should be assigned. Time-term inversion then will be applied.

To calculate the synthetic travel times as shown in Figure 5.14, simply click on “Execute”. The travel times will be calculated and displayed along with the observed data, along with the RMS error, the goal of minimizing the RMS error between the observed and calculated travel times is to get more accurate results from the model. by retracing and execute ,the data set will shows which points in the subsurface actually have been sampled to give a greater degree of confidence in the accuracy of the data.

By displaying velocity section, the observed travel time curves and the theoretical travel time curves based on the module which created after retracing routine and have been reverse calculated as a result of the retracing.

Ideally, the observed data should exactly match the calculated curves as shows in Figure 5.14 and the difference between the two is representing as the RMS error.

The better of seismic data is more accurate first break have been picked, the calculated curves will much more closely match the position of observed field data.

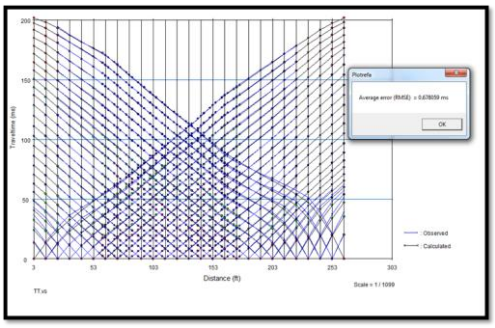

Figure 5.14. Illustrates the difference between calculated and observed first arrivals.

The Trimble® GeoXT Handheld delivers positioning accuracy in challenging GNSS situations is used to determine whether an earth is flat or had any elevation information.

The measured relative or absolute geophone elevations in the study line show a little small variation as shown in Table 5.3 and Figure 5.15 so, the array line assumed as a horizontal subsurface, where Figure 5.16 is showing the site map include the elevations of marked testing locations, SRT traverse and MASW traverse.

Figure 5.15. GeoExplorer 6000 Series.

Table 5.3. Point locations and elevations along the line survey at ILC-11.

Point	Distance (ft)	Latitude	Longitude	Elevation (ft)
1	0ft	38.64909	-90.1653	404.682
2	60ft	38.6491	-90.1651	404.785
3	100ft	38.64911	-90.1649	404.580
4	150ft	38.64912	-90.1648	403.661
5	200ft	38.64913	-90.1646	402.736
6	250ft	38.64914	-90.1644	403.391

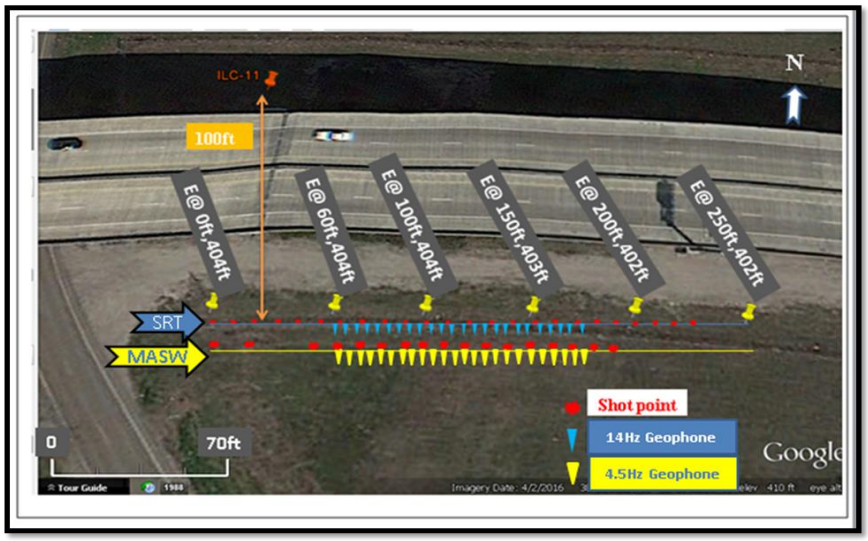

Figure 5.16. Site map showing the elevations of marked testing locations.

The Inversion using parameters that have been setting manually is favorable if the tomographic inversion achieved with the default parameters needs improvement, it may modify the tomographic inversion parameters by setting the parameters' manually as shown in Figure 5.17. The 2-D P-wave velocity model profile from SRT inversion is shown in Figure 5.18.

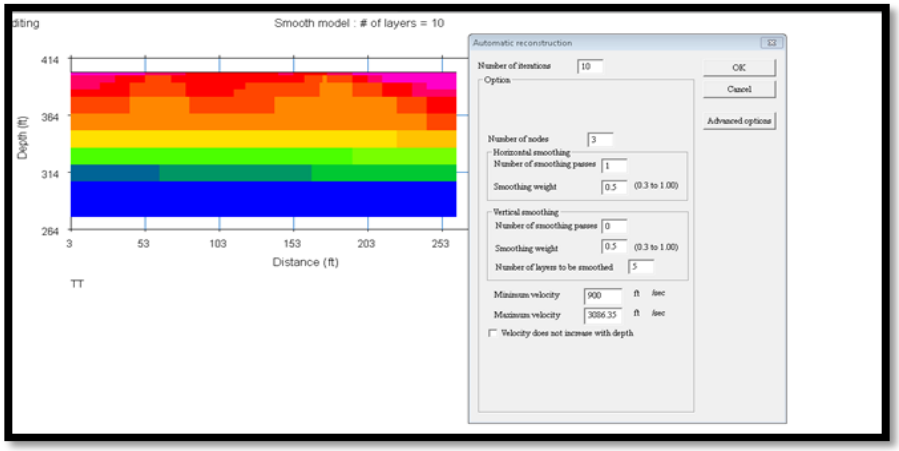

Figure 5.17. The synthetic velocity model for the test site.

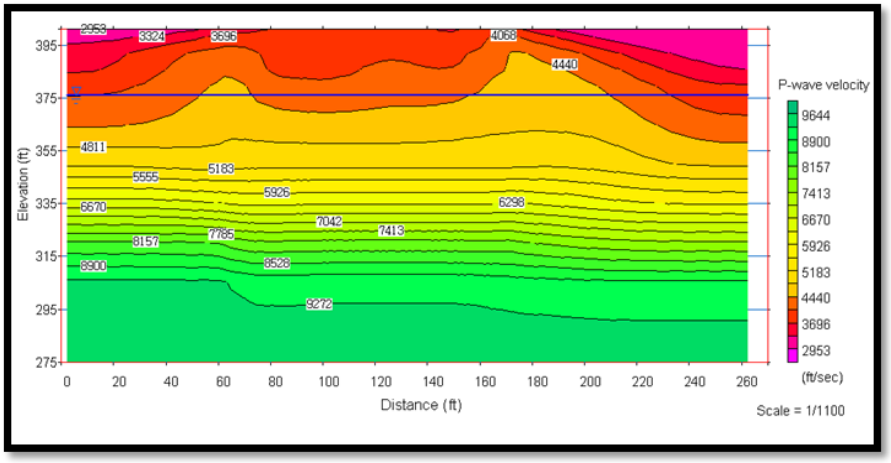

Figure 5.18. Pseudo 2-D P-wave velocity model profile resulting from SRT inversion.

5.3.4. MASW Survey. Multichannel analysis of surface wave data acquisition and processing in this study were performed.

5.3.4.1 MASW data acquisition. The MASW data acquisitions in this study were performed using 24 channels seismic equipment Seistronix RAS - 24, and 4.5 Hz geophones. The sampling interval used is 0.5 ms and recording time is 1,000 millisecond. One survey line is used as shown in Figure 5.19.

Twenty Four geophones are coupled firmly into the ground at 100 ft away of the ILC-11 borehole with spacing of 5 ft; hence the total length of survey line is 115 ft. The sources outside the array line at offset distances 60 ft, 35 ft, and 10 ft (3 records at each source).

The inline sources starting from the first geophone which increased by 10 ft up to the last geophone with 3 records at each source, the total records in this line was 45 records. 20 lb sledge hammer was used as the signal sources for data acquisition and the impact steel plate with dimensions of 1ft x 1ft as a choice to deliver appropriate impact power into the ground, and field laptop.

5.3.4.2 MASW data processing. Processing data of the all records was performed using the SurfSeis software package, developed by the Kansas Geologic Survey (KGS).

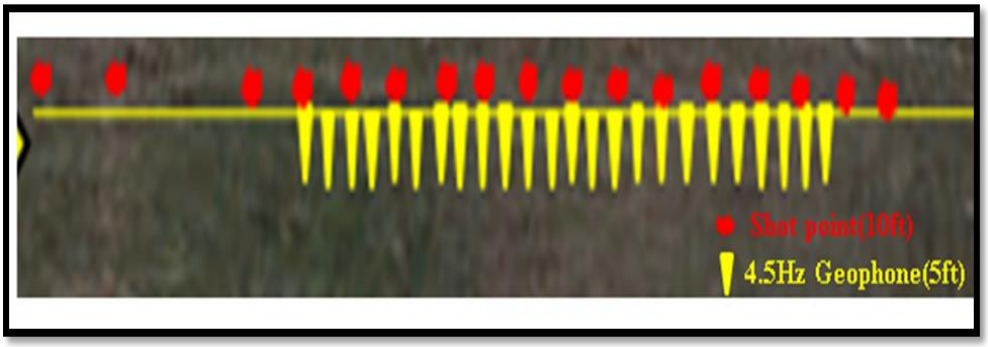

Figure 5.19. MASW data acquired with a fixed spreads and sources at various locations.

Using different spread sizes and different offset distances can help to initiate the 1-D shear wave velocity profiles along the fixed array line as shown from Figure 5.20 to Figure 5.45. The minimum and maximum offset of the array line is more important than the number of used geophones [56]. Various processing parameters; frequency ranges, and phase velocities were used to generate dispersion curves and 1-D shear wave velocity profiles for all of the records.

Field Setup Table: C:\Users\fmm95b\Desktop\11geophoneReverse\Line1(CUT)31.DAT <Channel
(X) = Source Location

RCD#\STA#	1001	1002	1003	1004	1005	1006	1007	1008	1009	1010	1011	1012	1013	1014	1015
31		1	2	3	4	5	6	7	8	9	10	11			(X)

Figure 5.20. Receiver locations for the mid-station 6 (at geophone 6).

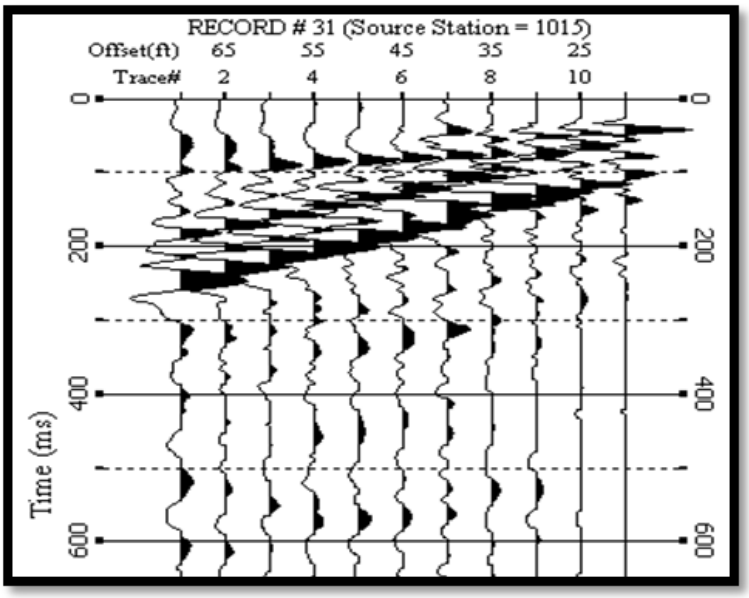

Figure 5.21. Shot gather used for the mid-station 6.

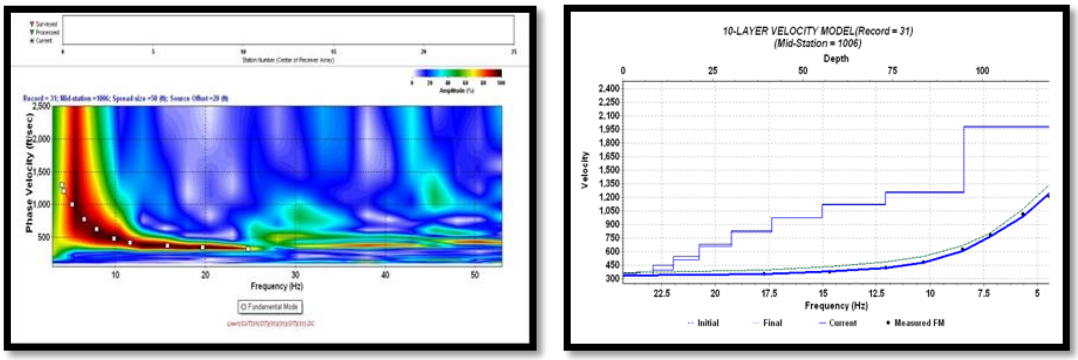

Figure 5.22. Step processing scheme for MASW data for the mid-station 1006.

Field Setup Table: C:\24&13geopones\Line1-45(CUT)13geoR7.DAT <Channel #'s at Each Receive
(X) = Source Location

RCD#\STA#	999	1000	1001	1002	1003	1004	1005	1006	1007	1008	1009	1010	1011	1012	1013
7	(X)		1	2	3	4	5	6	7	8	9	10	11	12	13

Figure 5.23. Receiver locations for the mid-station 7 (at geophone 7).

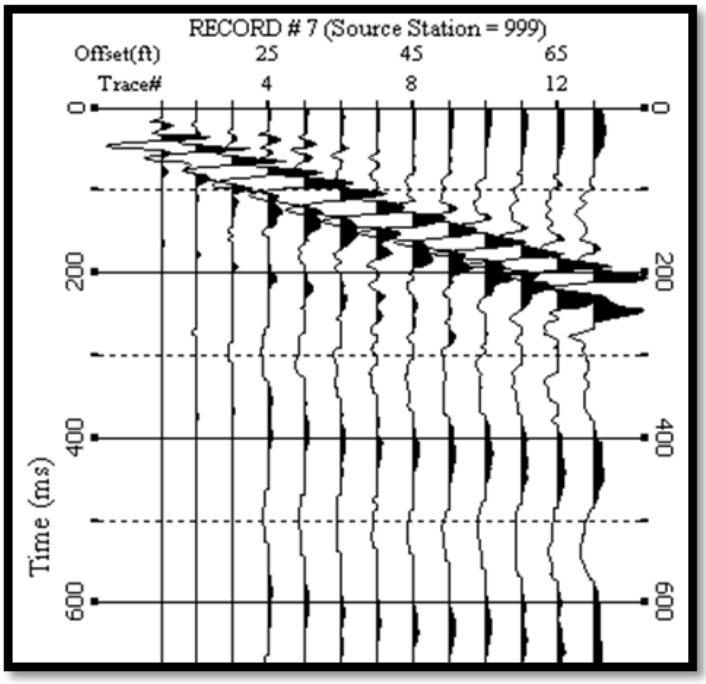

Figure 5.24. Shot gather used for the mid-station 7.

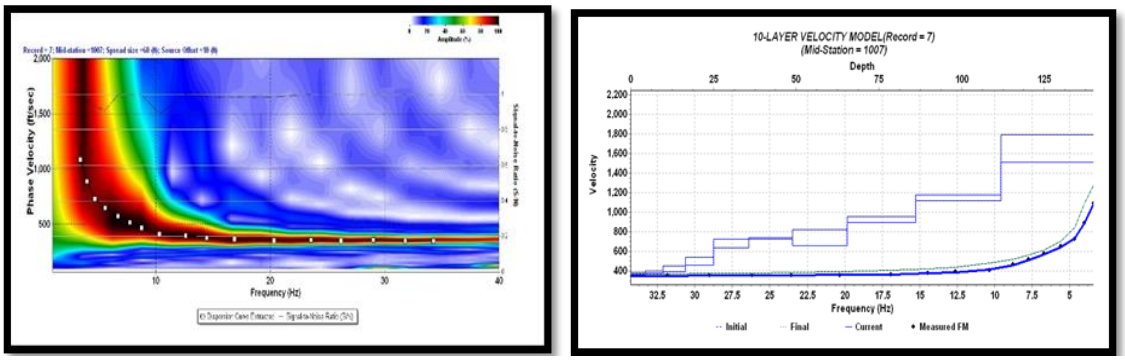

Figure 5.25. Step processing scheme for MASW data for the mid-station 1007.

Field Setup Table: C:\24&13geopones\Line1(CUT)24geoph.DAT <Channel #'s at Each Receiver Location>
(X) = Source Location

RCD#\STA#	994	995	996	997	998	999	1000	1001	1002	1003	1004	1005	1006	1007	1008	1009	1010	1011	1012	1013	1014	1015	1016	1017	1018	1019	1020	1021	1022	1023	1024
4		(X)						1	2	3	4	5	6	7	8	9	10	11	12	13	14	15	16	17	18	19	20	21	22	23	24

Figure 5.26. Receiver locations for the mid-station 12 (at geophone 12).

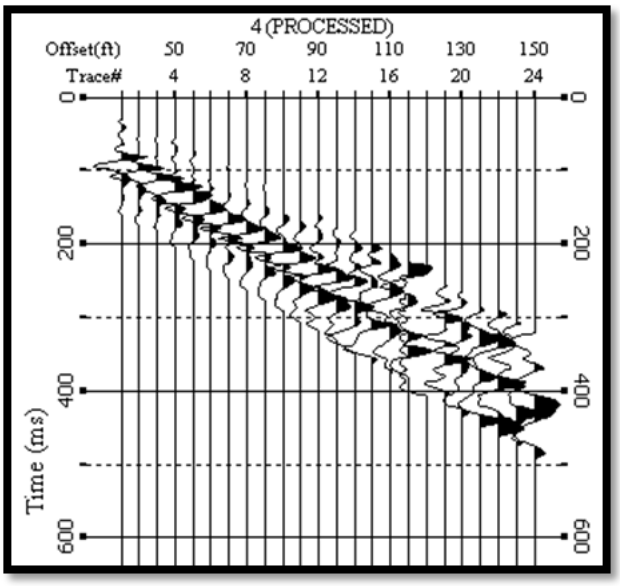

Figure 5.27. Shot gather used for the mid-station 12.

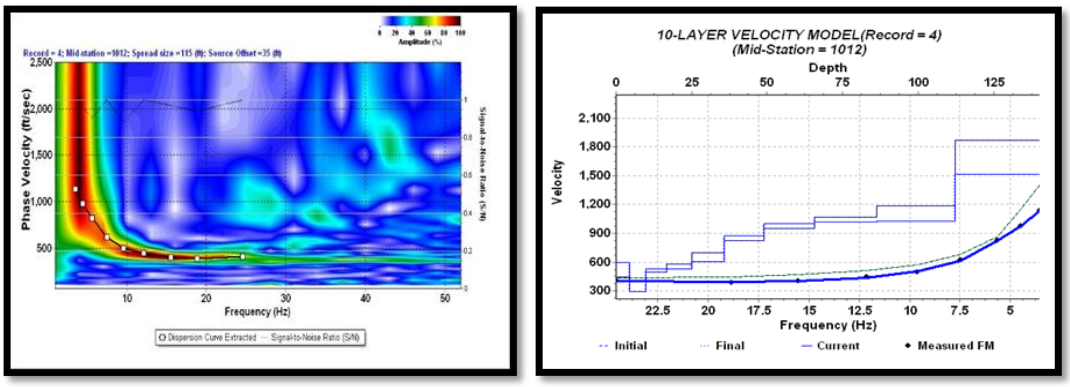

Figure 5.28. Step processing scheme for MASW data for the mid-station 1012.

1001	1002	1003	1004	1005	1006	1007	1008	1009	1010	1011	1012	1013	1014	1015	1016	1017	1018	1019	1020	1021	1022	1023	1024
1	2	3	4	5	6	7	8	9	10	11	12	13	14	15	16	17	18	19	20	21	22	23	24
(X)		3	4	5	6	7	8	9	10	11	12	13	14	15	16	17	18	19	20	21	22	23	24
		(X)		5	6	7	8	9	10	11	12	13	14	15	16	17	18	19	20	21	22	23	24
				(X)		7	8	9	10	11	12	13	14	15	16	17	18	19	20	21	22	23	24
						(X)		9	10	11	12	13	14	15	16	17	18	19	20	21	22	23	24
								(X)		11	12	13	14	15	16	17	18	19	20	21	22	23	24
										(X)		13	14	15	16	17	18	19	20	21	22	23	24

Figure 5.29. Receiver locations for the mid-stations from 13 to 17.

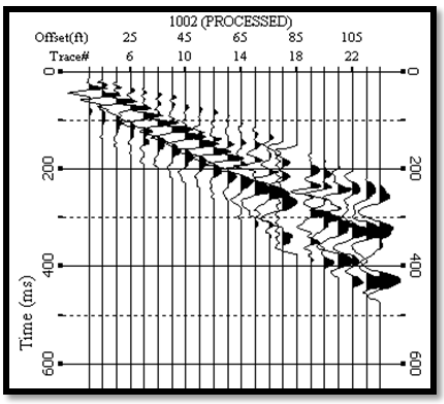

Figure 5.30. Shot gather used for the mid-station 13.

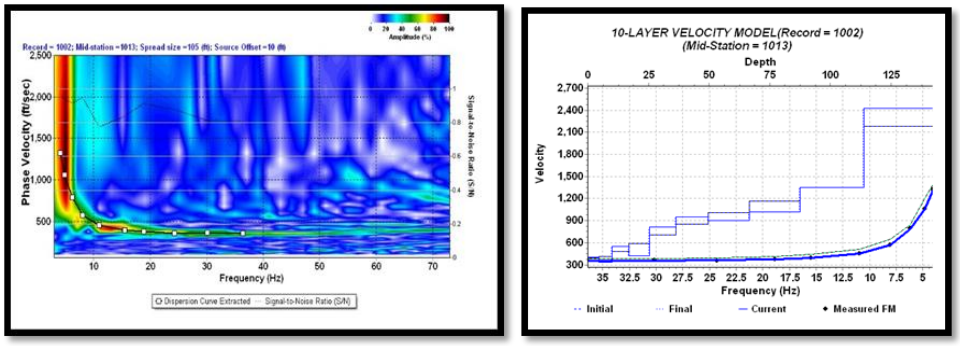

Figure 5.31. Step processing scheme for MASW data for the mid-station 1013.

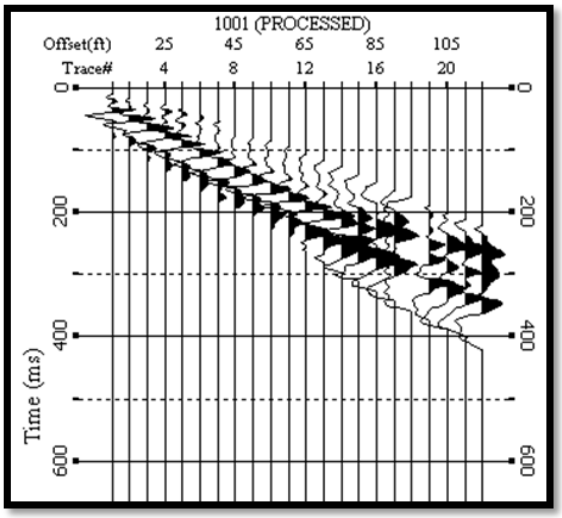

Figure 5.32. Shot gather used for the mid-station 14.

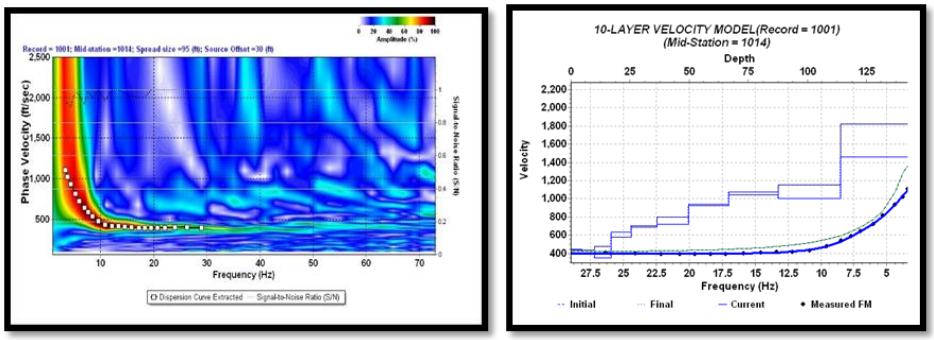

Figure 5.33. Step processing scheme for MASW data for the mid-station 1014.

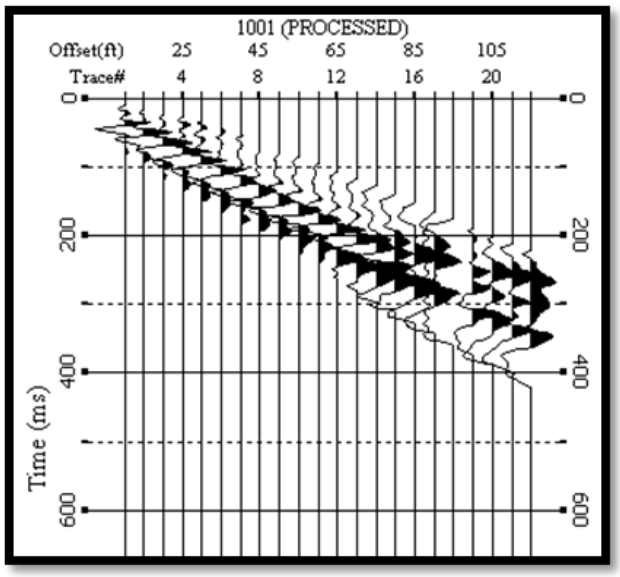

Figure 5.34. Shot gather used for the mid-station 15.

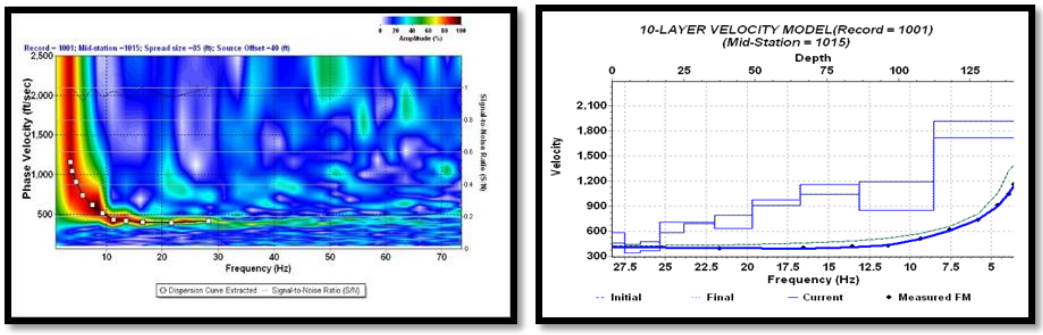

Figure 5.35. Step processing scheme for MASW data for the mid-station 1015.

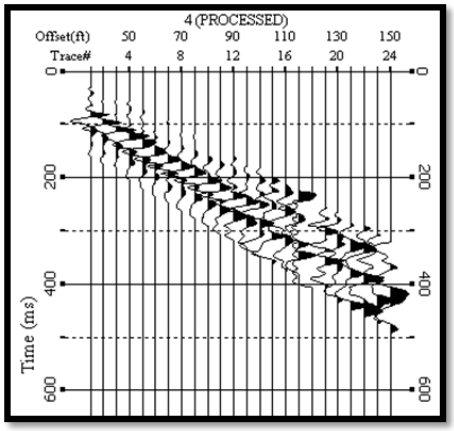

Figure 5.36. Shot gather used for the mid-station 16.

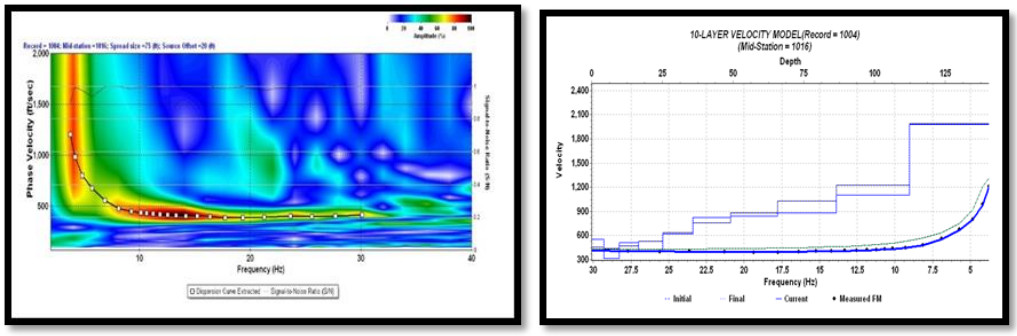

Figure 5.37. Step processing scheme for MASW data for the mid-station 1016.

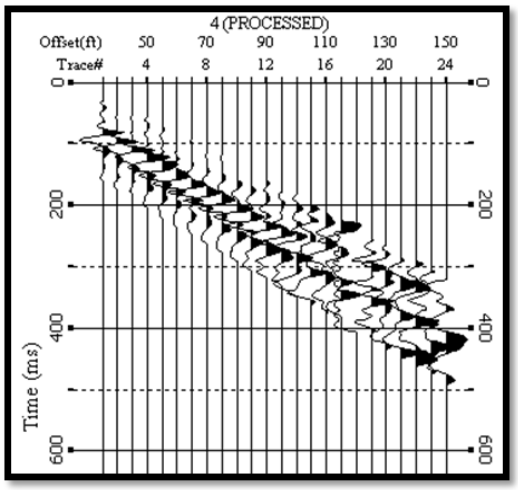

Figure 5.38. Shot gather used for the mid-station 17.

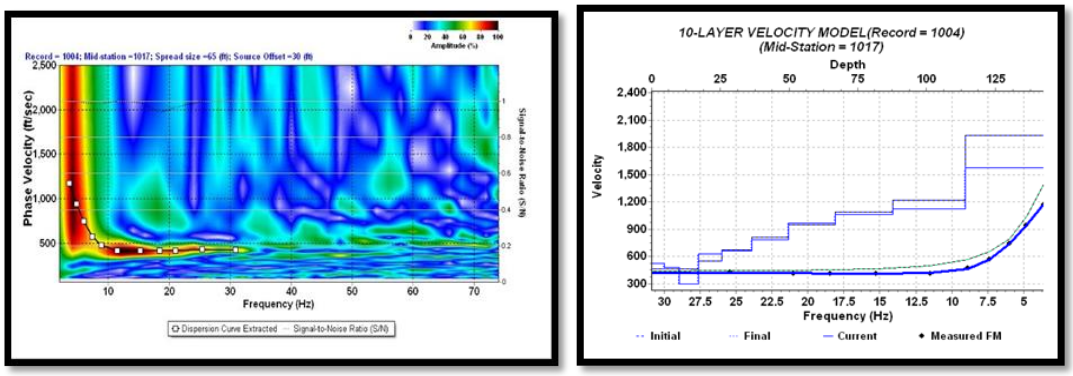

Figure 5.39. Step processing scheme for MASW data for the mid-station 1017.

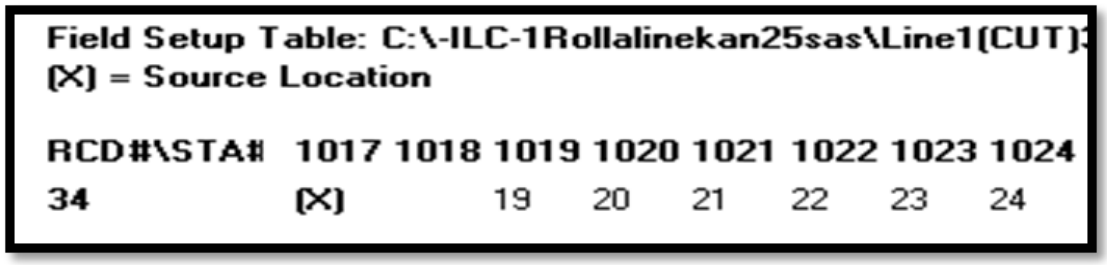

Figure 5.40. Receiver locations for the mid-station 21.

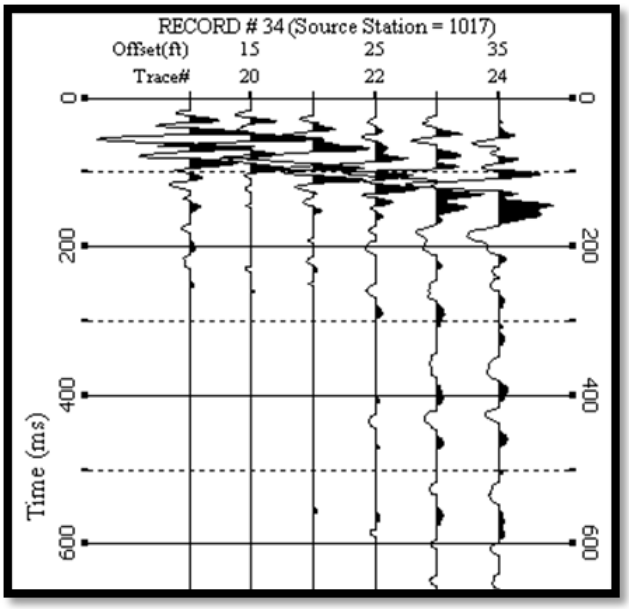

Figure 5.41. Shot gather used for the mid-station 21.

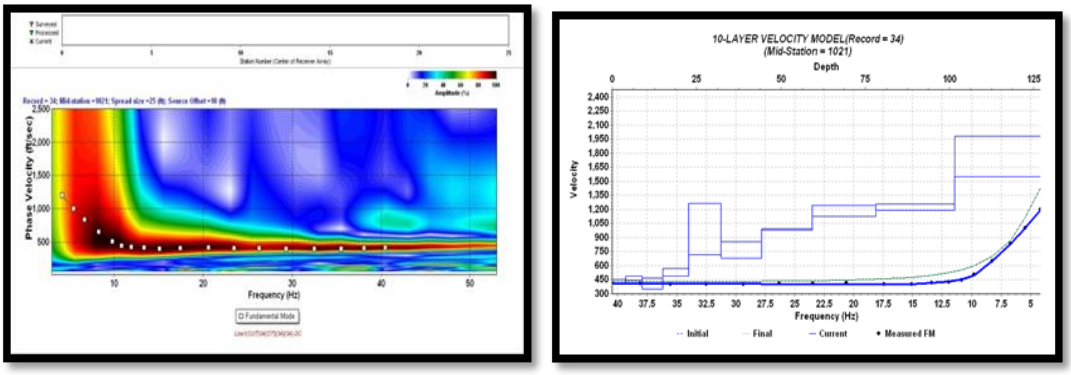

Figure 5.42. Step processing scheme for MASW data for the mid-station 1021.

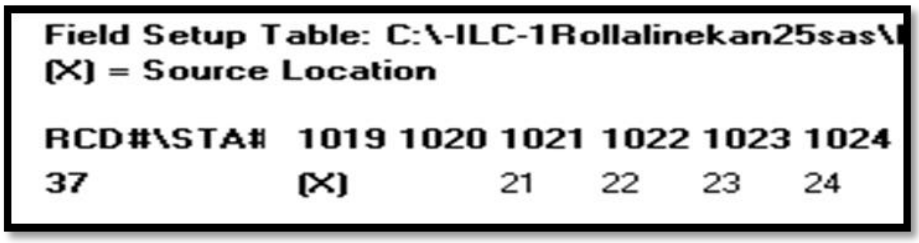

Figure 5.43. Receiver locations for the mid-station 22.

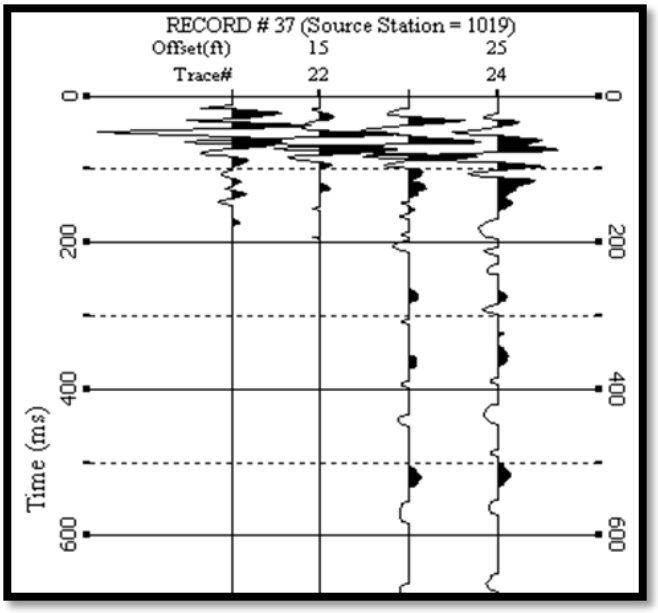

Figure 5.44. Shot gather used for the mid-station 22.

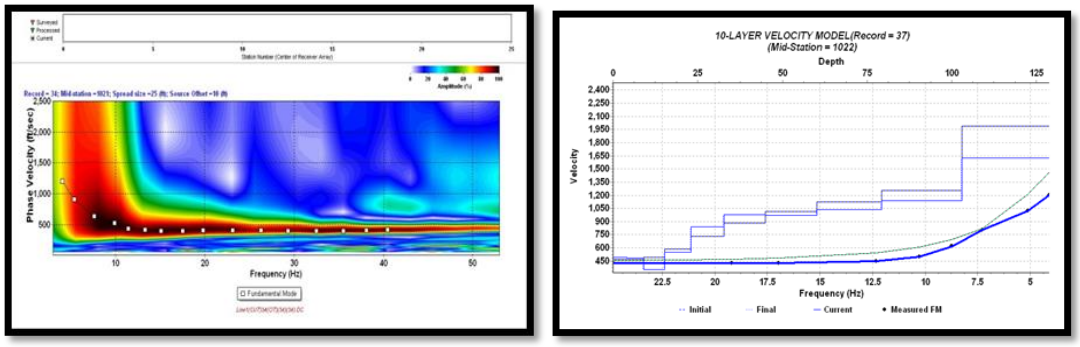

Figure 5.45. Step processing scheme for MASW data for the mid-station 1022.

For the equal weight, the RMS error (Figure 5.46) at the each iteration observed during inversion is calculated by the following

$$Erms = [\sum (o^k - T^k)^2 / M]^{0.5} \quad (5.1)$$

where:

O is the observed phase velocities, and

T is the calculated phase velocities.

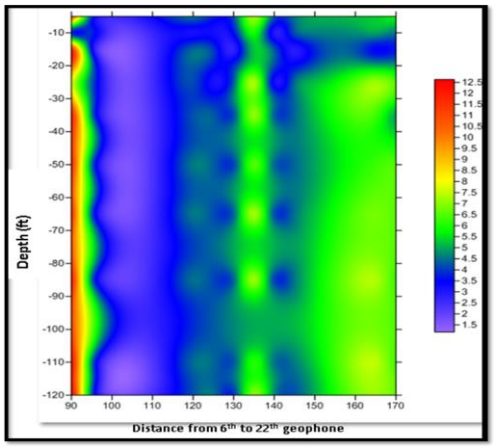

Figure 5.46. RMS error map for the MASW stations.

For the weighted case, the RMS error is calculated by the following:

$$Erms = [\sum (o^k - T^k)^2 / tr(w)]^{0.5} \quad (5.2)$$

where:

Wk is the weight of the kth data, and

tr (w) is the sum of the weights.

5.4. RESULTS AND INTERPRETATIONS

Depth to bedrock, elastic modulus of elasticity , density and Average Shear Wave Velocity at 100 ft (Vs100) were calculated as follows:

5.4.1. Depth to Bedrock. Several geophysical methods can be applied to locate and map the depth to bedrock at a site. The results of depth to bedrock in this study are shown in Table 5.4.

5.4.1.1 Depth to bedrock using borehole data. The soil description of ILC-11 borehole Figure 5.47 shows the depth to the bedrock at 110 ft.

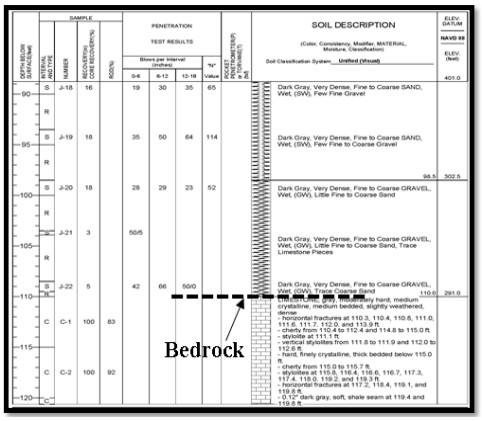

Figure 5.47. Borehole data showing the depth to bedrock.

5.4.1.2 Depth to bedrock using DHS data. The DHS results of the ILC-11 borehole Figure 5.48 shows the depth to the bedrock at 110 ft.

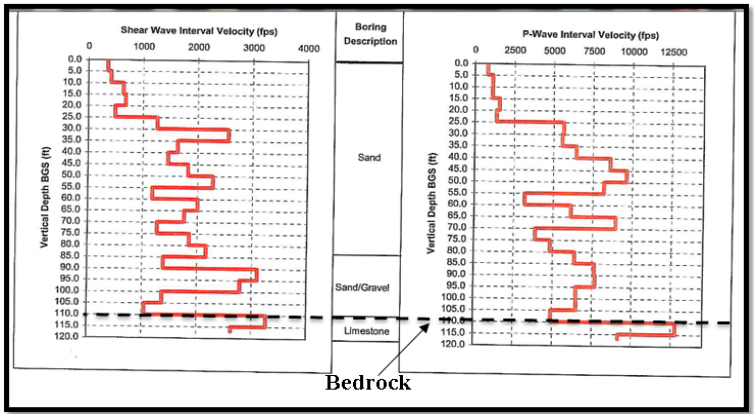

Figure 5.48. S-wave and P-wave velocity model showing the depth to bedrock using DHS.

5.4.1.3 Depth to bedrock using MASW data. Surface seismic wave profile reached depths to 120 ft as shown in Figure 5.49; it shows the bedrock aligned in the southwest to northeast ranged from 100 to 110 ft. which is conformable to the borehole data results.

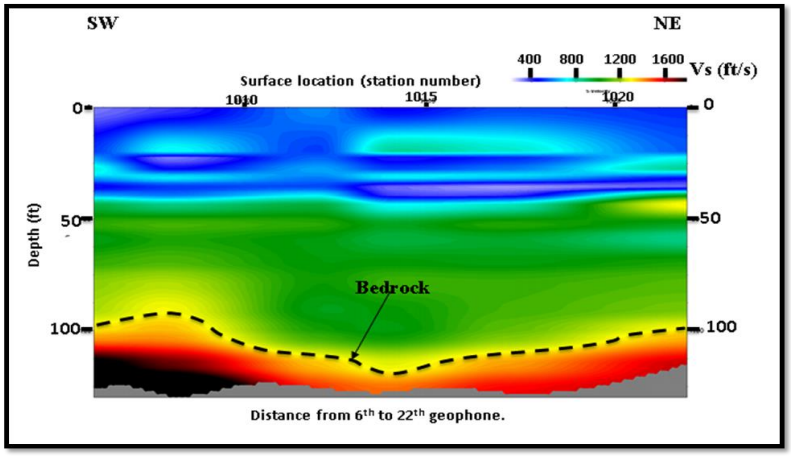

Figure 5.49. S-wave velocity model profile showing the depth to bedrock using MASW.

5.4.1.4 Depth to bedrock using SRT data. The compressional wave profile as shown in Figure 5.50, reached depths up to 120 ft.; it shows the bedrock aligned in the southwest to northeast ranged from 100 to 105 ft. which is conformable to the MASW and borehole data results.

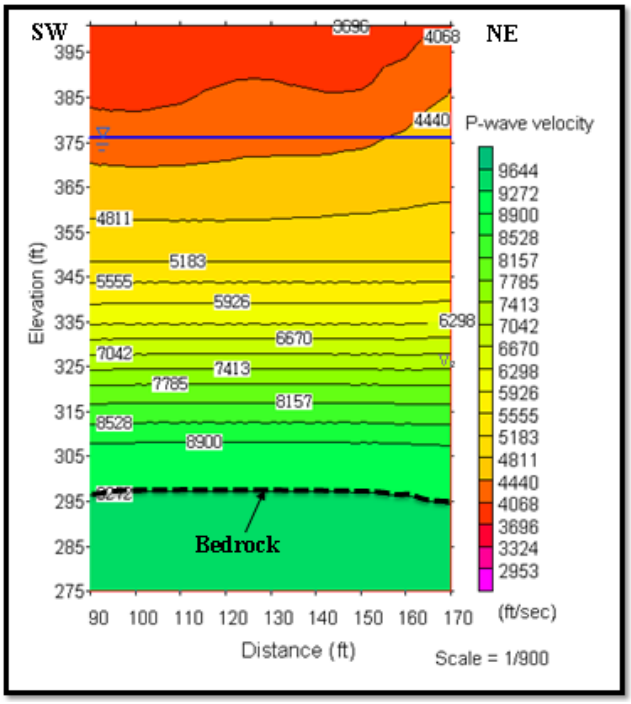

Figure 5.50. P-wave velocity model profile showing the depth to bedrock using SRT.

Table 5.4. Results of depth to bedrock for all methods used in the study site.

Method	Depth to bedrock (ft)
Borehole	110ft
Downhole seismic	110ft
SRT	105ft
MASW	100-110ft

5.4.2. Elastic Moduli Calculation. Measuring p- and s-wave velocities can enable the determination of elastic moduli indirectly and nondestructively; these include the shear modulus, young's modulus, and the bulk modulus.

5.4.2.1 Shear modulus calculation. The shear modulus can be calculated using density and shear velocity as shown in the following equation:

$$G = \rho V_S^2 \quad (5.3)$$

where,

G is the shear moduli

V_S is Shear-wave (S-wave) velocity

ρ is Density.

The shear modulus was calculated and mapped as 2D and 3D for all the stations as shown in Figure 5.51 and Figure 5.52.

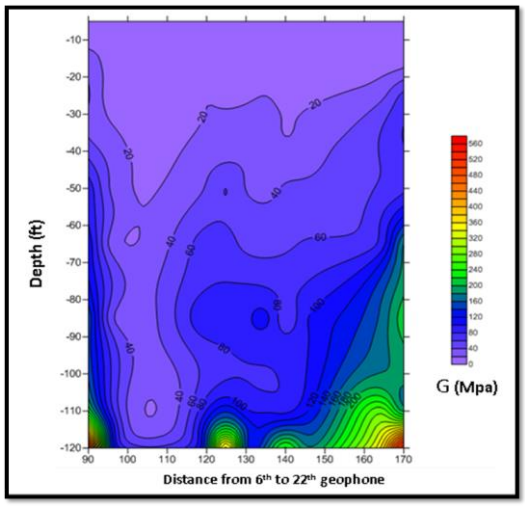

Figure 5.51. 2D map of the shear modulus of the subsurface.

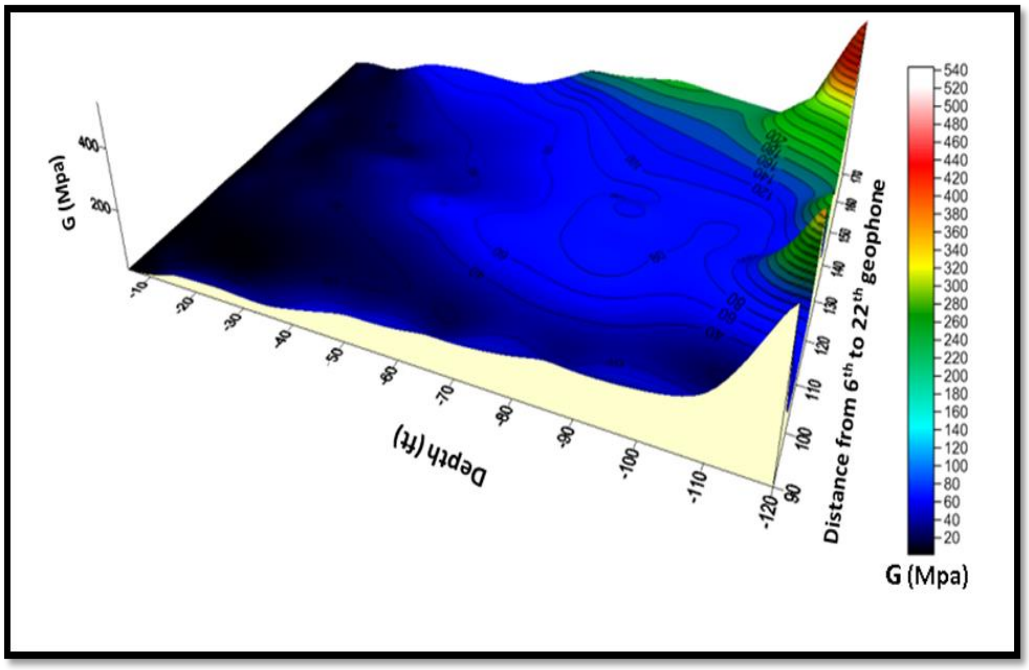

Figure 5.52. 3D map of the shear modulus of the subsurface.

5.4.2.2 Young's modulus calculation. The Young's modulus can be calculated using Poisson's ratio and shear modulus as shown in the following equation:

$$E = 2G\,(1+\nu) \tag{5.4}$$

where:

E= Young's modulus,

G = the shear modulus, and

ν = Poisson's ratio.

The Young's modulus was calculated and mapped as 2D and 3D for all the stations as shown in Figure 5.53 and Figure 5.54.

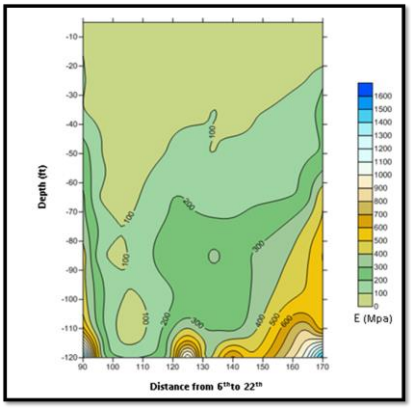

Figure 5.53. 2D map of the Young's modulus of the subsurface.

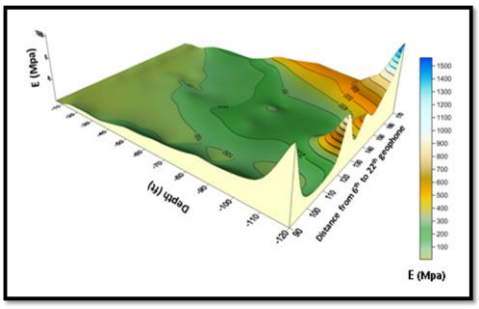

Figure 5.54. 3D map of the Young's modulus of the subsurface.

5.4.2.3 Bulk modulus calculation. The bulk modulus can be calculated using shear modulus and Young's modulus as shown in the following equation:

$$K = (9G - 3E) / EG \tag{5.5}$$

where:

K is the bulk modulus,

E is the Young's modulus, and

G is the shear modulus.

The bulk modulus was calculated and mapped as 2D and 3D for all the stations as shown in Figure 5.55.

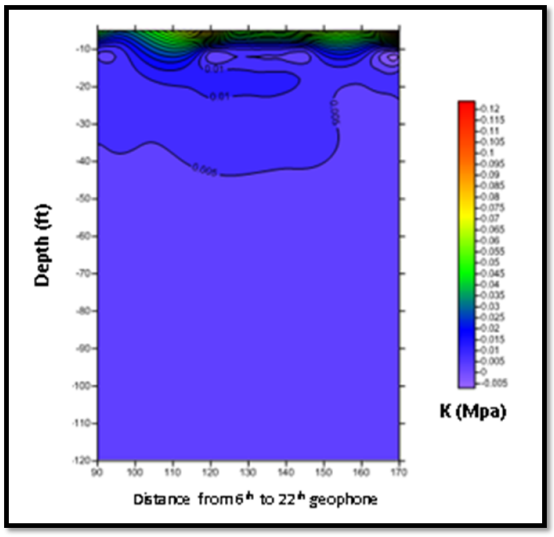

Figure 5.55. 2D map of the bulk modulus of the substance.

5.4.3. Poisson's Ratio Calculation. According to Simeon Poisson (1781 to 1840), a French mathematician, Poisson's ratio (ν) can be expressed in terms of properties which can be measured in the field, including velocities of P-waves (V_P) and S-waves (V_S) and no need to know the density of material as shown:

$$\nu = \tfrac{1}{2} [(V_P)^2 - 2 (V_S)^2] / [(V_P)^2 - (V_S)^2] \quad (5.6)$$

Poisson's ratio was calculated using inversions control of MASW processing as shown in Figure 5.56 by importing V_p values results from SRT method and V_s from MASW at all the stations and then compared with Poisson's ratio which, was calculated from DHS.

The result of Poisson's ratio comparison are shown in selected stations 22 & 16 (Figure 5.57) and (Figure 5.58) respectively. Both of the curves have very good agreement.

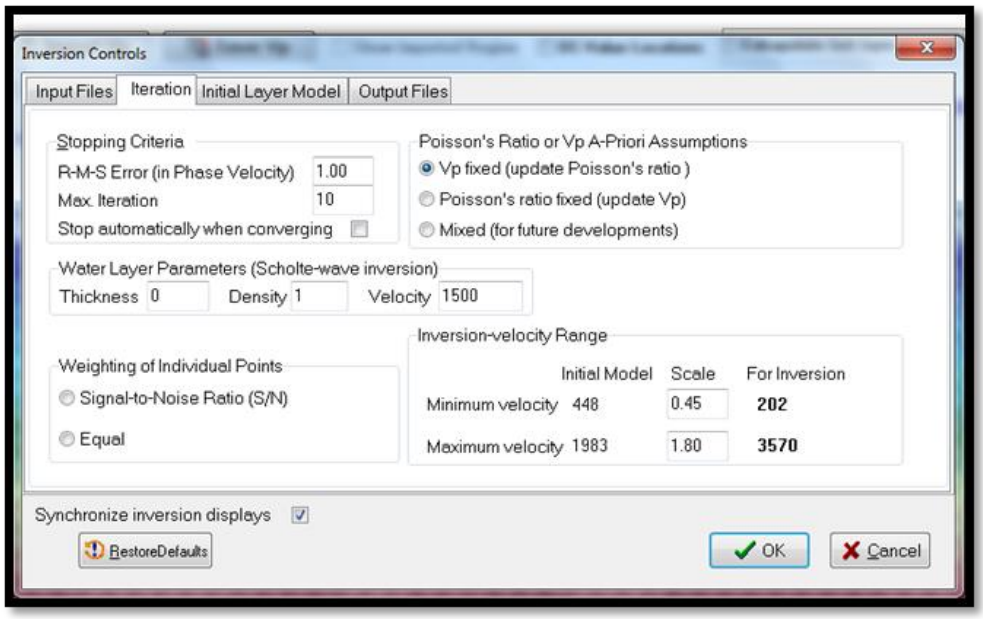

Figure 5.56. Poisson's ratio using MASW inversion by V_p values of SRT.

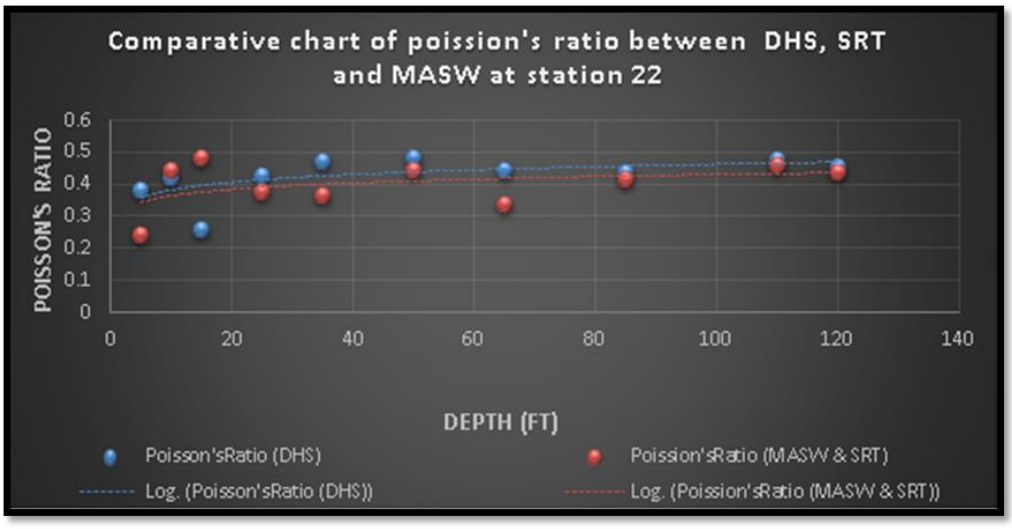

Figure 5.57. Poisson's ratio calculated at station 22.

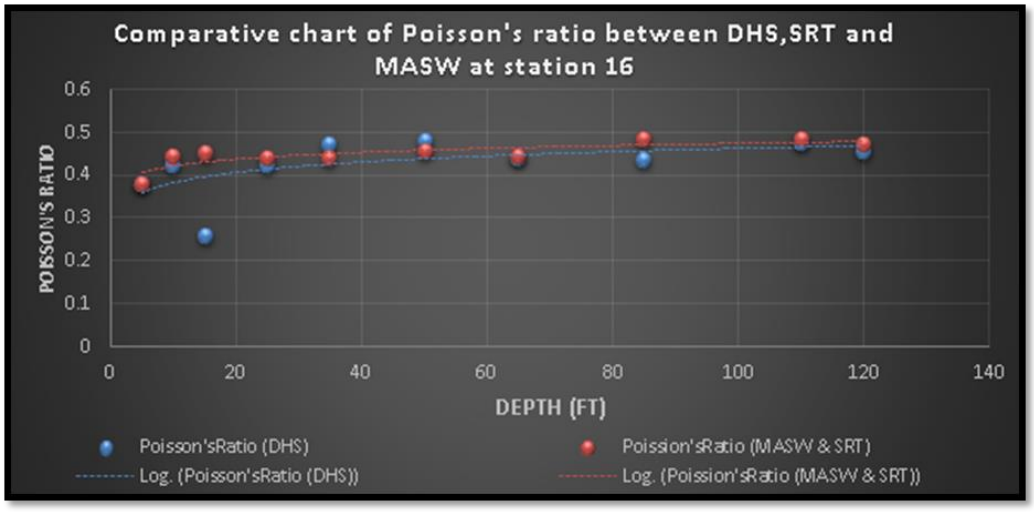

Figure 5.58. Poisson's ratio calculated at station 16.

The Poisson's ratio was calculated and mapped as 2D and 3D for all the stations as shown in Figure 5.59 and Figure 5.60.

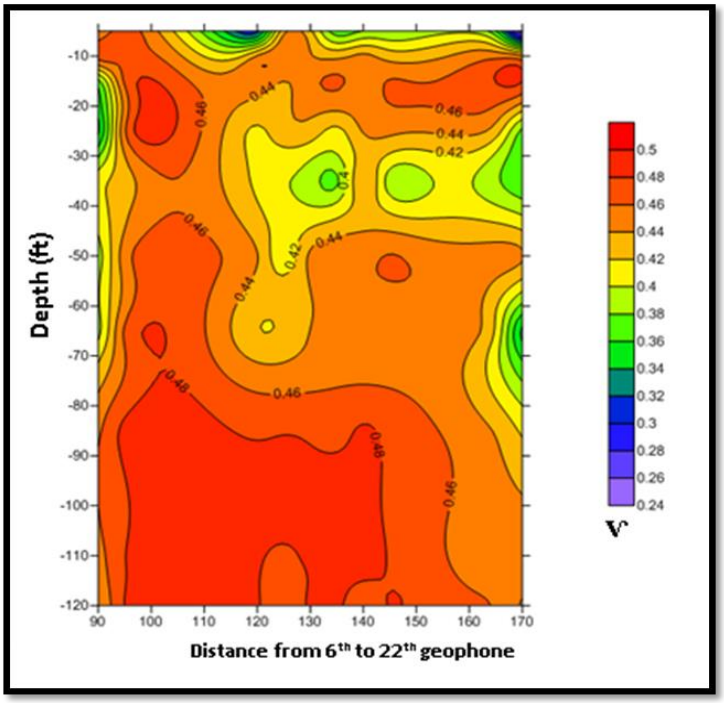

Figure 5.59. 2D map of the Poisson's ratio of the subsurface.

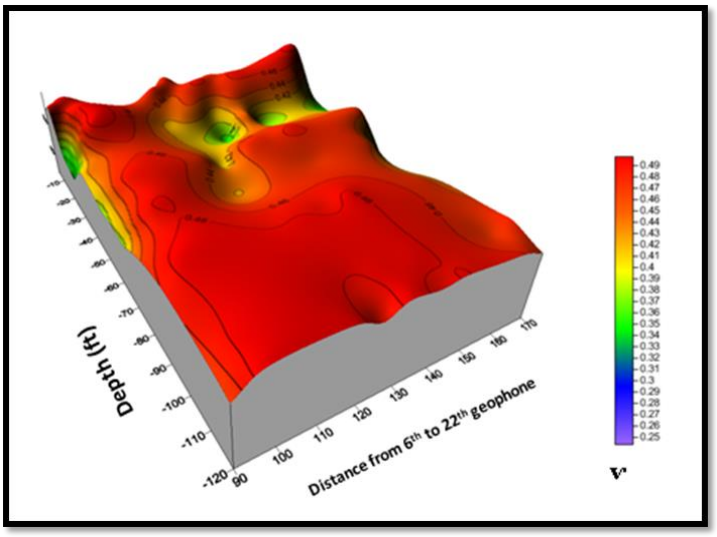

Figure 5.60. 3D map of the Poisson's ratio of the subsurface.

5.4.4. Density Calculation. Density can be calculated using Gardner equation. It is an empirically derived equation that relates seismic P-wave velocity to the bulk density of the lithology in which the wave travels.

$$\rho = \alpha V_p \beta \tag{5.7}$$

where:

ρ is a density,

α and β are empirically derived constants that depend on the geology, and

V_p is P-wave velocity (ft/s).

α and β are equal 0.23 and 0.25 respectively, the equation becomes:

$$\rho = 0.23 V_p 0.25 \tag{5.8}$$

The density was calculated and mapped as 2D and 3D for all the stations as shown in Figure 5.61 and Figure 5.62.

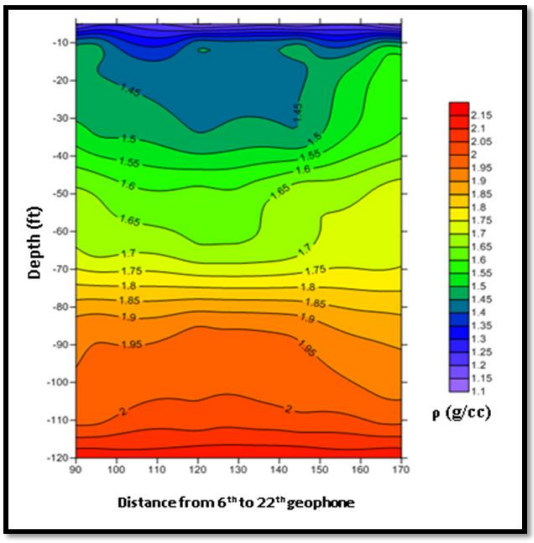

Figure 5.61. 2D map of the density of the subsurface.

5.4.5. Average Shear Wave Velocity (Vs100) Calculation. Calculating of the seismic hazard is usually carried out according to the near-surface shear wave velocity values. The averaged shear wave velocity for the depth ‘‘d’’ of the soil is referred as VH.

The average shear waves velocity down to a depth of H. (VH) is computed as follows:

$$VH = \sum di / \sum (di/vi) \quad (5.9)$$

where:

$\sum di$ is the cumulative depth in ft, and

Vi is the shear wave velocity.

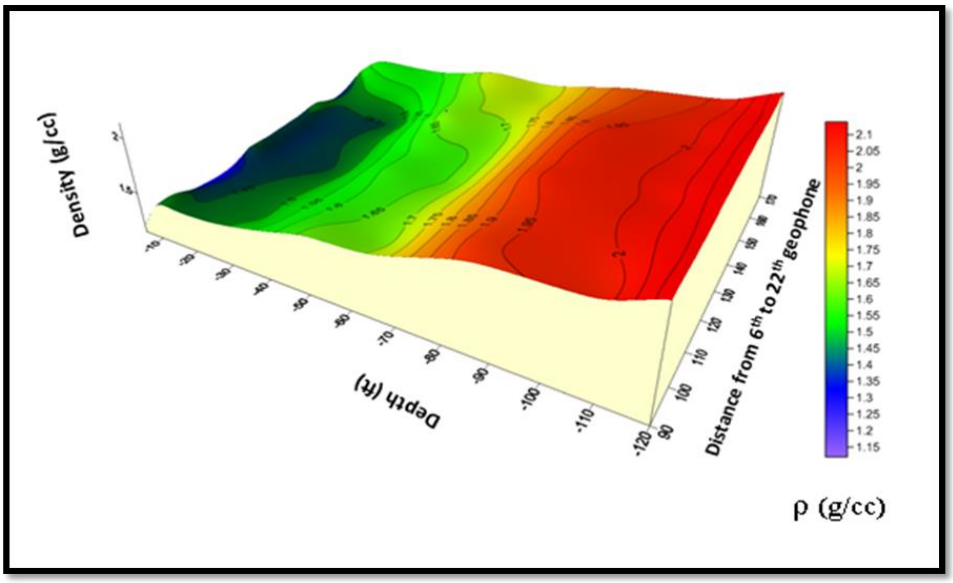

Figure 5.62. 3D map of the density of the subsurface.

For the average depth reached to 100ft, the shear wave velocity is written as:

$$Vs100 = 100/\sum di = (di/vi) \tag{5.10}$$

where:

di is denote the thickness (ft.),

vi is the layer velocity, and

Vs100 is the shear wave velocity at 100 ft in ft/s.

Site can be classified based on shear velocity of the top 100 ft. of the soil profile (Vs100) into known six categories (Soil types A through F) presented in Table 5.4.

The Table 5.5 is the soil profile type classification according to the national earthquake hazards reduction program (NEHRP).

Table 5.5. Soil profile type classification [57].

Soil type NEHRP	General description	Average shear wave velocity to 100 ft (ft/s)
A	Hard rock	> 4800
B	Rock	2430 < Vs ≤ 4800
C	Very dense soil and soft rock	1150 < Vs ≤ 2430
D	Stiff soil	576≤ Vs≤ 1150
E	Soil or any profile with more than 10 ft of soft clay defiled as soil	≤ 576

Table 5.6 shows the average shear wave velocity for the top 100 ft of soil (Vs100) in the study area range from 625 to 915 ft⁄s.

Table 5.6. Soil profile type for the study site using MASW and DHS tests.

MASW Stations	Vs100 (ft/s)	Soil Type (NEHRP)
1006	804	D
1007	569	D
1012	678	D
1013	654	D
1014	642	D
1015	670	D
1016	625	D
1017	668	D
1022	915	D
DHS	1026	D

6. ARKANSAS CASE STUDY

6.1. STUDY AREA

Earthquakes occur every year throughout the Mississippi County, state of Arkansas because Arkansas is located near one of the most hazardous earthquake zones in the North America, which is the New Madrid seismic zone (NMSZ). This active earthquake zone extends from Cairo, Illinois, into Marked Tree (Poinsett County).

The study site is located in the eastern part of Arkansas at (35°58'25.47"N, 89°55'31.95"W) in Blytheville, Arkansas on the NMSZ, the width of the ridge is about 416 ft, the geophysical lines (Figure 6.1) were run along, has been extended beyond the ridge in each directions. The new Lidar data show linear highs that appear to be the Cottonwood Grove fault (also sometimes called the Blytheville fault); some preliminary subsurface data were achieved to help suggest that this topographic high is a fault.

Integrated geophysical techniques, ERT, SRT and MASW provided greater details of lateral offset of features across the fault.

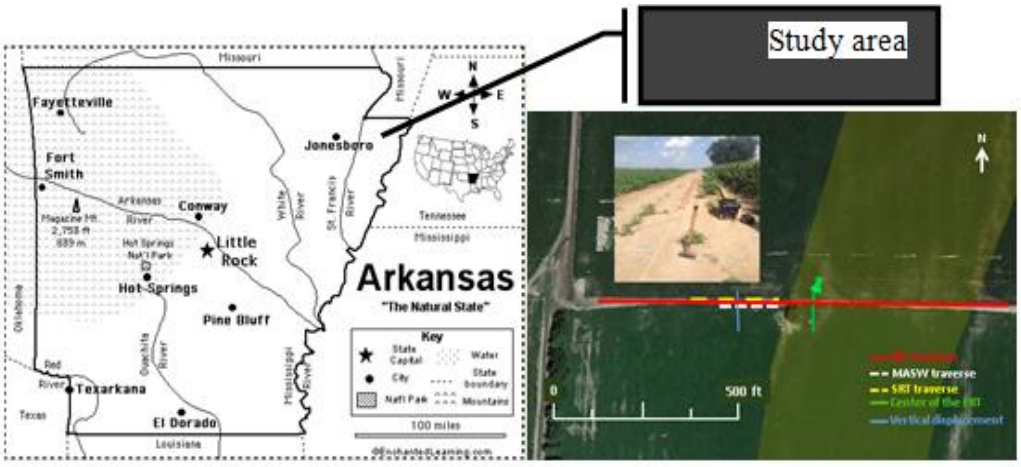

Figure 6.1. Map of study site in Arkansas [58].

6.2. GEOLOGY AND STRATIGRAPHY

Arkansas is divided into a highland area in the northwest and a lowland region in the south and east. The rocks in the highland area are dominated by well-lithified sandstones, shales, limestones, and dolostones of Paleozoic age. A thin drape of younger unconsolidated clays, sands, and gravel, termed alluvium, is often found in valley floors and associated with the streams and rivers. The sedimentary deposits of the lowlands are mainly unconsolidated clay, sand, and gravel of Quaternary age, poorly consolidated deposits of clay, sand, silt, limestone, and lignite of Tertiary age, and consolidated (to a limited extent) deposits of Cretaceous marl, chalk, limestone, sand, and gravel.

In the late Paleozoic Era, a broad uplift domed the Ozark strata with little structural disruption. Figure 6.2 shows the West Gulf Coastal Plain and Mississippi River Alluvial Plain sub regions of the Gulf Coastal Plain of Arkansas Simultaneously, a collision of two of the earth's mobile continental plates compressed the sediments of the abyssal plain into the Ouachita Mountains. This multimillion-year-long process folded and faulted the Ouachita strata into a structurally complex mountain chain.

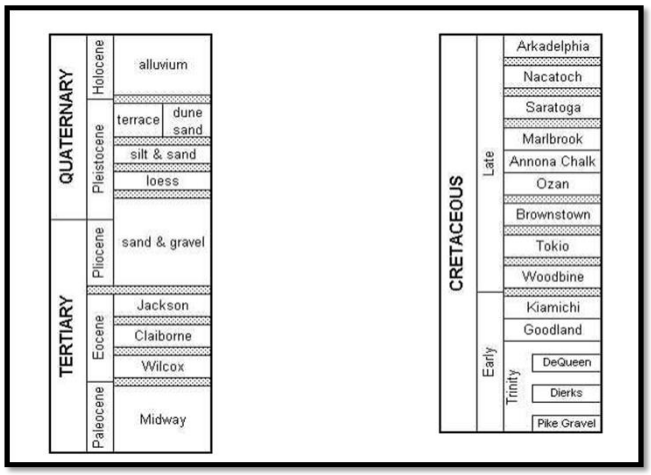

Figure 6.2. Stratigraphic correlation charts for Arkansas [59].

The Arkansas River Valley area is the transition zone between the structurally simple Ozarks and the structurally complex Ouachitas with subdued characteristics in each region. Eastern and southern Arkansas is underlain by Cretaceous age through recent sedimentary deposits with small areas of igneous intrusions of Cretaceous age. Eastern and northeastern Arkansas is dominated by Quaternary terrace and alluvial deposits with minor exposures of Tertiary units.

The central part of the Bootheel lineament (Figure 6.3) has been identified as a Holocene surface fault with both vertical and horizontal motion [59], A–A′ (Figure 6.4) indicates ~10 ft. of vertical offset of the braid-stream sand, but these could be related to either ground failure or uplift. Displacement on the fault is interpreted to be 10 ft in the vertical sense and at least 42 ft. in a right lateral sense.

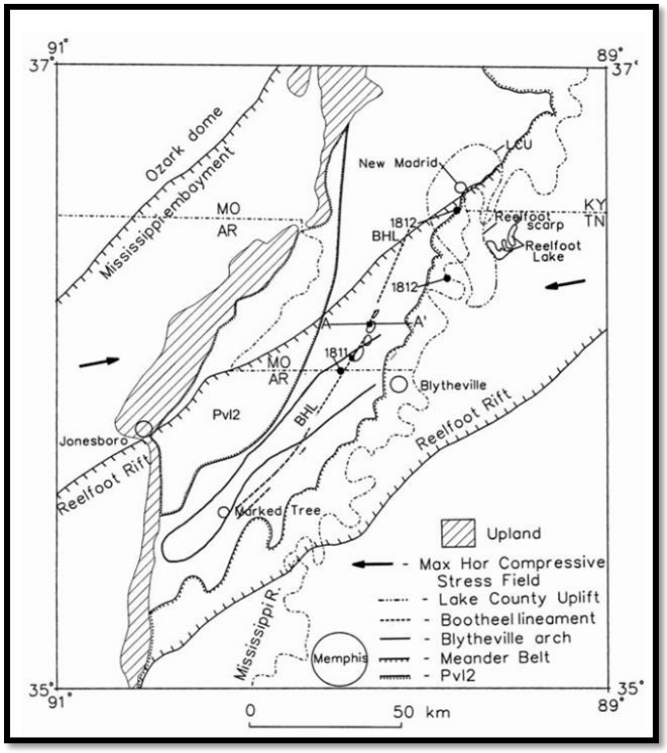

Figure 6.3. Location of Bootheel fault , Blytheville arch in the NMSZ [60].

A compressional pop up between two echelon segments of the BHF that may be associated with the large elliptical sandy area east of the study site may have contributed to the vertical component of displacement observed in the site.

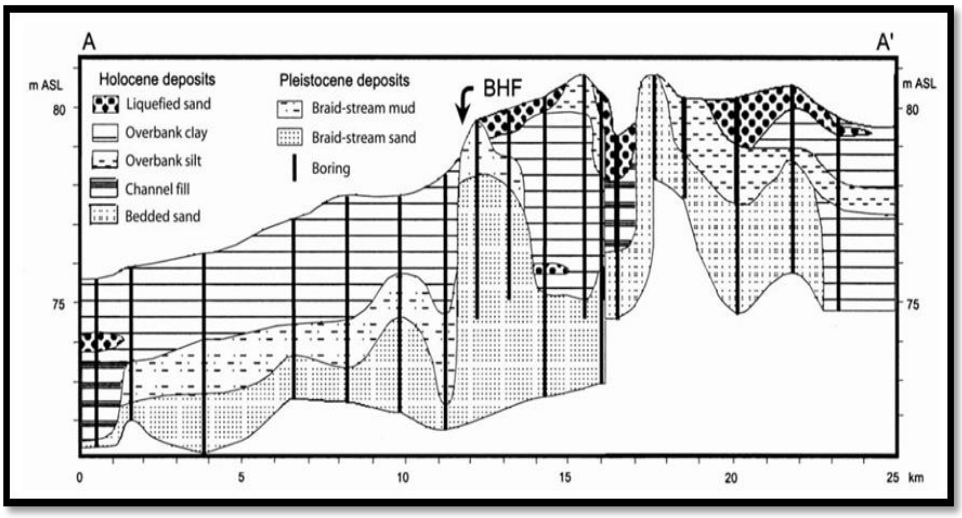

Figure 6.4. Cross section of the western Mississippi River flood plain [61].

The Reelfoot thrust fault is responsible for the most of the modern seismicity of the NMSZ (Figure 6.5). It is interpreted as an inverted basement normal fault. [62]. The Reelfoot Rift is formed during the breakup of the supercontinent Rodinia in the Neoproterozoic Era (about 750 million years ago). The resulting rift system apply as a weak zone deep underground the Earth's crust in the New Madrid seismic zone makes the area weaker than much of the rest of North America . This weakness allows reactivating old faults around New Madrid area, which make it prone to earthquakes. Also, heating in the lithosphere below the area will increase the deep rock plasticity, which makes the compressive stress more concentrate in the shallower subsurface area where the faulting occurs.

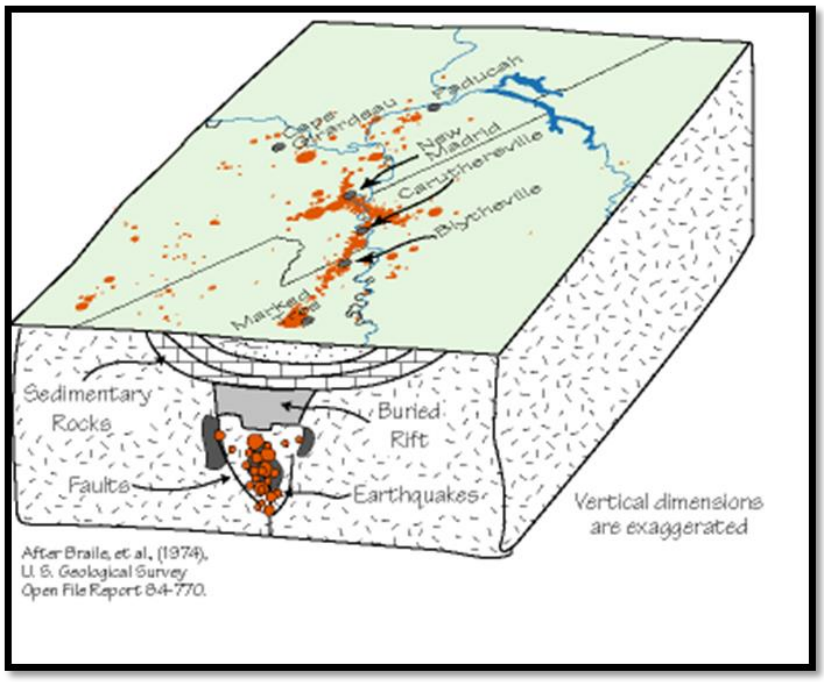

Figure 6.5. New Madrid faults structures [63].

The Reelfoot rift is a north-east-trending, 300km (186.4ml) long, 70m wide graben with a structural relief of ~2 m (6.4 ft.) between the interior of the graben and the surrounding basement [64], [62]. Although there is surface evidence for late Quaternary right-lateral strike-slip movement on the Reelfoot margins, net fault separation in the basement is dip slip [65], [66]. As shown in Figure 6.6, the new Madrid fault has seven segments and their respective lengths, they are: Blytheville arch (BA-71 m), Blytheville fault zone (BFZ-55 m, Botheel lineament (BL-70 m), new Madrid west (NW-40 m), new Madrid north (NN-59.5 m), Reelfoot fault (RF-32.2 m), and Reelfoot south (RS-35.4 m) [64]. There are two types of faults within the fault system, a strike slip segment oriented to the northeast, extending from marked tree to Caruthersville, MO, and a reverse fault trending to the northwest that rests below the new Madrid region [63]. Material on the northwest side of the strike slip fault moves northeast and up the ramp.

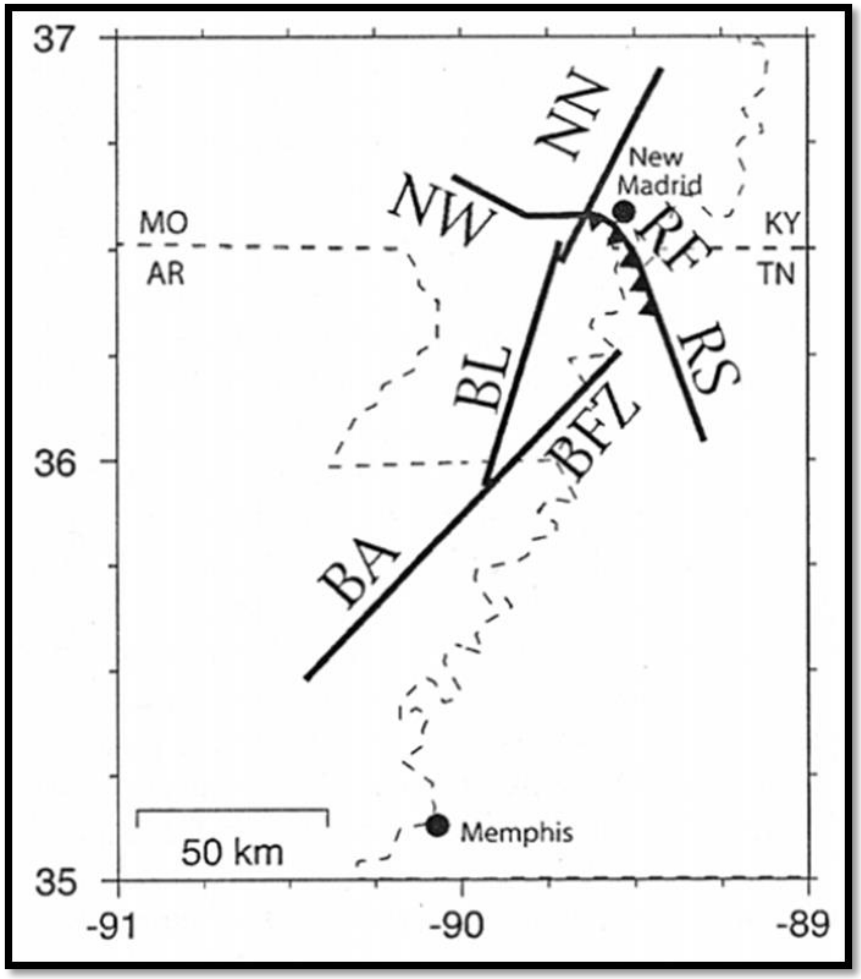

Figure 6.6. Fault segmentation of the NMSZ [64].

The impact of the Reelfoot on Quaternary deformation in the central Mississippi River valley is shown in Figure 6.7; the Reelfoot rift is subdivided into eight fault-bound blocks. The rift consists of two basins divided by a structural high. This high area is bound on the north by the Osceola fault zone and on the south by the Bolivar-Mansfield tectonic zone. Eastern Rift Margin and Western Rift Margin faults have major changes in strike occur near their intersection with the Bolivar-Mansfield tectonic zone and the Osceola fault zone, also indicating that these southeast-trending faults influenced the geometry of the Reelfoot rift.

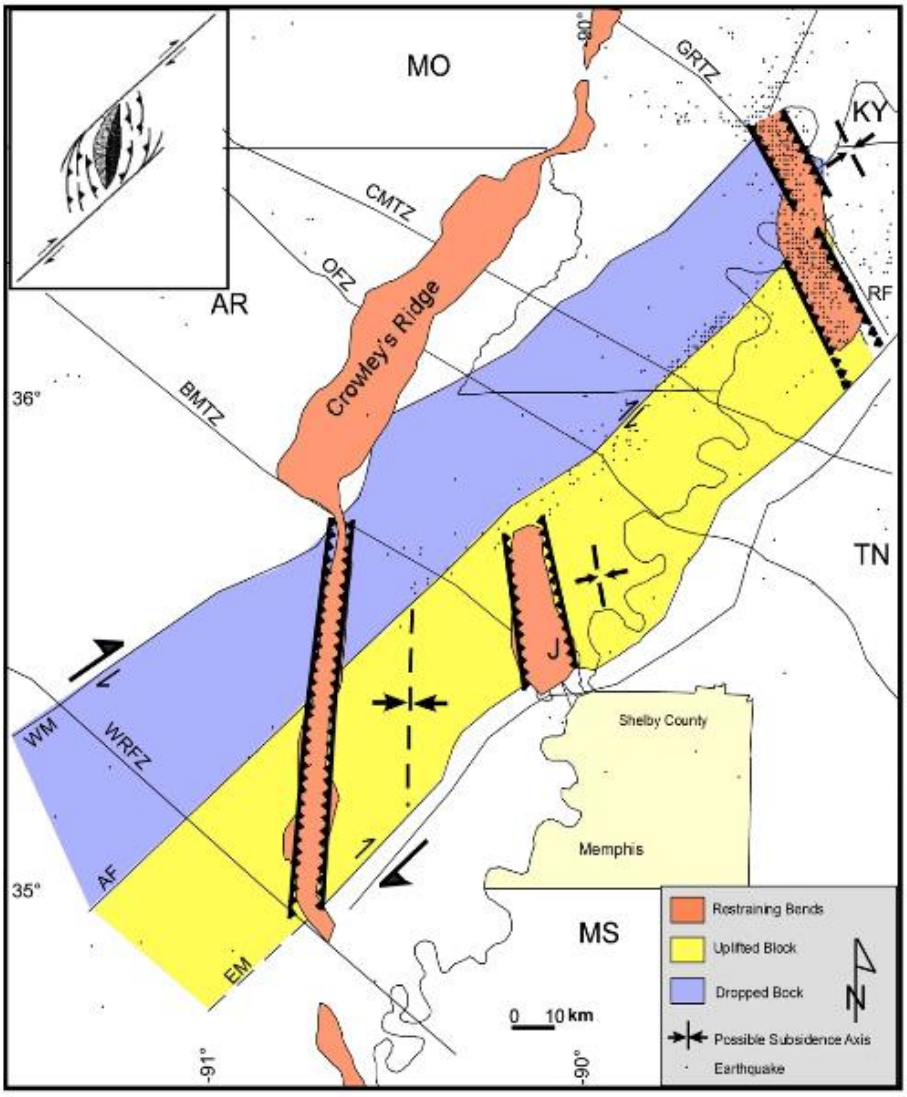

Figure 6.7. Interpreted deformation of the Pliocene–Pleistocene unconformity surface [66].

Figure 6.8 shows the three dimensional model of deep seated faulting in the NMSZ. [67], the segmented faults (BVF, CGF, BF, and PF) join together into a single fault at depth in the lower crust.

These segment faults have a relative movement shows a series of echelon Riedel R shear faults in the brittle upper crust. BVF, Blytheville fault; CGF, Cottonwood Grove fault; BF, Bardwell fault; PF, Paducah fault.

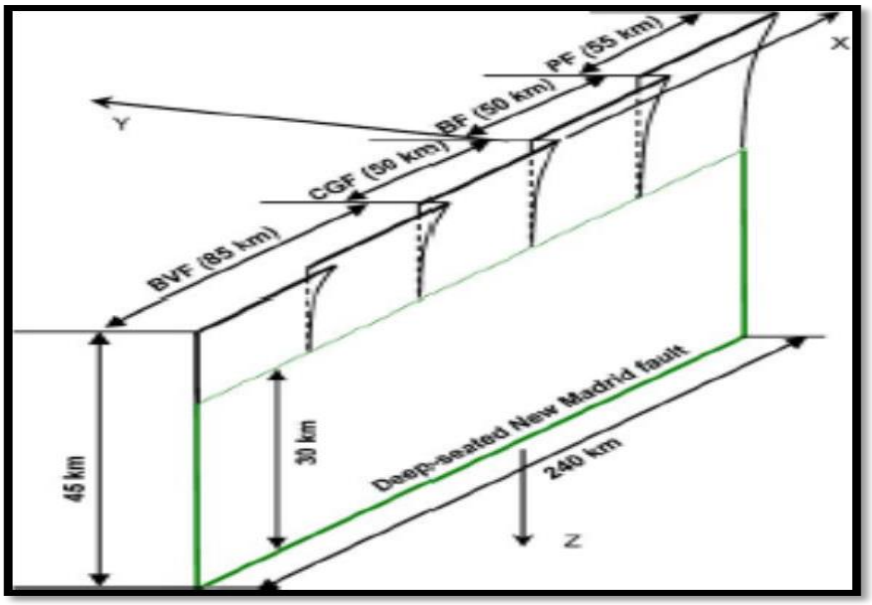

Figure 6.8. Three-dimensional model of deep-seated faulting in the NMSZ [67].

6.3. METHODOLOGY AND DATA

The avaliable borehole data, ERT, MASW and SRT were used in this study.

6.3.1. Borehole Data. The nearest bore hole in the study area in Mississippi County as shown in Figure 6.9, a water will with 100 ft. depth shows the static water level 13 ft. below land surface. The subsurface layers show a flood plain deposits.

6.3.2. SRT Survey. Seismic refraction tomography (SRT) has been used in this study; the data were acquired and processed using SeisImagerTM software.

6.3.2.1 SRT data acquisition. The SRT data acquisition were performed using 24-channels seismic equipment Seistronix RAS - 24, the sampling interval used is 0.25 millisecond and recording time is 0.25 millisecond.

The seismic refraction survey line has been done by 280 ft. as the total length of survey line using 14 HZ Vertical Geophones with 10 ft. geophone spacing. Both of the Offset forward and backward distances were equal 25 ft.

The signal sources for data acquisition achieved by a sledge hammer (20 lb.) and the impact steel plate with dimensions of 1ft x 1 ft.

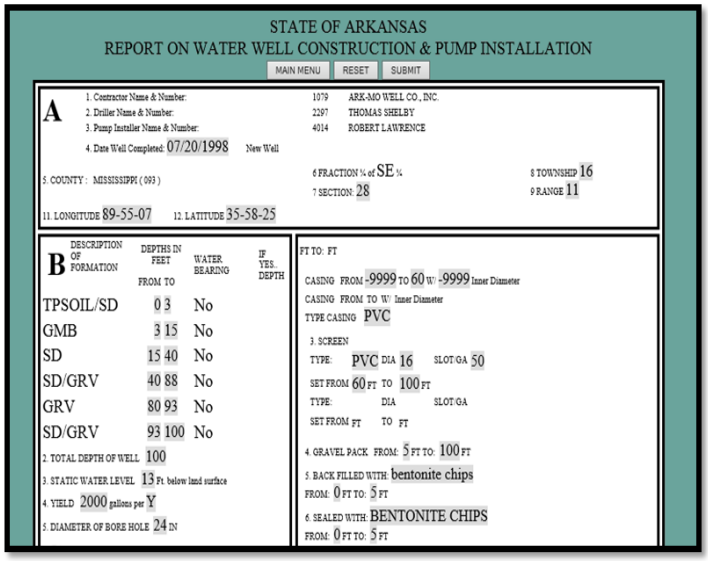

STATE OF ARKANSAS
REPORT ON WATER WELL CONSTRUCTION & PUMP INSTALLATION

MAIN MENU | RESET | SUBMIT

A

1. Contractor Name & Number: 1079 ARK-MO WELL CO., INC.
2. Driller Name & Number: 2297 THOMAS SHELBY
3. Pump Installer Name & Number: 4014 ROBERT LAWRENCE
4. Date Well Completed: 07/20/1998 New Well
5. COUNTY: MISSISSIPPI (093)
6. FRACTION ¼ of SE ¼
7. SECTION: 28
8. TOWNSHIP 16
9. RANGE 11
11. LONGITUDE 89-55-07
12. LATITUDE 35-58-25

B

DESCRIPTION OF FORMATION	DEPTHS IN FEET FROM	TO	WATER BEARING	IF YES, DEPTH
TPSOIL/SD	0	3	No	
GMB	3	15	No	
SD	15	40	No	
SD/GRV	40	88	No	
GRV	80	93	No	
SD/GRV	93	100	No	

2. TOTAL DEPTH OF WELL 100
3. STATIC WATER LEVEL 13 Ft. below land surface
4. YIELD 2000 gallons per Y
5. DIAMETER OF BORE HOLE 24 IN

FT TO: FT
CASING FROM -9999 TO 60 W/ -9999 Inner Diameter
CASING FROM TO W/ Inner Diameter
TYPE CASING PVC
3. SCREEN
TYPE: PVC DIA 16 SLOT/GA 50
SET FROM 60 FT TO 100 FT
TYPE: DIA SLOT/GA
SET FROM FT TO FT
4. GRAVEL PACK FROM: 5 FT TO: 100 FT
5. BACK FILLED WITH: bentonite chips
FROM: 0 FT TO: 5 FT
6. SEALED WITH: BENTONITE CHIPS
FROM: 0 FT TO: 5 FT

Figure 6.9. The nearest borehole data less than half a mile of the study site [68].

Seven vertical stacks were sufficient to get good results. 29 shot points are done for the survey line, 10 ft as a distance between each shot. The location of shot points for survey line is shown in Figure 6.10.

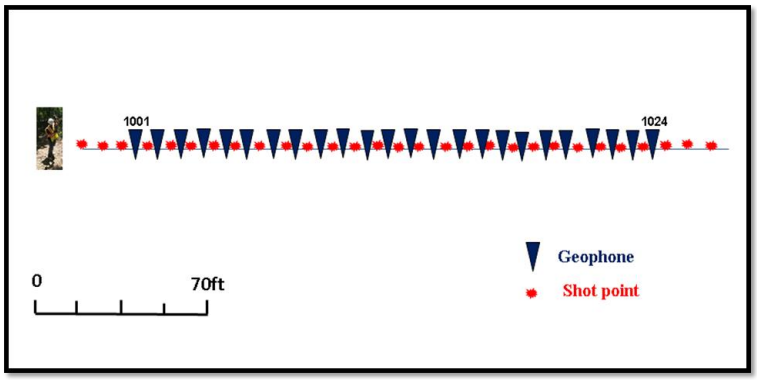

Figure 6.10. Location of the shot points for SRT traverse line.

6.3.2.2 SRT data processing. The results of the SRT data processing are shown in Figure 6.11, Figure 6.12, and Figure 6.13.

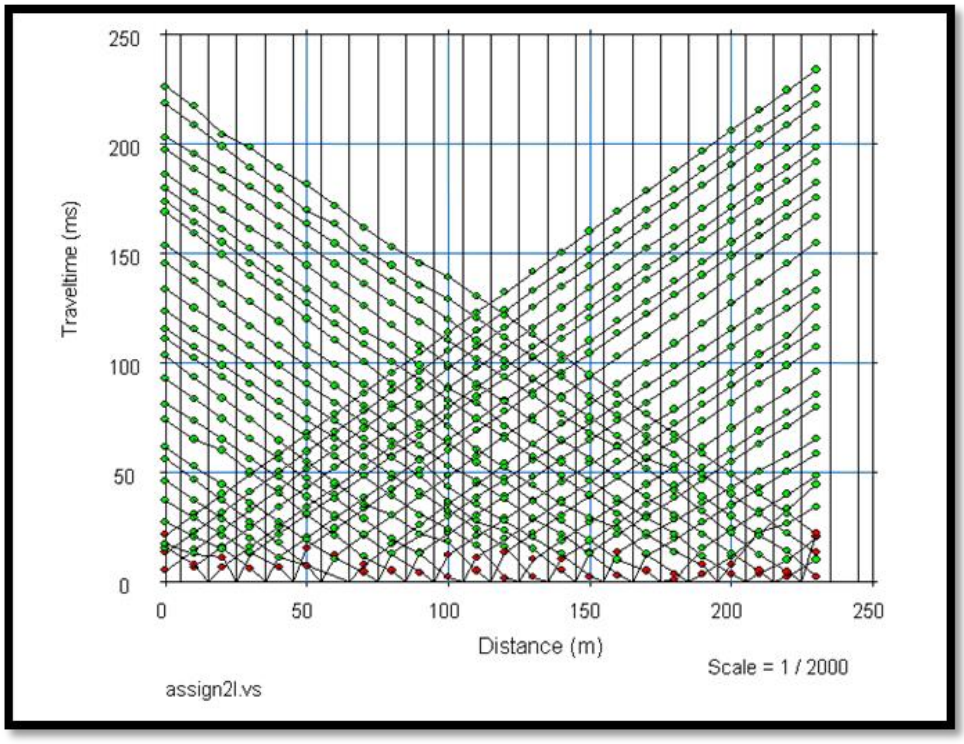

Figure 6.11. The assigning layers of the first arrivals.

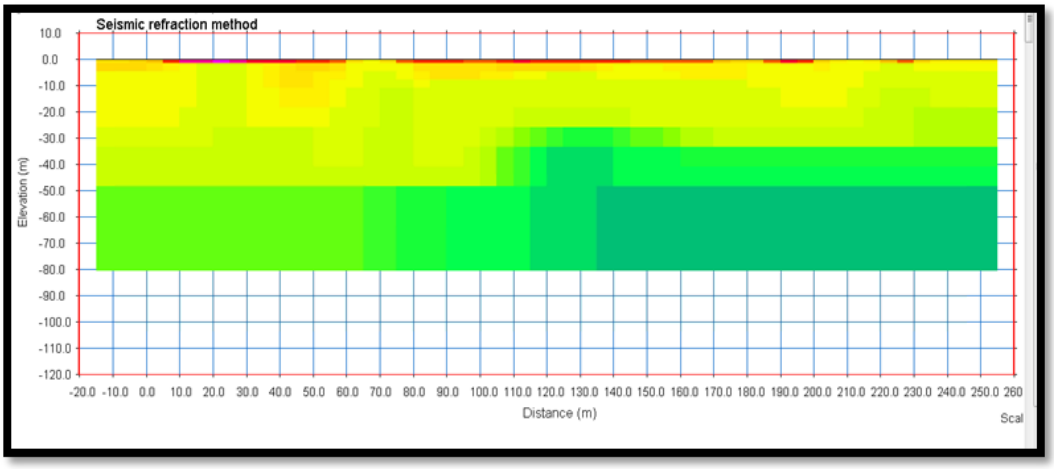

Figure 6.12. The synthetic velocity model for the test site.

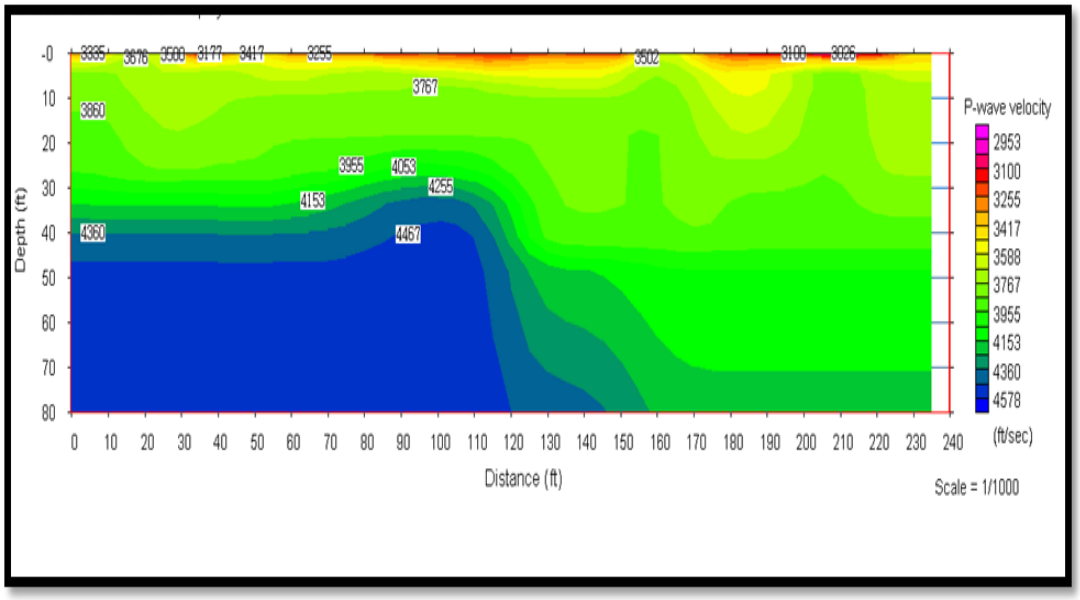

Figure 6.13. Pseudo 2-D P-wave velocity model profile resulting from SRT inversion.

6.3.3. MASW Survey. The MASW data acquisitions and processing have been done in this study.

6.3.3.1 MASW data acquisition. The MASW data acquisitions in this study were performed using 24 channels seismic equipment Seistronix RAS - 24, and 4.5 Hz geophones (Figure 6.14). The sampling interval used is 0.5 millisecond and recording time is 1,000millisecond.

Seven lines were overlapped with 10 ft. distance as shown in Figure 6.15. 24 Geophones are coupled firmly into the ground with spacing of 2.5 ft.; hence the total length of survey line is 57.5 ft. The offset distance was 10 ft. from the first geophone were used for the seven lines, one record at each source location were obtained. 20 lb. sledge hammer was used as the signal sources for data acquisition and the impact steel plate with dimensions of 1ft x 1 ft. as a choice to deliver appropriate impact power into the ground, and field laptop.

Figure 6.14. Location of the shot points for MASW array line.

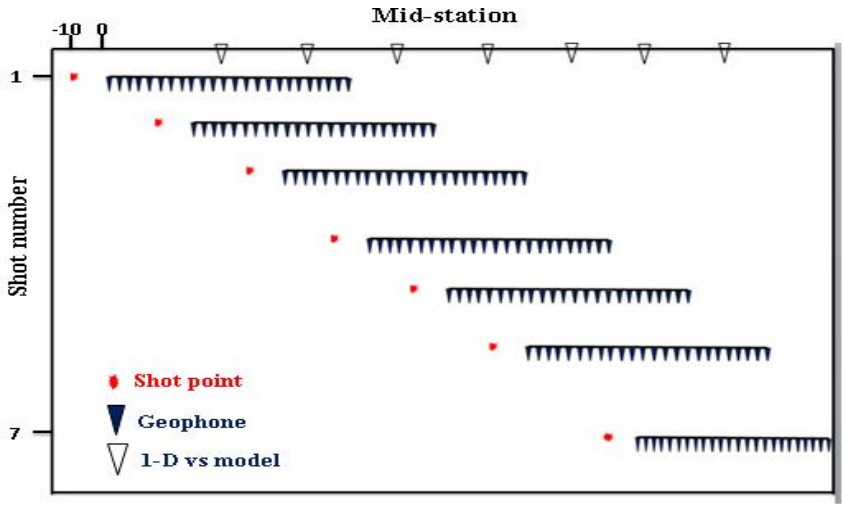

Figure 6.15. Location of the shot points for MASW traverses lines.

6.3.3.2 MASW data processing. Processing data of the all records was performed using the SurfSeis software package, developed by the Kansas Geologic Survey (KGS). The total records in the study lines were 7 records. Various processing parameters; frequency ranges, and phase velocities as shown in Figure 6.16, were used to generate dispersion curves and 1-D shear wave velocity profiles for all of the records:

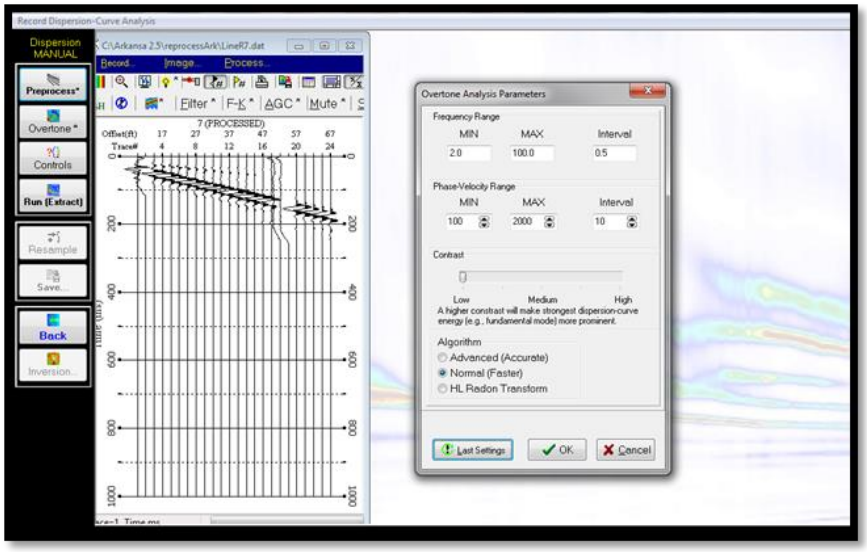

Figure 6.16. Overtone analysis parameters used for MASW lines.

The results of the shot gathers, the dispersion curves and the inverted of 1D shear wave velocity modules for all records are shown from Figure 6.17 to Figure 6.30.

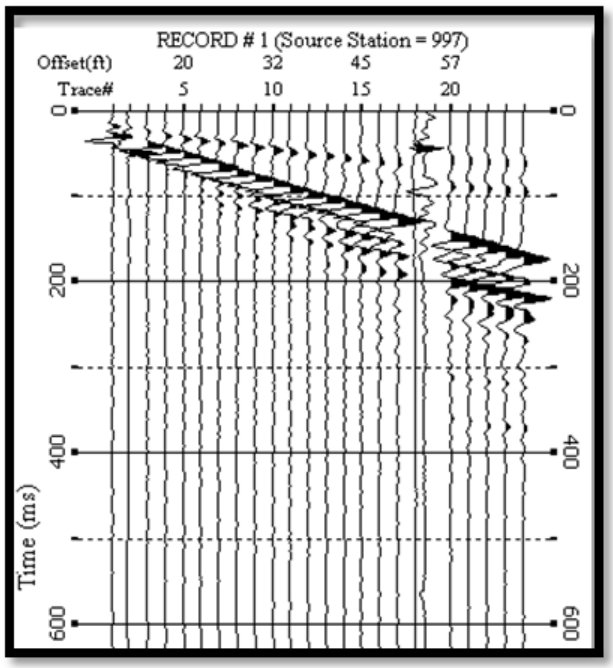

Figure 6.17. Shot gather used for line 1.

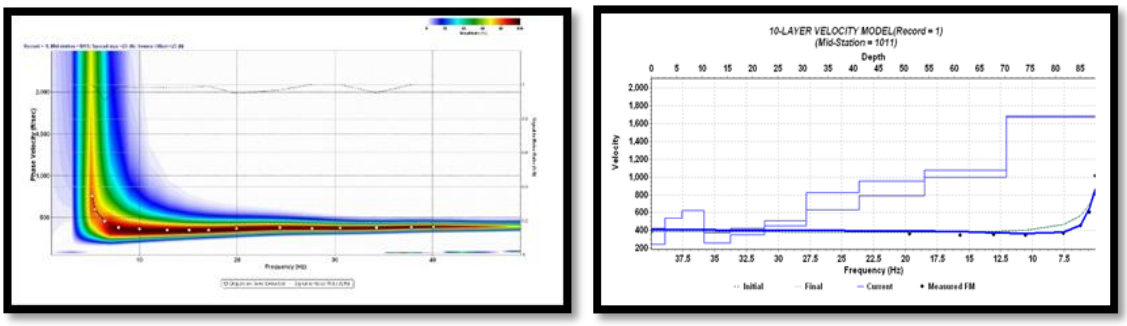

Figure 6.18. Step processing scheme for MASW data for line 1.

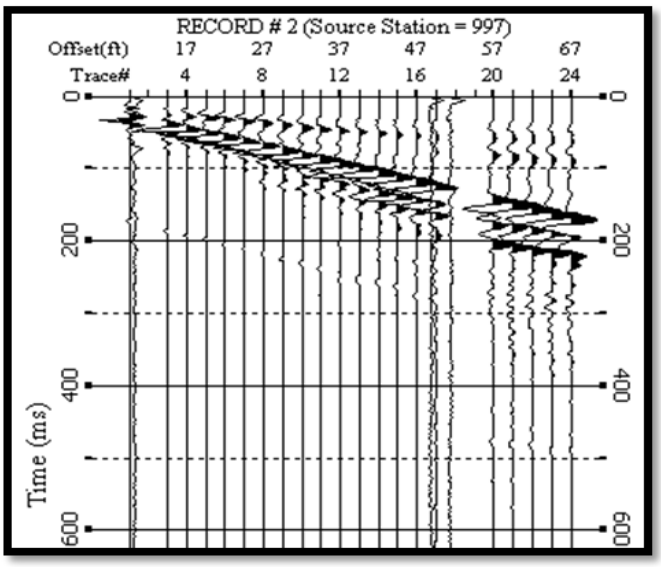

Figure 6.19. Shot gather used for line 2.

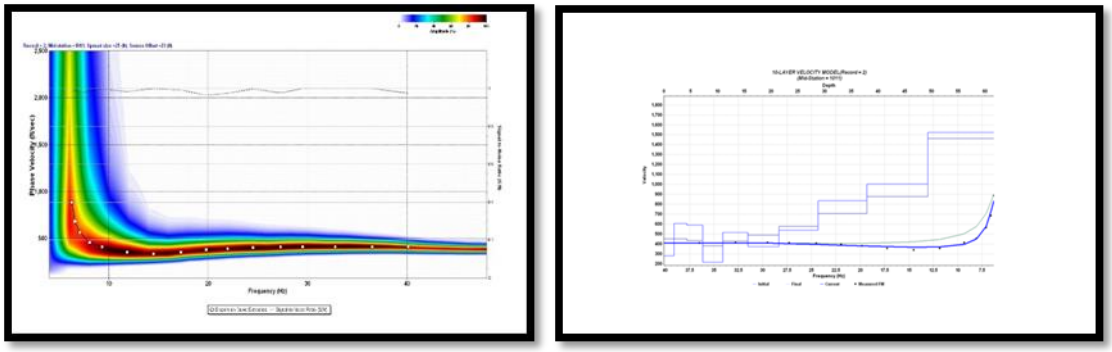

Figure 6.20. Step processing scheme for MASW data for line 2.

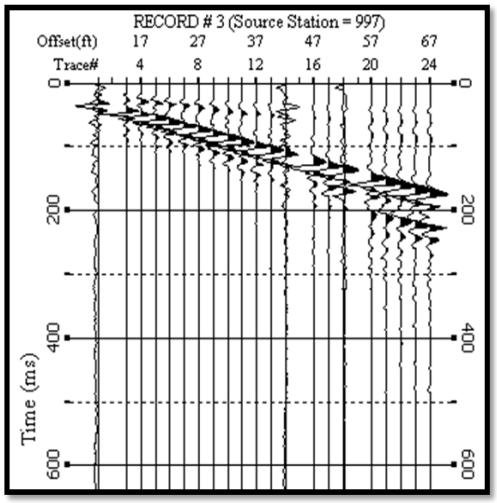

Figure 6.21. Shot gather used for line 3.

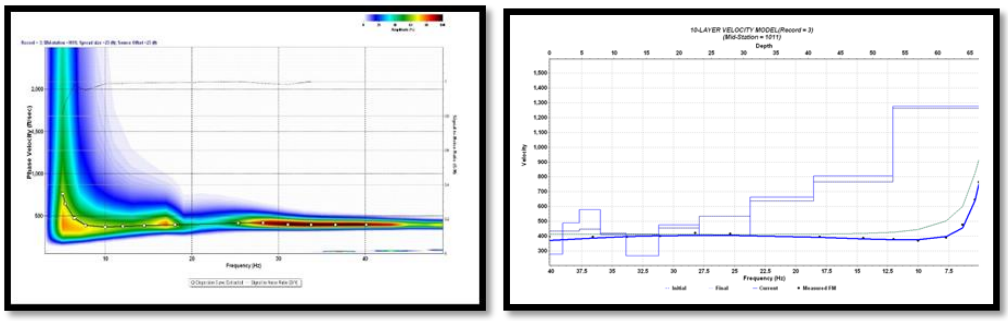

Figure 6.22. Step processing scheme for MASW data for line 3.

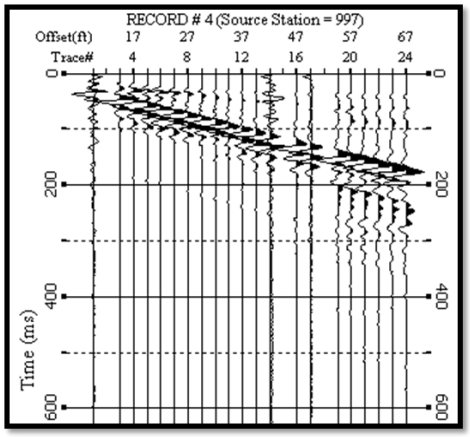

Figure 6.23. Shot gather used for line 4.

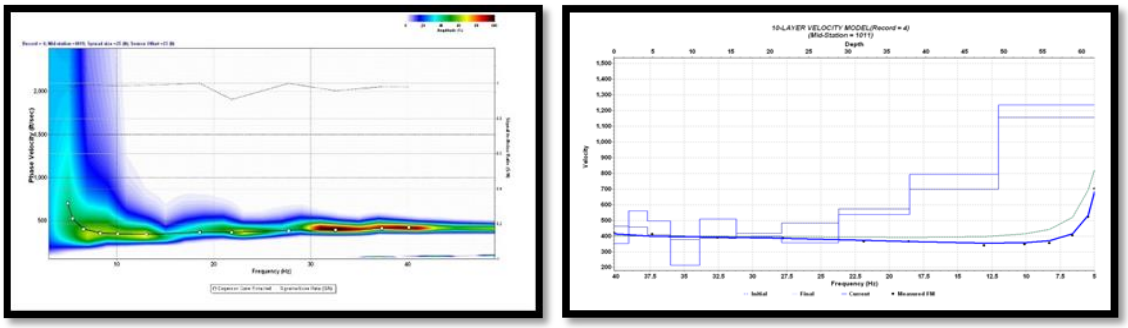

Figure 6.24. Step processing scheme for MASW data for line 4.

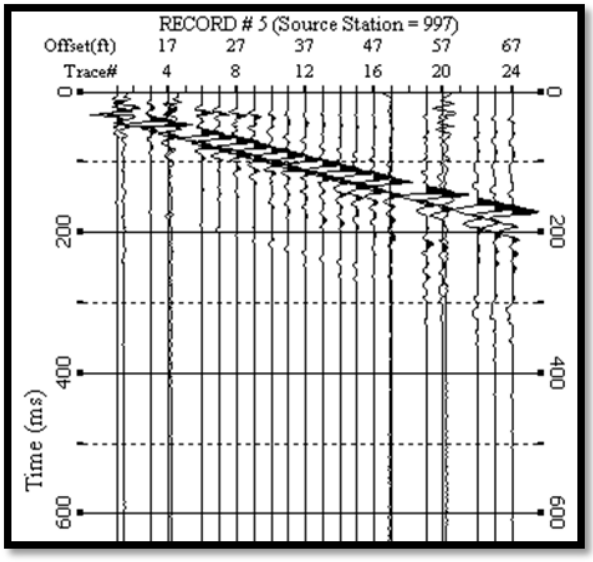

Figure 6.25. Shot gather used for line 5.

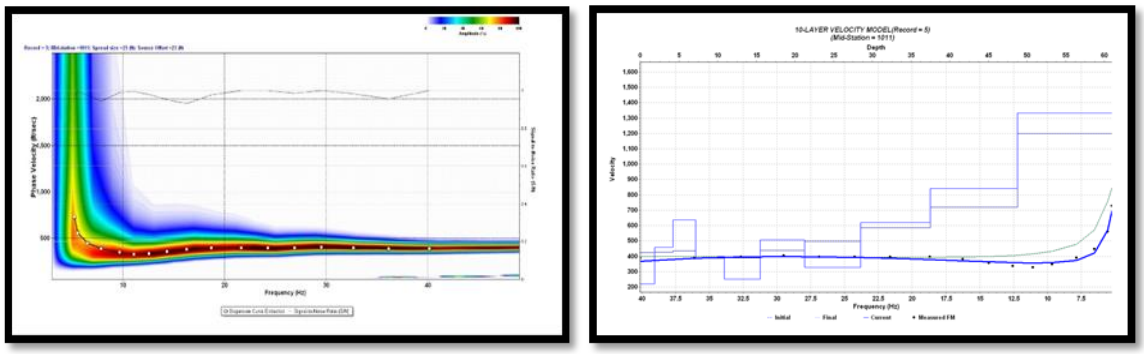

Figure 6.26. Step processing scheme for MASW data for line 5.

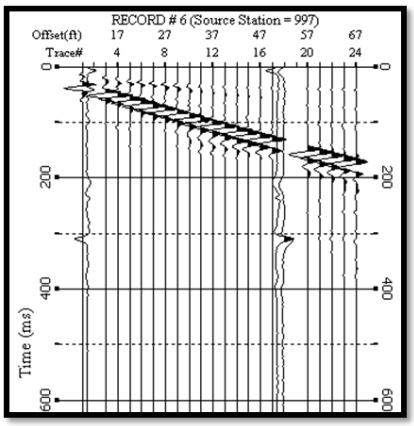

Figure 6.27. Shot gather used for line 6.

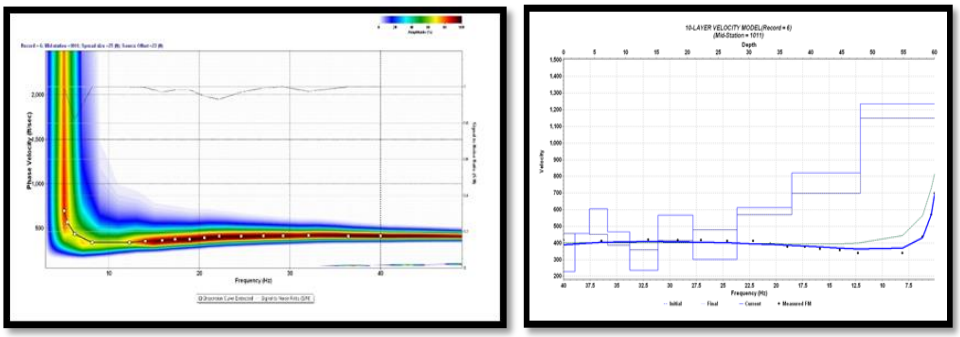

Figure 6.28. Step processing scheme for MASW data for line 6.

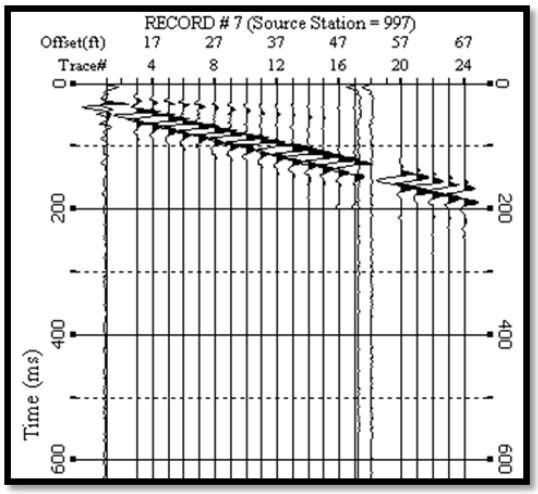

Figure 6.29. Shot gather used for line 7.

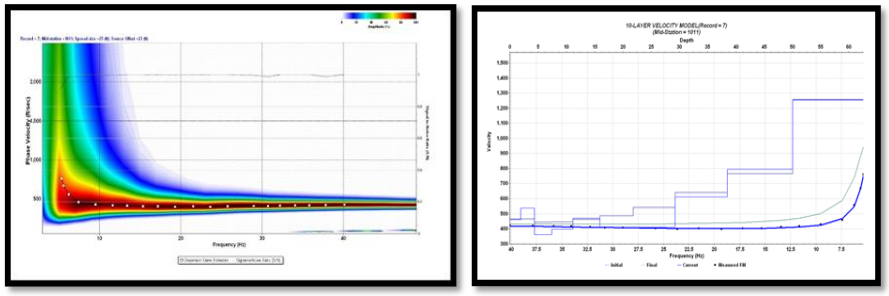

Figure 6.30. Step processing scheme for MASW data for line 7.

6.3.4. ERT Survey. ERT data was acquired using the AGI Super Sting R8/IP system and a dipole-dipole array. Data is recorded to .stg (Sting) format and imported as .dat format into the RES2DINV software. The bad data points are removed, so that lines are straight/parallel to indicate statistical consistency. Least Squares Inversion iterates to the best fit model for the data. Generally, the output of a 2D survey is a 2-D pseudo-sections and a 2-D resistivity model of the subsurface as shown in Figure 6.34.

6.4. RESULTS AND INTERPRETATIONS

The P-wave velocity model profile (Figure 6.31) was formed by SRT inversions, and Shear wave velocity model profile, (Figure 6.32), and (Figure 6.33) were formed by MASW inversions using 2.5ft geophone spacing are showing the fault zone.

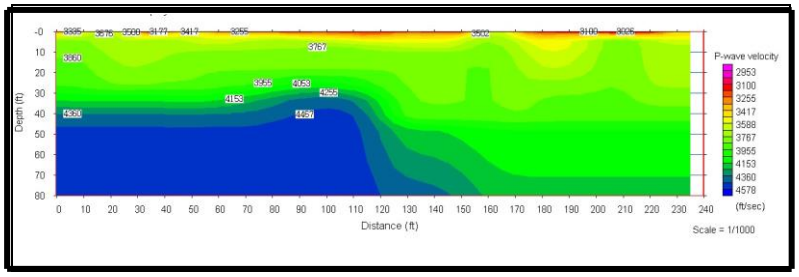

Figure 6.31. P-wave velocity model profile resulting from SRT inversion.

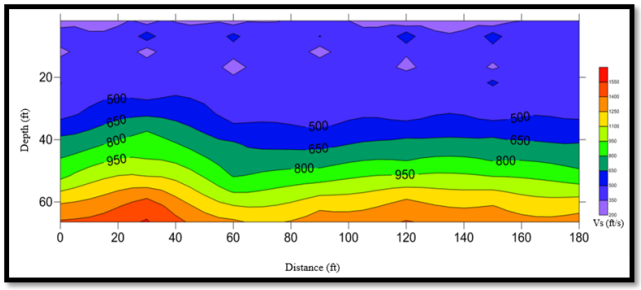

Figure 6.32. 2D model profile from MASW data shows the vertical displacement.

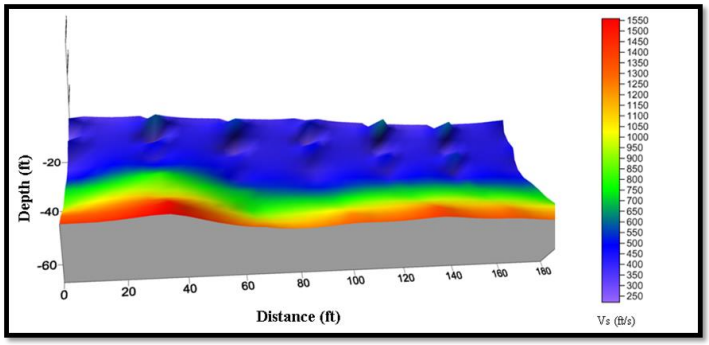

Figure 6.33. 3D model profile resulting from MASW data.

The resistivity model profile resulting from ERT inversion (Figure 6.34) shows the vertical displacement, where Figure 6.35 represent the vertical displacement measurement using ERT, SRT, and MASW data.

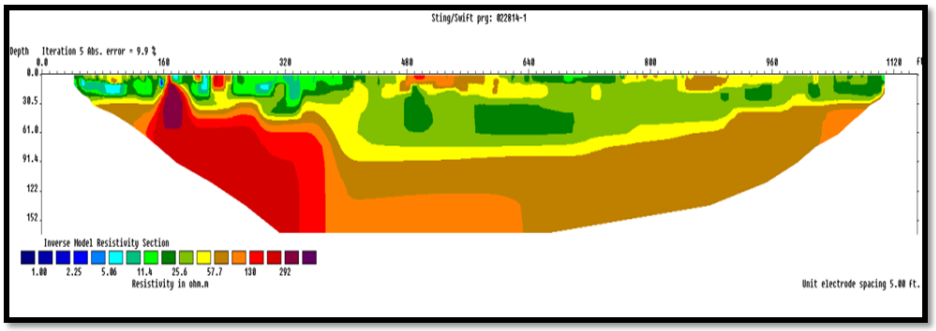

Figure 6.34. ERT model profile shows the vertical displacement.

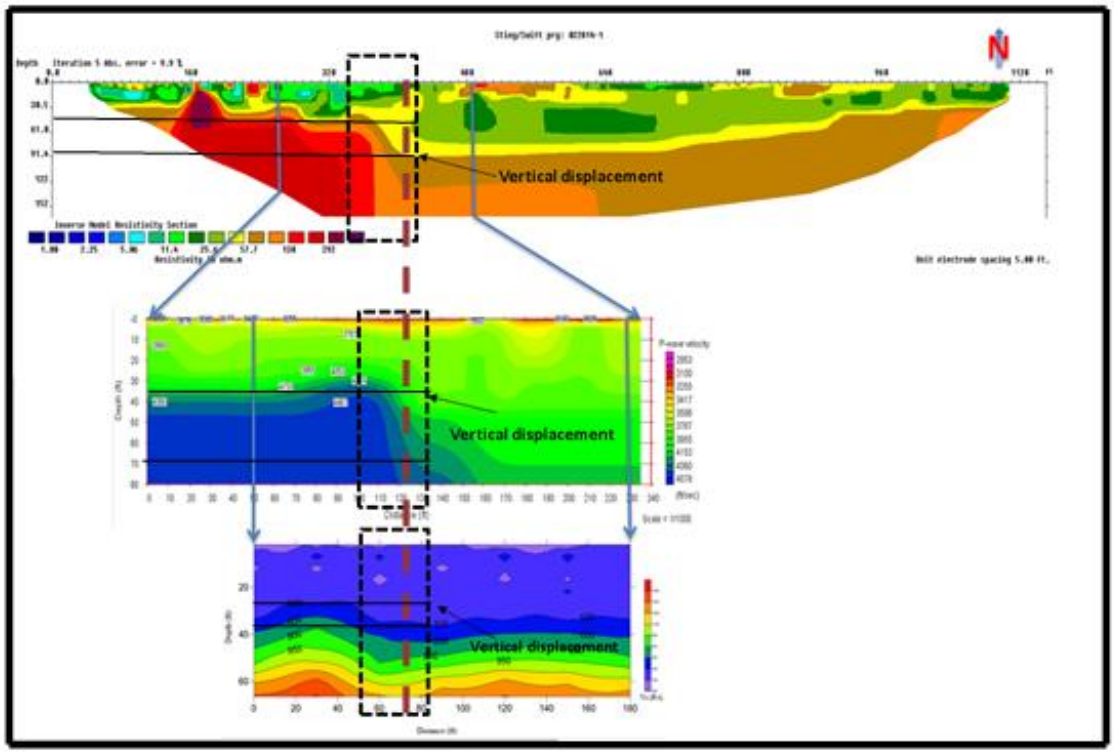

Figure 6.35. ERT, SRT and MASW model profiles show the vertical displacement.

7. CONCLUSIONS

This research presented two case studies, one in Illinois State and the other in Arkansas State, in which geophysical investigations were conducted to characterize the subsurface.

At the Illinois site, borehole control, downhole seismic, seismic refraction tomography and multichannel analysis of surface waves data were acquired with the purpose of seismic site characterization. The data analyses showed that:

Depth to bedrock determined by DHS, MASW and SRT is in good agreement with borehole data.

Shear wave and compressional wave velocities can be used to determine Poison's ratio, elastic moduli, and density of the subsurface.

Poison's ratio obtained by MASW and SRT are consistent with Poison's ratio measured by DHS testing.

Shear wave velocities obtained by MASW are consistent with shear wave velocities measured by DHS testing. Additionally, compressional wave velocities obtained by SRT are in a good agreement with compressional wave velocities measured by DHS testing.

A NEHRP class D assigned to the site based on average shear wave velocity in the upper 100 ft. is consistent with classification assigned on the basis of DHS testing data. All these observations lead to the conclusion that, for purposes of seismic site characterization, non-destructive geophysical methods (MASW, SRT) can be a reliable and cost-effective alternative to destructive geophysical method (DHS).

At the Arkansas site, borehole control, ERT, SRT, and MASW data were acquired with the purpose of mapping a postulated fault. The data analyses showed that:

Based on the ERT interpretations, upthrown block of the fault is characterized by resitivities in the range of 130-292 ohm-m, whereas downthrown block is characterized by resistivities in the range of 50-120 Ohm-m. This suggests that upthrown block is less porous and permeable, and therefore, contains less moisture than the downthrown block.

Based on the SRT interpretations, upthrown block is characterized by compressional wave velocities in the range of 4100-4578 ft/s, whereas downtrown block is characterized by compressional wave velocities in the range of 3500-4000 ft/s.

Electrical resistivity signatures obtained from the fault have a remarkable similarity with seismic refraction signatures. More specifically, the fault mapped on ERT and SRT has a vertical displacement of approximately 40 ft.

Shear wave velocity signatures of the fault showed that the fault has a vertical displacement of approximately 15 ft.

All these observations lead to the conclusion that integrated use of seismic (SRT, MASW) and electrical (ERT) methods are an effective approach in mapping the fault. Additionally, the integrated use of geophysical methods is particularly effective in assessing soil and rock in the New Madrid Seismic Zone.

BIBLIOGRAPHY

[1] http://geology.isu.edu/wapi/EnvGeo/EG5_earthqks/waves.jpg. Direction of seismices generated by earthquake, March 2014.

[2] H. W. Bakun and G. M, "Hopper, Magnitudes and locations of the 1881-1812 New Madrid, Missouri, and the 1886 Charleston, South Carolina, earthquakes", Bulletin of the Seismological Society of America, pp. 94 (1), 64-75, 2004.

[3] http://www.showme.net/~fkeller/quake/maps.htm.The USGS map shows the areas potentially under threat from earthquakes in both the new Madrid seismic zone and the Wabash valley seismic zone. March 2014.

[4] M. Morin, "New insight on the nation's earthquake hazards Web," 2014.

[5] https://pubs.usgs.gov/of/2009/1198/pdf/OF09-1198.pdf. Local soil conditions affect the intensity of shaking,Nov 2016.

[6] http://nptel.ac.in/courses/105108072/mod02/image/lec1_clip_image018_0000.jpg Stress acting on the elemental cube,Jully 2016.

[7] D. S. Parasnis, "Principles of Applied Geophysics," Chapman & Hall. ISBN 978-0- 412-64080-3, 1997.

[8] https://nikhilkardale.files.wordpress.com/2010/05/stress-vs-strain.jpg. Stress and strain relationship, May 2016.

[9] https://www.britannica.com/science/Youngs-modulus. Young's modulus diagram, June 2016.

[10] http://www.kshitij-iitjee.com/Study/Physics/Part1/Chapter12/34.jpg. Shear modulus diagram, June 2016.

[11] http://www.kshitij-iitjee.com/Study/Physics/Part1/Chapter12/34.jpg. Compressed cube in all sides,Nov 2016.

[12] http://web.ics.purdue.edu/~braile/edumod/waves/WaveDemo.htm. Seismic wave demonstrations and animations, June 2015.

[13] Kearey, Brooks and Hill, "Introduction to Geophysical Exploration," Williston: Blackwell Publishing, 2002.

[14] https://compass.astm.org/EDIT/html_annot.cgi?D5777+00 (2011) e1. Range of velocities for compressional waves in soil and rock, April 2017.

[15] M. B.Dobrin and C. H. Savit, “Introduction to geophysical prospecting,” New York: McGraw-Hill Book Co.Geophysics, 64, 3, p. 800-808, 1998.

[16] F. E. Richart, J. R. Hall and R. D.Woods,“Vibrations of soils and foundations”Prentice-Hall, Inc, 1970.

[17] J. Xia R.D. Miller and C.B. Park, “Estimation of near surface shear-wave velocity by inversion of Rayleigh waves”: Geophysics, 64, 691–700. 1999.

[18] K. H. Stokoe, G. W. Wright, A. B. James and M. R. Jose, “Characterization of geotechnical sites by SASW method. In: Woods RD, Ed,” Geophysical characterization of sites, A. A. Balkema/Rotterdam, p. 15-25, 1994.

[19] R. E. Sheriff, “Encyclopedic dictionary of exploration geophysics. 4th ed. Tusla: Society of exploration Geophysicists, 115-116, 1991.

[20] W. Mayne, “Measurements of Shear Wave Velocity: Crosshole & Downhole Geophysics, 2012.

[21] http://www.zoomschool.com/usa/statesbw/arkansasbw.GIF. Arrival time curve from downhole seismic test for shear wave velocity measurements, Nov 2016.

[22] J. Xia R.D. Miller C.B. Park E. Wightman and R. Nigbor, “A pitfall in shallow shear-wave refraction surveying”. Journal of Applied Geophysics, 51, 1, 1-9, January 01, 2002.

[23] W. M. Ewing,W. S. Jardetsky and F. Press, , Elastic waves in a layered media, McGraw-Hill, 1975.

[24] P. Gabriels, R. Snieder and G. Nolet, “In situ measurements of shear-wave velocity in sediments with higher-mode Rayleigh waves,” Geophysical Prospecting: 35,187-196, 1987.

[25] http://www.kgs.ku.edu/Publications/PIC/37gifs/fig6.png. Spike coupled Geophone, March 2014.

[26] M.H. Loke, “Electrical Imaging Survey for Environmental and Engineering Studies,” 2000.

[27] Milson and John “Field Geophysics,” New York: John Wiley & Sons, 1996.

[28] http://www.zapatainc.com/wp-content/uploads/2011/11/Processing.jpg. A 3-step processing scheme for MASW data,May 2014.

[29] http://www.kgs.ku.edu/software/surfseis/masw.html. Construct a 2-D vs map from a MASW survey,Dec 2016.

[30] H. Burger and Roberts, “Exploration Geophysics of the Shallow Subsurface”. Prentice Hall, Inc, 1992.

[31] Stork and Clayton, “Linear aspects of tomographic velocity analysis” Geophysics, 56, 483-495, 1991.

[32] http://a-levelphysicstutor.com/images/waves/huygns-post.jpg. Construct a new wave front from the original one,Oct 2015.

[33] http://www.bing.com/images/search?q=Snell%27s+Law+Explained&FORM =IRBPRS&=0. The relationship of energy passing across a boundary between faster and slower media (Snell’s law), Oct 2015.

[34] J. M. Reynolds, “An Introduction to Applied and Environmental Geophysics,” John Willey & Sons Ltd., Hoboken, 1997.

[35] C.B. Park, R.D. Miller and J. Xia, “Multi-channel analysis of surface waves”, 1999.

[36] M.L. Rucker, “Applying the seismic refraction technique to exploration for transportation facilities, in geophysics,” The first international conference on the application of the geophysical methodologies to transportation facilities and infrastructure, St. Louis, Missouri, p. 1-3, 2000.

[37] K. Hayashi and T. Takahashi, “High Resolution Seismic Refraction Method Using Surface and Borehole Data for Site Characterization of Rocks,” International Journal of Rock Mechanics and Mining Sciences, Vol. 38, pp. 807-813, 2001.

[38] H.R. Thornburgh, “Wave front diagrams in seismic interpretation,” Bull. A. A. P. G., pp. 185–200, 1930.

[39] G.H.F. Gardner, L.W. Gardner and A.R. Gregory, “Formation velocity and density,” the diagnostic basics for stratigraphic traps Geophysics, 39, pp. 770–780, 1974.

[40] M.M. Slotnick, “A graphical method for the interpretation of refraction profile data Geophysics,” pp. 163–180, 1950.

[41] L.H. Tarrant, “A rapid method of determining the form of a seismic refractor from line profile results,” Geophysics. Prospect. pp. 131–139, 1956.

[42] J.G. Hagedoorn,”The plus-minus method of interpreting seismic refraction sections,”Geophys Prospect, 7, pp. 158–182, 1959.

[43] D. Palmer, “The generalized reciprocal method of seismic refraction interpretation,” Soc. Explor. Geophys. 1980.

[44] P. Linderholm, L. Marescot, M. H. Loke and P. Renaud, “Cell culture imaging using microimpedance tomography,” IEEE Transactions on Biomedical Engineering, 55,138–146, 2008.

[45] H. Storz, W. Storz and F. Jacobs, “Electrical resistivity tomography to investigate geological structures of the earth’s upper crust,” Geophysical Prospecting, 48, 455–471,2000.

[46] R.M.S. White, S. Collins R. Denne, R. Hee and P. Brown, “A new survey design for 3D IP modelling at Copper hill,” Exploration Geophysics 32, 152–155, 2001.

[47] http://subsurfaceinsights.com/images/electrode_geometries.png. Electrode array configurations for resistivity measurements,Nov 2016.

[48] http://www.gbgmaps.com.au/methods/electrical-resistivity-imaging. Resistivity of different rock types,Nov 2016.

[49] D. Hoffman, N. Anderson and J. D. Rogers,“St. Louis, metro area shear wave velocity testing,” U.S. Geol. Surv. Final Tech. Rept, 2008.

[50] C.B. Park, J. Xia and and R.D. Miller, “Imaging dispersion curves of surface waves on multichannel record,” In: 68th Ann. Internat. Mtg., Soc. Expl. Geophys., Expanded Abstracts, pp. 1377–1380, 1998.

[51] https://earthquake.usgs.gov/hazards/urban/st_louis.php. Location map of the study area, Feb 2017.

[52] D. A. Grimley, G. A. Shofner and Illinois State Geological Survey, “Surficial geology of Ames quadrangle, Monroe and Randolph counties, Illinois,” Champaign, Ill:Illinois State Geological Survey, 2008.

[53] A.G. Unklesbay and D. Jerry,“Missouri Geology: Three Billion Years of London, Volcanoes, Seas, Sediments, and Erosion,” University of Missouri Press Columbia and 1992.

[54] A. J. Crone, “Sample description and stratigraphic correlation of the New Madrid test well-1-X,” New Madrid County, Missouri, U.S. Geol. Surv. Open-File Rept. 81-426,26, 1981.

[55] Geotechnology,INC “Down hole seismic testing for Mississippi river bridge,” St. louis , Missouri, U.S. Geotecnology, INC. Proj. 1038101.87TG, NOV 20, 2008.

[56] C.B. Park, R.D. Miller and H. Miura,"Offset and resolution of dispersion curve in geophysics multichannel analysis of surface waves(MASW)," Symposium on the application of two engineering and environmental problems, SAGEEP, 2001.

[57] http://earthquakes.unlv.edu/SeismicRiskAnalysis/soil.jSoil profile type classification for seismic amplification, May 2015.

[58] http://www.zoomschool.com/usa/statesbw/arkansasbw.GIF.Map of study site in Blytheville,Nov 2016.

[59] http://www.geology.ar.gov/geology/strat_missembayment_gulfplain.htm Stratigraphic correlation charts for West Gulf Coastal Plain and Mississippi River Alluvial Plain sub regions of the Gulf Coastal Plain of Arkansas.

[60] M. J. Guccione, R. Marple and W.J. Autin, "Evidence for Holocene displacements on the Bootheel fault (lineament) in southeastern Missouri: Seismotectonic implications for the New Madrid region," Geological Society of America Bulletin, p. 320–333, 2002.

[61] T. Saucier, "Geomorphology and Quaternary geo- logic history of the lower Mississippi valley: Vicks-burg, Mississippi," U.S. Army Engineers Waterways Experiment Station, v. II, scale 1:250,000, 1994.

[62] R. Csontos and R. Van Arsdale, " New Madrid seismic fault geome-try,"Geol. Soc. Am.4,802–813, 2008.

[63] http://www.eas.slu.edu/eqc/eqc_publ/Flyers/CUS/nm_block.gif. New Madrid Faults Structures, May 2016.

[64] Van Arsdale, R. B., J. Purser, W. J. Stephenson, and J. K. Odum,"Faulting along the southern margin of Reelfoot Lake," Tennessee,Bull.Seismol. Soc. Am.88, 131–139,1998.

[65] S. C. Chiu, J. M. Chiu and A. C. Johnston, "Seismicity of the south-eastern margin of Reelfoot rift, central United States," Seism. Res. Lett.68, 785–796., 1997.

[66] R. T.Cox, R. B. Van Arsdale, J. B. Harris and D. Larsen "Neotec-tonics of the southeastern Reelfoot rift zone margin, central UnitedStates, and implications for regional strain accommodation," Geology29,419–422, 2001.

[67] B.A. Van der Pluijm, and S. Marshak, “Earth structure: An introduction to structural geology and tectonics: New York, W.W. Norton & Company. 656 p, 2004.

[68] https://ar.water.usgs.gov/. The nearest borehole data less than half a mile of the study site, Jan 2017.

VITA

Faraj Mohamed Eljabri was born in Kasir Al-akhyar city, Libya. In 1987 he graduated from High School Kasir Alakhiar.

In 1993, he had B.Sc. Degree in Geological Engineering at the faculty of engineering, Tripoli University, Tripoli –Libya and a Master's degree at the same university.

He received his PhD in Geological Engineering from Missouri University of Science and Technology in December 2017.

Faraj is a member of European Association of Geoscientists & Engineers (EAGE). He had been in Libyan 2007 Conference & Exhibition of 3rd North African /Mediterranean Petroleum.

He had summer training in September, 1992, with Schlumberger Company in wire line logging in Sarir Field, Arabian Golf oil company, Sarir –Libya, and had drilling course in mud logging & gas detection instrumentations (Als2 system) with Geoservice Company, Safax, Tunisia May, 1997. Safety course in H2S gas with Total Company in July, 2003.

He had joined Transportation Infrastructure Conference held at Jefferson City MO, September 13, 2013.

He was taken MASW/SurfSeies workshops held at Kansas Geological Survey, Lawrence, Kansas June 19-20, 2014 and July 14-15, 2016.